UNIVERSITY OF COPENHAGEN

PhD Thesis

Electro- and opto-mechanics with soft-clamped membrane resonators at milliKelvin temperatures for quantum memory and transduction

Eric Planz

Supervised by Prof. Dr. Albert Schließer

This thesis has been submitted to the PhD School of

The Faculty of Science, University of Copenhagen

August 2023

Eric Planz
Electro- and opto-mechanics with soft-clamped membrane resonators at milliKelvin temperatures for quantum memory and transduction
PhD Thesis, August 2023
Supervisor: Prof. Dr. Albert Schließer

University of Copenhagen
Faculty of Science
Center for Hybrid Quantum Networks, Niels Bohr Institute

Acknowledgements

I am sincerely grateful to my advisor, Albert Schließer. His high standards and strong drive consistently encouraged me to push myself in this substantial project. I am thankful for the chance to work on such a critical topic under his supervision and look up to his dedication to physics - and to our research section's Julefrokost.

A special thanks to my postdoctoral colleagues. Thibault Capelle, with his careful eye for technical detail was a pillar of this project. His commitment and supportive approach have been invaluable in this journey. Xiang Xi, despite joining our team later, had a significant impact on my research and approach to problem-solving. His talent for breaking down, locating, and addressing problems has deeply enriched my learning experience. I am indebted to both for their contributions.

I am grateful for the occasional but crucial support from Professor Jörg Müller, who not only helped keep our research running with backup lasers but also lent a comforting presence in the lounge. Professor Emil Zeuthen, I appreciate our stimulating discussions; your German certainly has character!

My thanks also extend to our competent secretaries, particularly Dorte Nielsen and Erika Bodova, whose efficiency ensured smooth sailing in administrative matters. I am also grateful to the members of the mechanical workshop, whose readiness to assist with quick fixes was instrumental in keeping our work on track.

This research was made possible by the generous support of the Talent Doctoral Fellowship, for which I am deeply grateful.

I am thankful for the companionship and support of my lab mates, especially Mads Kristensen, Yannick Seis, Lucio Stefan, Sho Tamaki, and Ivan Galinskiy, and everyone else in the SLAB team who have all been a source of friendship, intellectual stimulation, and mutual support.

On a personal note, I extend my deepest gratitude to my family for their unfailing love and belief in my capabilities. Their ongoing encouragement has been my rock. I also thank my friends Cassandra, Rebecca, Arianne, Linnan, Oscar, Carlos, Patrik, Mai, Julian, Shikai, Johann, Marco, Daniel, Nicholas, Nick, and Zack for their enduring friendship and support during challenging times. I am grateful for many other friends and colleagues at the Niels Bohr Institute creating a welcoming and supportive environment, and making it the perfect place to pursue a PhD.

The path towards completing this PhD was paved with trials and triumphs. I have learned the art of problem-solving: the importance of thorough testing, breaking down big problems into smaller parts, the satisfaction in solving these problems, and the consistent chase of our goals. I am deeply grateful for these insights, which will certainly be of great value in my future work.

Abstract

This thesis focuses on the advances and challenges in coupling electromagnetic fields in the microwave and optical domain to soft-clamped membrane mechanical resonators, a promising component in emerging quantum technologies. Soft-clamped membranes exhibit exceptionally low mechanical damping due to their isolated mechanical modes from their substrate, enabling ground-state cooling and an extraordinary 140 ms coherence time. However, certain limitations must be addressed for their effective implementation in quantum systems.

In electro-mechanical coupling, the coupling strength is constrained by nanofabrication techniques. Microwave resonators and mechanical resonators have to be brought very close to each other for electro-mechanical coupling. We have demonstrated how integrating a piezo actuator might significantly enhance this coupling.

Opto-mechanical coupling presents its own challenges: operating a high-finesse cavity in a dilution refrigerator, optical losses due to the membrane resonator design, and optical absorption heating of the membrane material. For the first issue, we have devised a new design of a high-finesse cavity that enables operation at milliKelvin temperatures. To tackle optical losses of the membrane design, we have characterized them and derived and implemented design considerations that can minimize these losses. We built a low optical loss, high-finesse cavity with a refined membrane design for the absorption heating effect. We then characterized how optical absorption heating influences the thermal bath temperature and the intrinsic mechanical decay rate.

Our findings offer comprehensive solutions that significantly enhance soft-clamped membrane resonators' electro- and optomechanical coupling. This

work lays a critical foundation for low-noise quantum transduction with embedded quantum memory, paving the way for the next generation of quantum technologies.

Sammenfatning

Denne afhandling fokuserer på fremskridt og udfordringer ved kobling af elektromagnetiske felter, både i mikrobølge- og optisk domæne, til soft-clamped membranresonatorer, en lovende komponent i nykommende kvanteteknologier. ‘Soft-clamped’ membraner viser en usædvanlig lav mekanisk dæmpning på grund af deres isolerede mekaniske tilstande, hvilket gør grundtilstandskøling og en ekstraordinær 100 ms kohærenstid mulig. Der skal dog adresseres visse begrænsninger for deres effektive implementering i kvantesystemer.

Ved elektromekanisk kobling er styrken begrænset af nanofabrikationsteknikker. Mikrobølgeresonatorer og mekaniske resonatorer skal bringes meget tæt på hinanden for elektromekanisk kobling. Vi har demonstreret, hvordan integrationen af en piezo-aktuator kan forbedre denne kobling betydeligt.

Optomekanisk kobling præsenterer sine egne udfordringer: drift af en høj-finesse-kavitet i en fortyndingskryostat, optiske tab på grund af membranresonatordesign og optisk absorptionsopvarmning af membranmaterialet. For at addressere det første problem har vi udviklet et nyt design til høj-finesse-kaviteten, der muliggør drift ved milliKelvin temperaturer. For at tackle optiske tab fra membrandesignet har vi nøje karakteriseret dem hvorfra vi har afledt og implementeret designovervejelser, der kan minimere disse tab. For absorptionsopvarmningseffekten byggede vi en lavt optisk tab, høj-finesse-kavitet med et forfinet membrandesign. Vi karakteriserede derefter, hvordan optisk absorptionsopvarmning påvirker badtemperaturen og den indbyggede mekaniske henfaldshastighed.

Vore fund tilbyder omfattende løsninger, der markant forbedrer elektro- og optomekanisk kobling af ‘soft-clamped’ membranresonatorer. Dette arbejde

lægger en kritisk grund for lavstøjende kvantetransduktion med en indlejret kvantehukommelse, hvilket baner vejen for næste generation af kvanteteknologier.

Publications and Presentations

Journal Publications

- E. Planz*, X. Xi*, T. Capelle*, E. Langman, A. Schliesser. "Membrane-in-the-middle optomechanics with a soft-clamped membrane at milliKelvin temperatures". Submitted to Optics Express. ArXiv submission identifier 5037710. **shared first-authorship*

- Y. Seis, T. Capelle, E. Langman, S. Saarinen, E. Planz, A. Schliesser. "Ground state cooling of an ultracoherent electromechanical system". Nat Commun 13, 1507 (2022).

Oral Presentations

- Quantum Matter International Conference – QUANTUMatter 2023, Madrid, Spain (2023)

- IBM Quantum Transduction Workshop, IBM Research, Rüschlikon, Switzerland (2023)

- Danish National Research Foundation, Hy-Q Follow-Up Meeting, Copenhagen (2023)

Poster Presentations

- Quantum Enhanced Sensing Symposium, Copenhagen (2023)
- UCPH Quantum Hub Annual Meeting, Copenhagen (2023)
- Gordon Research Conference "Mechanical Systems in the Quantum Regime", Ventura, CA, USA (2022)
- Danish Optical Society, Annual Conference, Copenhagen (2021)

Contents

1 Introduction **3**
1.1 Superconducting Quantum Computing 5
1.1.1 DiVincenzo Criteria and Superconducting Qubits 5
1.2 Quantum Transduction 7
1.2.1 Figures of Merit 8
1.3 Experimental Platforms Suitable for Transduction 8
1.3.1 Rydberg Atoms 8
1.3.2 Electro-Optic Modulation 9
1.3.3 Magneto-Optic Modulation 9
1.3.4 Piezoelectric Transduction 10
1.3.5 Electro-Optomechanical Transduction 10
1.4 Quantum Memory 11

2 Fundamentals on Cavity Opto- and Electromechanics **13**
2.1 Membrane Resonators 13
2.2 Cavity Optomechanics 19
2.2.1 Optical Cavities 19
2.2.2 Optomechanical Interaction 21
2.2.3 Dynamical Backaction 23
2.2.4 Heating Effects 26
2.3 Electromechanics 27
2.4 Electro-Optomechanical Transduction 28
2.4.1 Summary of the Derivation of the Transduction Efficiency 29
2.4.2 Added Noise 32
2.4.3 Bandwidth 33

3 Low Effective Mass Soft-Clamped Membranes at milliKelvin Temperatures **35**
3.1 Motivation and Design 35
3.2 Setup 37
3.3 Results 38

3.4 Comparison to other Designs 41
3.5 Conclusion 43

4 Enhanced Electromechanical Coupling to Soft-Clamped Membrane Resonators 47
4.1 Ground State Cooling of an Ultracoherent Electromechanical System 48
4.2 Implementing Coplanar Microwave Coupling 55
4.3 Increased Coupling Strength g_0 via Actuator-Based Capacitor Gap Tuning 57

5 High-Finesse Optomechanical Cavity Inside Dilution Refrigerators 61
5.1 Vibrations of Dilution Refrigerators 61
5.2 Cavity Parameters 62
5.3 Vibration Isolation 65
5.3.1 Breadboards Clamped to the Dilution Refrigerator 69
5.4 High-Finesse Optical Cavity at milli-Kelvin Temperatures 69
5.5 Membrane Design 72
5.6 Design with Integrated Electromechanical Access 75

6 Optomechanical Cooling and Absorption Heating of Soft-Clamped Membranes at Milli-Kelvin Temperatures 79
6.1 Phonon Occupation of Radiation-Pressure Cooling 79
6.2 Mechanical Resonator 81
6.3 Optomechanical Cavity 81
6.4 Measurement Setup 81
6.5 Results 89
6.6 Discussion 93

7 Conclusion 99

8 Prospective Directions 103

9 Bibliography 107

1 Introduction

The discovery of quantum mechanics in the early twentieth century marked a shift in our understanding of the physical world, shifting the paradigm from the deterministic universe of classical physics to a realm governed by probability and uncertainty. Groundbreaking work by pioneering physicists, such as Max Planck, Albert Einstein, Erwin Schrödinger, and Niels Bohr, paved the way for a new approach to understanding the microscopic world of particles and atomic structures [Planck, 1901; Bohr *et al.*, 1924]. In particular, the particle-wave duality exhibited by both light and matter presented the scientific community with opportunities and challenges.

Quantum mechanics is the cornerstone for the emergence of quantum computing. In contrast to classical computing, which uses bits as its basic unit of information, quantum computing leverages the quantum bit or qubit. This computational approach allows for algorithms that can solve certain mathematical problems with shorter computation time, thanks to the quantum phenomena of superposition and entanglement [Shor, 1997; Arute *et al.*, 2019].

A milestone in applying quantum mechanics was the invention of the laser in the 1960s [Mainman, 1960], an outcome of Einstein's work on the quantum theory of radiation. The laser, producing a coherent, monochromatic beam of light, became the tool that enabled unprecedented control over atomic states and energy transitions which, in turn, led to a deeper understanding of quantum physics.

The research field of optomechanics, explored early on by Braginskii, explores the interaction between light and mechanical motion [Braginskii and Manukin, 1967]. With laser advancements, sensitive measurement techniques, and the creation of micro- and nanomechanical resonators, the research field has allowed optomechanics to reach the quantum regime, i.e., where a quantum-mechanical treatment of both light and mechanical motion is necessary [Aspelmeyer *et al.*, 2014]. This progress was made possible by isolating mechanical systems from their environment to the level at which their motion could be coherently controlled and observed in their quantum-mechanical ground state.

Several quantum systems, including ions, neutral atoms, nitrogen-vacancy centers, single photons, and Josephson junctions in superconductors, are being investigated as potential candidates for scalable and universal quantum computing. Key properties include long-lived quantum states and the ability to interface with quantum systems at other nodes in a network. In the case of superconducting qubits, a particularly promising platform operating at microwave frequencies, long-distance connectivity via optical links requires quantum-coherent conversion. Such quantum transduction entails the conversion of quantum information from one form to another without destroying the quantum correlations and is a crucial component of quantum networks, where information needs to be transmitted over long distances.

Quantum optomechanics could be a potential approach for quantum transduction, provided that we can achieve a regime where the quantum interaction is comparable or dominates over the environmental noise. This regime is achieved routinely in state-of-the-art experiments. In addition, optomechanical systems are able to be coupled to various frequency ranges of the electromagnetic spectrum.

Soft-clamped membranes that have been derived by Tsaturyan *et al.*, 2017 represent one mechanical design that is particularly suitable for this purpose. Due to their low mechanical damping, these systems have low coupling to the thermal bath, making them a promising candidate for quantum memory and transduction applications in superconducting qubit systems. In this thesis, we explore their suitability for quantum memory and transduction, leading to an understanding of their potential to enable a new frontier in quantum technology.

In the remainder of this chapter, we will describe the promises and challenges of superconducting qubits as quantum computing platforms, showing a need for quantum transduction, and we will present recent experimental results towards quantum transduction on various physical platforms.

1.1 Superconducting Quantum Computing

Superconducting qubits have emerged as a compelling candidate for achieving universal quantum computing, rooted in the discoveries of superconductivity by Onnes in 1911 and the Josephson effect by Josephson in 1962 [Onnes, 1911; Josephson, 1962]. These phenomena underpin the design and operation of superconducting qubits in the microwave regime. Despite challenges, early implementations established new interest in the field about twenty years ago [Nakamura *et al.*, 1999; Devoret and Martinis, 2004]. This progression underscores superconducting qubits' potential as a robust platform for quantum computing and is experiencing tremendous interest from researchers and industries [Kim *et al.*, 2023].

1.1.1 DiVincenzo Criteria and Superconducting Qubits

To enter a more detailed assessment of the potential of superconducting qubits, we here review the DiVincenzo criteria, established by physicist David P. DiVincenzo in 2000, which are five practical and two communication requirements that any physical implementation of a quantum computer must satisfy [DiVincenzo and IBM, 2000]. This section assesses how superconducting qubits align with these criteria and contrasts them with other quantum computing platforms.

1. **Well-defined qubits:** Superconducting qubits, often constructed as nonlinear LC oscillators, fulfill this criterion. The nonlinearity results in an anharmonic potential, allowing for distinguishable states – as opposed to any harmonic oscillator whose Fock states cannot represent a qubit

due to the inability to single out which states are populated. Their states are defined by the number of Cooper pairs tunneling across a Josephson junction. In comparison, platforms such as trapped ions also offer well-defined qubits through internal energy levels of ions [Blatt and Wineland, 2008].

2. **State Preparation:** Superconducting qubits can be initialized into a known state (usually the ground state) using a technique called refrigeration, where a control voltage is used to ensure preparation in the ground state $|0\rangle$ as the initial state. Similar initialization is achievable in platforms like trapped ions, where 'repump' lasers initialize a particular electron state.

3. **Long coherence times:** Superconducting qubits have historically struggled with this criterion, but significant advancements have been made [Kjaergaard *et al.*, 2020]. As of today, coherence times have reached the order of 100 microseconds. Such a timescale is, however, still shorter than those of other platforms like trapped ions, which can have coherence times of several seconds [Harty *et al.*, 2014].

4. **Universal gate set:** A combination of single-qubit rotations and a two-qubit entangling operation that can then provide a universal set of gates has been demonstrated for superconducting qubits with high gate fidelity [Barends *et al.*, 2014].

5. **Qubit measurement:** Superconducting qubits can be measured using a method called a quantum non-demolition (QND) measurement [Clarke and Wilhelm, 2008], among others.

6. **Faithful transmission of quantum states (communication criterion):** This criterion is more challenging for superconducting qubits, as they are stationary on a chip. Since their resonance frequencies are in the few-GHz regime, they have to be cooled down to less than 100s of milliKelvin in order not to be dominated by thermal noise, i.e., $\hbar\omega > k_{\mathrm{B}}T$. Their transmission is therefore hindered in this frequency regime. Cryogenic links have been demonstrated over several meters [Magnard *et al.*, 2020] but appear challenging for larger-scale quantum networks. Instead, quantum states could be transduced to photons for transmission, an

active field of research for which this thesis discusses the suitability of soft-clamped membranes as transducers. Photonic quantum computing, however, inherently excels in this area due to its high electromagnetic frequency, which interacts weakly with the environment.

7. **Scalability (communication criterion):** Superconducting qubits have shown considerable promise in terms of scalability due to their solid-state nature and compatibility with traditional microfabrication techniques [Kjaergaard *et al.*, 2020]. However, as cryogenic cooling power is limited in dilution refrigerators, higher scaling will require linking several cryogenic systems, potentially via a quantum transducer, as discussed in the previous criterion. This stands in contrast to platforms such as trapped ions, where scalability remains a significant challenge due to the complexity of ion manipulation at large scales [Blatt and Wineland, 2008].

In conclusion, while superconducting qubits fulfill many of DiVincenzo's criteria, challenges remain in areas such as increasing coherence times and facilitating faithful transmission of quantum states. As research progresses in these areas, the potential of superconducting qubits to be the foundation of practical quantum computers continues to grow. This thesis discusses the suitability of soft-clamped membrane resonators for advancing this goal.

1.2 Quantum Transduction

As described by the DiVincenzo criteria, achieving quantum transduction from the microwave domain of superconducting qubits to the optical domain remains an outstanding goal for practical quantum computing. Meanwhile, quantum transducers are also relevant for other applications such as metrology [Kómár *et al.*, 2014]. While significant progress has been made in developing microwave-to-optical transducers, several challenges remain to be addressed to achieve high-efficiency, high-fidelity transduction. In this section, we discuss the figures of merit associated with microwave-to-optical transduction.

1.2.1 Figures of Merit

The most crucial parameters in quantum transduction are the efficiency, i.e., the efficiency that an incoming quantum generates an outgoing quantum, and the added noise level, quantifying the signal-to-noise ratio or the fidelity of the transduction scheme [Zeuthen *et al.*, 2020]. While to date, no experimental transduction platform has simultaneously demonstrated near unity efficiency and an added noise level <1, several systems are approaching these numbers [Brubaker *et al.*, 2022; Sahu *et al.*, 2023]. In the meantime, discussions have focused on practical applications of transducers, which add the bandwidth and/or the repetition rate as an additional figure of merit [Wang *et al.*, 2022; Delaney *et al.*, 2022]. This allows calculating the rate with which a superconducting qubit can be converted to an optical signal with high fidelity and vice-versa.

1.3 Experimental Platforms Suitable for Transduction

This section discusses the leading experimental platforms for microwave-to-optical transduction, including Rydberg atoms, electro-optic modulation, magneto-optic modulation, piezoelectric modulation, and electro-optomechanical transduction. An excellent summary used as a resource for this section is: Lauk *et al.*, 2020. I also highlight recent progress in each area and the ongoing research to improve microwave-to-optical transducer efficiency and noise level. At the end of this section, a table shows the state-of-the-art figures of merit for each experimental platform.

1.3.1 Rydberg Atoms

Transduction can be implemented using Rydberg atoms, atoms excited to a high quantum number n. A crucial characteristic of these atoms is their ability to be optically and microwave-addressable, enabling efficient microwave-to-optical conversion. This is due to the Rydberg states' large dipole moments, allowing for strong interactions with single microwave photons.

However, challenges exist in transduction using Rydberg atoms. One primary issue is the requirement for the atom to be positioned very close to the microwave source or resonant cavity. A large atomic ensemble may also be necessary to enhance the coupling. This proximity requirement can conflict with the necessity for laser cooling and trapping in a cryogenic environment.

Moreover, the lifetime of Rydberg states, which scales approximately as the cube of the principal quantum number, prevents the establishment of steady-state atomic polarization in states coupled to the microwave field. This eliminates the possibility of collective enhancement of the microwave transition in the single-photon regime, hence requiring a compromise between coupling strength and distance from surfaces. These issues seem to have limited experimental progress on cold atom-based transduction [Vogt *et al.*, 2019; Covey *et al.*, 2023].

1.3.2 Electro-Optic Modulation

Electro-optic modulation is a promising technique for microwave-to-optical transduction, as it can achieve high conversion efficiency and low-noise operation. This approach relies on the electro-optic effect, which describes the change in the refractive index of a material in response to an applied electric field. Electro-optic modulators, such as lithium niobate ($LiNbO_3$) waveguides, can convert microwave signals into optical signals by modulating the phase or amplitude of an optical field.

Advancements in electro-optic modulation include the development of integrated electro-optic modulators with high conversion efficiency [Fan *et al.*, 2018].

1.3.3 Magneto-Optic Modulation

Magneto-optic modulation is another approach for microwave-to-optical transduction, which relies on the interaction between microwave and optical fields in magneto-optic materials, such as yttrium iron garnet (YIG). In this technique, a microwave signal is applied to a magneto-optic material, inducing a change in the material's refractive index and thus modulating the phase or amplitude of an optical field. However, coupling rates appear low, reaching efficiencies of only about 10^{-3} [Hisatomi *et al.*, 2016].

1.3.4 Piezoelectric Transduction

Piezoelectric transduction is another promising experimental platform for microwave-to-optical conversion. This method leverages the piezoelectric effect to attain both electro- and opto-mechanical coupling through an intermediate mechanical system.

Several experiments using aluminum nitride (AlN) or lithium niobate ($LiNbO_3$) have been making relevant progress in achieving moderate efficiencies and added noise levels below 1 [Mirhosseini *et al.*, 2020; Meesala *et al.*, 2023]. While piezoelectric systems show large bandwidths of the transduction scheme, both AlN and $LiNbO_3$ systems suffer strong optically-induced heating (by metals, not the piezoelectric material) limiting the repetition rate of the transduction scheme in order to achieve noise levels <1 [Marinković *et al.*, 2021; Jiang *et al.*, 2022; Meesala *et al.*, 2023].

1.3.5 Electro-Optomechanical Transduction

Finally, electro-optomechanical transduction is yet another technique for microwave-to-optical transduction, which involves the conversion of quantum states between microwave and optical domains through mechanical intermediaries. Electro-Optomechanical systems, coupling both microwave and optical fields to the same mechanical resonators, can enable the coherent transfer of quantum states between these two domains [Midolo *et al.*, 2018].

With planar membrane resonators made of silicon nitride (SiN), this transduction technique has demonstrated the ability to achieve 47% efficiency in microwave-to-optical conversion at an added noise level of 3.2 [Brubaker *et al.*, 2022]. Interestingly, this platform has not been limited by optical absorption heating but instead by heating the resonator due to the microwave field, which also limited the bandwidth to less than 300 Hz. This thesis discusses how microwave coupling can be increased and characterizes the use of soft-clamped membranes for achieving lower added noise levels.

1.4 Quantum Memory

Quantum memories are systems of long-lived quantum states. Besides the need for quantum memories in quantum computing, quantum memories are needed to establish quantum repeaters for long-distance quantum communication [Lvovsky *et al.*, 2009]. Soft-clamped membranes are particularly suitable as quantum memory [Kristensen et al. 2023, in preparation] showing >100 ms coherence times [Seis *et al.*, 2022]. This thesis characterizes the optical absorption of soft-clamped membranes, which limits their coherence time for quantum memory, but longer storage times than planar membranes [Brubaker *et al.*, 2022; Seis *et al.*, 2022; Tsaturyan *et al.*, 2017].

In this chapter, we have delved into fundamental physical discoveries that lead to the emergence of superconducting quantum computing. We discussed the need for quantum transduction between microwave and optical fields – an objective yet to be fully realized, despite several physical platforms being strong contenders. In this light, soft-clamped membrane resonators appear as a promising platform for quantum transduction, offering weak interaction with the thermal environment, thus having an embedded quantum memory. Chapter 2 explores the basic principles of opto- and electromechanical interaction and derives the figures of merit for electro-optomechanical transduction. In Chapter 3, we measure the optical absorption effects of soft-clamped membranes with low effective mass at milliKelvin temperatures and compare their absorption heating against similar membrane designs. Chapter 4 presents the results of ground-state cooling of a soft-clamped membrane design, one that promises lower absorption heating and demonstrates coherence times exceeding 100 ms. Moreover, we have further optimized the electromechanical design, predicting a 50-fold improvement in electromechanical coupling. Chapter 5 shows the mechanical design considerations that have been taken for operating high-finesse optomechanical cavities at milliKelvin temperatures. Lastly, in Chapter 6, we demonstrate high-finesse cavity optomechanics, present optomechanical cooling of the soft-clamped membrane, and characterize the optical absorption heating.

Table 1.1: Summary of several recent transduction experiments. Here, EOM stands for Electro-optomechanics, Rep. rate for repetition rate, and OPAB for optical absorption induced heating.

Publication	Approach	Materials	Efficiency	Added Noise	Rep. Rate	Bandwidth	Limit
Hisatomi *et al.*, 2016	Magnon	YIG	10^{-3}	N/A	N/A	est. 1 MHz	Coupling
Fan *et al.*, 2018	Electro-Optics	AlN	$(25.9 \pm 0.3)\%$	3	N/A	0.59 MHz	Opt. Loss
Vogt *et al.*, 2019	Rydberg Atoms	Rb	5%	$\gg$1	N/A	$\gg$4 MHz	N/A
Mirhosseini *et al.*, 2020	Piezoelectric	Si+AlN	10^{-3}	0.57 ± 0.20	100 Hz	1 MHz	OPAB
Jiang *et al.*, 2022	Piezoelectric	Si-$LiNbO_3$+NbTiN	5%	99 ± 10	N/A	1.5 MHz	OPAB
Brubaker *et al.*, 2022	EOM	SiN+NbTiN	47%	3.2	CW	<300 Hz	MW Heat
Sahu *et al.*, 2022	Electro-Optics	$LiNbO_3$+Al	8.7%	0.16 ± 0.02	<500 Hz	18 MHz	OPAB
Sahu *et al.*, 2022	Electro-Optics	$LiNbO_3$+Al	15%	0.41 ± 0.02	<500 Hz	18 MHz	OPAB

2 Fundamentals on Cavity Opto- and Electromechanics

In this chapter, I am describing the fundamental physics of mechanical resonators and what needs to be considered to decouple them from their thermal environment. Afterwards, I show the relevant parameters of optical cavities and how optomechanical interactions are established. I then show how this translates to electromechanical systems, i.e., the coupling via electrostatic force instead of radiation pressure force. Finally, I am deriving the equations for the figures of merit of electro-optomechanical transduction.

2.1 Membrane Resonators

The displacement $x(t)$ of mechanical resonators can be described by the following equation of motion

$$m\frac{d^2x^2(t)}{dt^2} + m\Gamma_{\mathrm{m}}\frac{dx(t)}{dt} + m\Omega_{\mathrm{m}}^2 x(t) = F_{\mathrm{ex}}(t) \ , \tag{2.1}$$

where m is the resonator's mass, Γ_{m} the damping rate, Ω_{m} the resonance frequency, and F_{ex} any external driving force. Fig. 2.1 shows a pendulum as an example of a mechanical oscillator. Here, the damping rate Γ_{m} corresponds to the loss in amplitude of the oscillation over time. In the frequency domain,

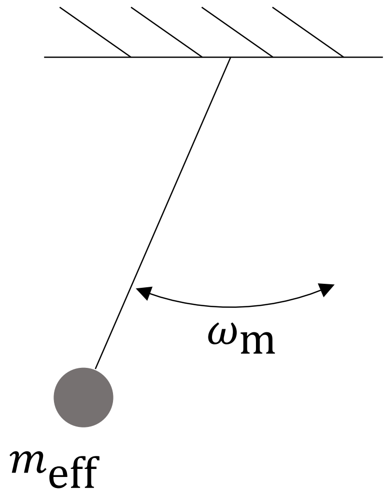

Figure 2.1: Pendulum as an example of a mechanical oscillator. A mass m_eff is suspended from a rope oscillating at a frequency ω_m. The damping rate Γ_m is dominated by air resistance.

the response of the mechanical resonator to an external force can be described by its response curve, its susceptibility, given by

$$\chi_\mathrm{m}(\omega) = \left(m_\mathrm{eff}\left(\Omega_\mathrm{m}^2 - \omega^2\right) - i m_\mathrm{eff}\Gamma_\mathrm{m}\omega\right)^{-1} , \tag{2.2}$$

where m_eff is the effective mass of the specific resonator mode.

In the quantum regime, the displacement can be represented by phonon occupations described with the ladder operators $\hat{b}$ and turns the spatial variable of Eq. 2.1 into

$$\hat{x} = x_\mathrm{zpf}\left(\hat{b} + \hat{b}^\dagger\right) , \tag{2.3}$$

where x_zpf is the zero-point fluctuation, i.e., the ground-state fluctuation, given by

$$x_\mathrm{zpf} = \sqrt{\frac{\hbar}{2 m_\mathrm{eff}\Omega_\mathrm{m}}} . \tag{2.4}$$

The Hamiltonian is

$$\hat{H} = \hbar\Omega_\mathrm{m}\hat{b}^\dagger\hat{b} + \frac{1}{2}\hbar\Omega_\mathrm{m} , \tag{2.5}$$

and the equations of motion can easily be calculated via Hamilton's equations. To conduct tests using specific states of a mechanical resonator, we must lower the energy level and minimize the interaction with the surrounding environment, which can lead to heat exchange. The bath occupation of the environment is given by the Bose-Einstein distribution

$$\bar{n}_{\text{th}} = \frac{1}{e^{\hbar\Omega_{\text{m}}/k_{\text{B}}T} - 1} \approx \frac{k_B T_{\text{bath}}}{\hbar\Omega_{\text{m}}} , \tag{2.6}$$

where the approximation holds in the high temperature limit $k_B T_{\text{bath}} \gg \hbar\Omega_{\text{m}}$. The thermal bath coupling is then given by

$$\bar{n}_{\text{th}}\Gamma_{\text{m}} = \frac{k_B T_{\text{bath}}}{\hbar Q} , \tag{2.7}$$

where the quality factor Q is given by $\Omega_{\text{m}}/\Gamma_{\text{m}}$. It is desirable to operate mechanical resonators at low bath temperatures to achieve low bath coupling and design them to possess high quality factors.

By its relation to resonance frequency and decay rate, the quality factor, Q, is defined as the ratio of energy loss per cycle ΔW to the total energy stored in the system $2\pi W$:

$$Q^{-1} = \frac{\Delta W}{2\pi W} . \tag{2.8}$$

The individual contributions to energy loss can be divided into intrinsic (such as thermoelastic damping) and extrinsic sources (such as gas damping of the environment) [Tsaturyan, 2019] that sum up for a resulting measurable quality factor as

$$Q^{-1} = \sum_i Q_i^{-1} = Q_{\text{extrinsic}}^{-1} + Q_{\text{intrinsic}}^{-1} . \tag{2.9}$$

As mechanical resonators in this thesis, we use thin-film silicon nitride (SiN) membranes with a hexagonal phononic crystal structure of holes in the material around the mechanical resonator pad towards the membrane frame as shown in Fig. 2.2. This phononic structure is designed with a unit cell size that makes the material less susceptible to allow the propagation of a certain frequency range, opening a 'phononic bandgap' [Maldovan, 2013] as shown in Fig. 2.2(b) to the left. Now the size and shape of the defect, the mechanically resonating pad, can be designed to possess its resonance frequencies within this bandgap, as shown in Fig. 2.2(b) to the right. This reduces phonon tunneling through the phononic crystal structure, an extrinsic loss, between the bulk material of the membrane frame to the resonator significantly compared to for example, trampoline membranes and plane membranes [Tsaturyan *et al.*, 2017]. From a theoretical perspective, we can thus focus on intrinsic losses, i.e., the internal dissipation of the material derived from the imaginary part of the Young's modulus.

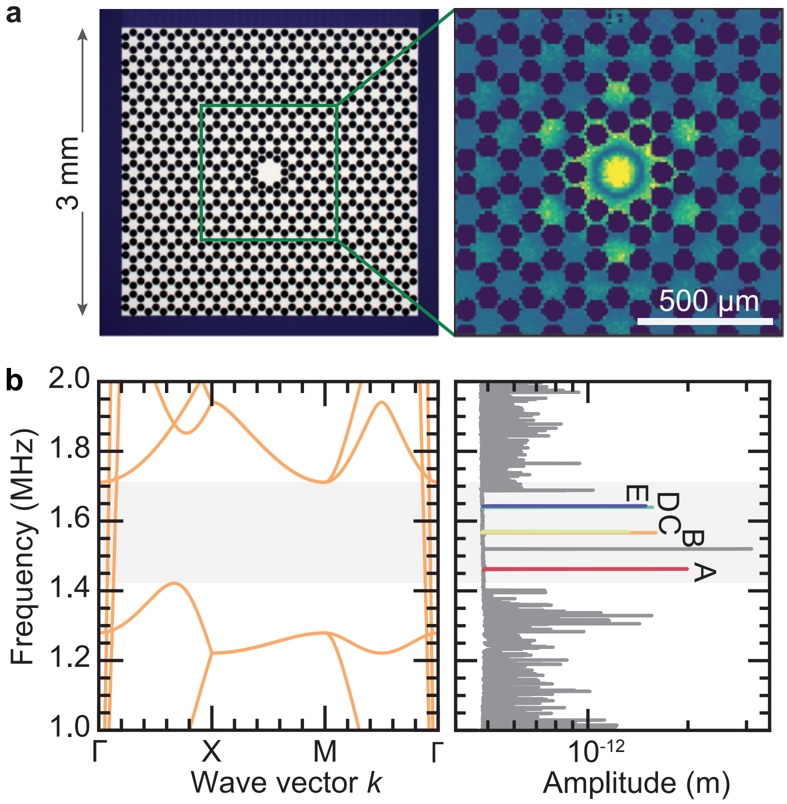

Figure 2.2: "(a) Micrograph of a silicon nitride membrane patterned with a phononic crystal structure (left) and measured out-of-plane displacement pattern of the first localized mode A (right) of a device with the lattice constant $a = 160$ m. (c) Simulated band diagram of a unit cell (left) and measured Brownian motion in the central part of the device shown in a. Localized modes A–E are colour coded, and the peak around 1.5 MHz is an injected tone for calibration of the displacement amplitude." Figure and caption from Tsaturyan *et al.*, 2017

The Young's modulus E represents the inherent stiffness of a material. It is defined as the ratio of stress σ to strain ϵ as follows:

$$E = \frac{\sigma}{\epsilon}, \tag{2.10}$$

where σ denotes the applied stress and ϵ corresponds to the induced strain in the material. The imaginary part of the Young's modulus E_{imag}, contributes to the amount of mechanical work done per cycle, i.e., $\Delta W \propto E_{\text{imag}}$. This implies that E_{imag} is associated with energy dissipation in the material. This energy dissipation introduces a loss term and influences the definition of the quality factor. In our design, the deposition of the membrane material occurs highly stressed, i.e., the main source of loss is bending losses instead of elongation losses, omit

$$\epsilon_0 = \epsilon_0^{\text{elong}} + \epsilon_0^{\text{bend}} \approx \epsilon_0^{\text{bend}} \,. \tag{2.11}$$

We thus expect the mechanical work to primarely derive from bending that can be described by the second derivative of the displacement function $u(x, y)$ in the form of:

$$\Delta W \approx \int \frac{\pi E_{\text{imag}}}{1-\nu^2} z^2 \left(\partial_x^2 u + \partial_y^2 u\right)^2 \mathrm{d}V \tag{2.12}$$

$$W \approx \int \frac{\bar{\sigma}}{2} \left(\left(\partial_x^2 u\right)^2 + \left(\partial_y^2 u\right)^2\right) \mathrm{d}V \,, \tag{2.13}$$

where ν is the Poisson ratio [Tsaturyan *et al.*, 2017], the ratio between transverse and axial strain. For a plane membrane, it results in a loss of

$$Q^{-1} \approx 2\sqrt{\frac{E_{\text{real}}}{12\bar{\sigma}}} \frac{h}{L} Q_{\text{int}}^{-1}, \tag{2.14}$$

where h is the thickness of the membrane, L is its length, and Q_{int}^{-1} is the loss solely given by the imaginary part of the Young's modulus, i.e., $Q_{\text{int}}^{-1} = E_{\text{imag}}/E_{\text{real}}$. For sufficiently large pre-stress $\bar{\sigma}$, the loss can be significantly reduced, which is referred to as 'dissipation dilution' [Tsaturyan *et al.*, 2017].

In addition, the phononic crystal structure around a mechanical defect changes the boundary conditions. In a standard plane material, the boundary condition between the membrane and the bulk material it is clamped to becomes

$$u\left(\vec{r}_{\text{cl}}\right) = \left(\vec{n}_{\text{cl}} \cdot \nabla\right) u\left(\vec{r}_{\text{cl}}\right) = 0 \,, \tag{2.15}$$

where $\vec{r}_{\text{cl}}$ gives the position of clamping between membrane and bulk material, and $\vec{n}_{\text{cl}}$ is the out-of-plane vector. This means that the displacement at the position of the clamp has to be zero. However, this boundary condition does not hold for a phononic crystal structure. Instead, the displacement and their derivative have to be continuous. This corresponds to

$$u_{\mathrm{d}}\left(\vec{r}_{\mathrm{cl}}\right)=u_{\mathrm{pc}}\left(\vec{r}_{\mathrm{cl}}\right) \tag{2.16}$$

$$\left(\vec{n}_{\mathrm{cl}}\cdot\nabla\right)u_{\mathrm{d}}\left(\vec{r}_{\mathrm{cl}}\right)=\left(\vec{n}_{\mathrm{cl}}\cdot\nabla\right)u_{\mathrm{pc}}\left(\vec{r}_{\mathrm{cl}}\right)\ , \tag{2.17}$$

where u_{d} is the displacement of the defect and u_{pc} is the displacement of the phononic crystal.

If the phononic crystal structure supports this weak clamping of the defect mode, then we refer to it as 'soft clamping' [Tsaturyan *et al.*, 2017]. This enables a significant reduction in bending loss, allowing to reach quality factors of $>10^8$ [Tsaturyan *et al.*, 2017; Seis *et al.*, 2022]. One such device is depicted in Fig. 2.3(a).

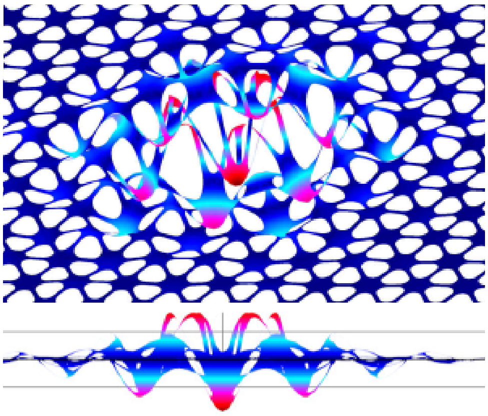

(a)

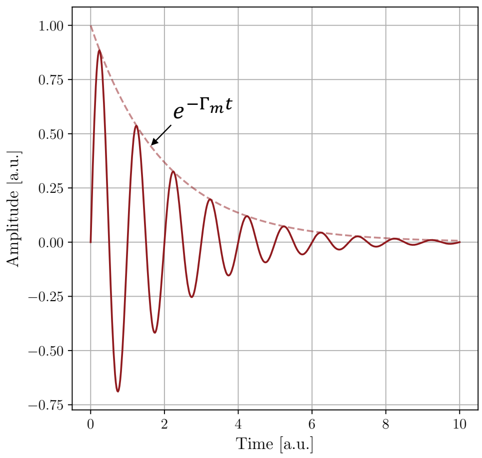

(b)

Figure 2.3: (a) COMSOL simulation of a high-Q membrane, where the hole structure opens a band gap only allowing one isolated out of plane mode at the defect at the center of the membrane, here with $Q>10^8$ (Seis *et al.*, 2022). The amplitude decays slowly over several unit cells, reducing clamping losses. This can be seen by the chosen colormap showing low displacement in blue and high displacement in red. (b) Demonstration of how the mechanical decay rate Γ_{m} is related to the amplitude of a mechanical resonator.

2.2 Cavity Optomechanics

This section describes the fundamentals of optomechanical interaction, i.e., the interaction between photonic and phononic fields, and its consequences. I start by describing optical cavities, how optomechanical interaction is established, and how this can be exploited for optomechanical cooling. However, this coupling results additionally in heating effects to the mechanical device.

2.2.1 Optical Cavities

Optical cavities can be characterized by their cavity linewidth κ, free-spectral range ω_{FSR}, and finesse F, connected via

$$F = \frac{\omega_{\mathrm{FSR}}}{\kappa} \, . \tag{2.18}$$

The finesse corresponds to the average number of round trips for a photon, while ω_{FSR} gives the frequency difference between two cavity resonances fulfilling the standing wave condition. The linewidth κ gives the total cavity loss rate that corresponds to two times the full width at half maximum (FWHM) of the cavity response. Fig. 2.4 shows a schematic of the relevant units to characterize an optical cavity.

The equation of motion for the photonic field operator $\hat{a}$ inside the cavity is given by

$$\dot{\hat{a}} = -\frac{\kappa}{2}\hat{a} + i\Delta\hat{a} + \sqrt{\kappa_{\mathrm{ex}}}\hat{a}_{\mathrm{in}} + \sqrt{\kappa_0}\hat{f}_{\mathrm{in}} \, , \tag{2.19}$$

where Δ is the frequency detuning of the laser to the from cavity resonance as in Fig. 2.4(b), κ_{ex} is the external input coupling rate, $\hat{a}_{\mathrm{in}}$ is the cavity input field, κ_0 is the coupling rate of quantum noise $\hat{f}_{\mathrm{in}}$ [Aspelmeyer *et al.*, 2014]. When calculating the steady-state solution of this equation ($\dot{\hat{a}} = 0$), the cavity response curve, susceptibility results in

$$\chi_{\mathrm{opt}}(\omega) = \frac{1}{-i(\omega + \Delta) + \kappa/2} \tag{2.20}$$

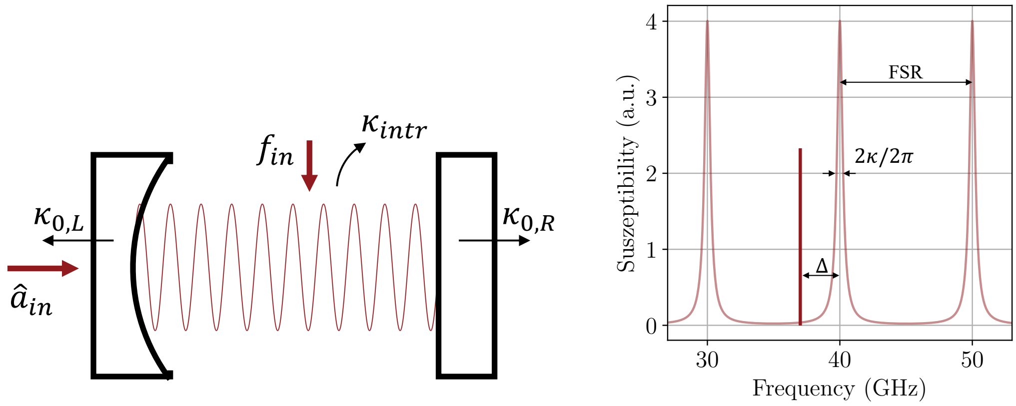

(a) (b)

Figure 2.4: (a) Schematic of an optical cavity. On resonance, the incoupling light field $\hat{a}$ creates a resonant standing wave inside the cavity. The individual cavity loss contributions sum up to a total loss of $\kappa = \kappa_{0,L} + \kappa_{0,R} + \kappa_{intr}$. (b) Spectrum of the frequency response of an optical cavity, i.e., $|\chi_{\mathrm{opt}}|^2$ of the cavity suszeptibility χ_{opt} showing three free spectral ranges. The red bar indicates a laser beam operating at a detuning from cavity resonance Δ.

that is drawn as $|\chi_{\mathrm{opt}}|^2$ in Fig. 2.4(b), proportional to the the intracavity field

$$\bar{n}_{\mathrm{cav}} = \langle \hat{a}^\dagger \hat{a} \rangle = \frac{\kappa_{\mathrm{ex}}}{\Delta^2 + (\kappa/2)^2} \frac{P}{\hbar\omega_{\mathrm{L}}} \eta \, , \tag{2.21}$$

where P is the photonic input power at frequency ω_{L}, and η is the mode-matching factor between the laser input mode and the cavity mode.

Non-confined cavity modes can be described by a larger set of spacial cavity modes that depend strongly on the parameters of the incoupling beam. While beam divergence introduces rotational symmetric modes, referred to as Laguerre-Gaussian modes, any reflection on a planar surface with a tilt introduces coupling to rectangular modes, referred to as Hermite-Gaussian modes [Østfeldt, 2022; Pampaloni and Enderlein, 2004].

For the fundamental cavity mode (Gaussian beam profile) of a near hemispherical cavity, meaning one curved and one plane mirror, the beam waist w_0 can be easily found via the Rayleigh range z_{R} and the radius of curvature of the beam $R(z)$ that is set by the radius of the curved mirror. The equation to be solved then turns into

$$R(z) = z\left(1 + \left(\frac{z_{\mathrm{R}}}{z}\right)^2\right) \text{ with } z_{\mathrm{R}} = \frac{\pi\omega_0^2 n}{\lambda}\,, \tag{2.22}$$

where z is the position from the plane mirror, n is the index of the refraction of the medium ($n = 1$ in vacuum), and λ the laser wavelength.

2.2.2 Optomechanical Interaction

When a partially reflective mechanical resonator is placed within the standing wave of an optical field, the device experiences a radiation-pressure force, which derives from the momentum transfer upon reflection of $\Delta p = 2\hbar k$ per photon and per round trip with the wavenumber k. This leads to an average force of

$$\langle F\rangle = \Delta p\frac{\bar{n}_{\mathrm{cav}}}{\tau_{\mathrm{r}}} = \Delta p\frac{c\bar{n}_{\mathrm{cav}}}{L}\,, \tag{2.23}$$

where τ_{r} is the round-trip time, c is the speed of light, and L is the cavity length. Moreover, this partially reflective mechanical device partitions the optical in two sub-cavities. The momentum transfer upon reflection that causes a displacement of the mechanical resonator, in turn changes the resonance frequency condition of the optical cavity. A schematic of such an interacting system is shown in Fig. 5.8. The change in resonance frequency due to the

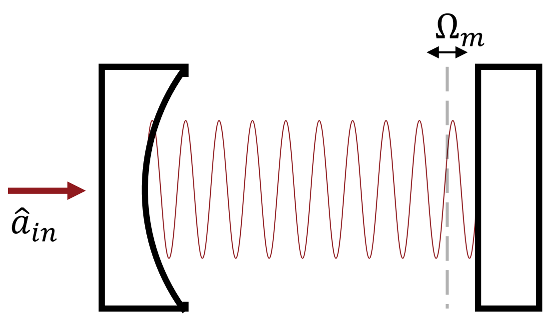

Figure 2.5: Schematic of an optomechanical cavity with a mechanical membrane resonator depicted as a gray dashed line close to the flat cavity mirror. The gradient of the intracavity power of the standing wave induces a force acting on the membrane resonator, and the displacement of the resonator results in a change in the optical length of the cavity, resulting in a change in resonance frequency $\omega_{\mathrm{cav}}(x)$

displacement x of the mechanical resonator can be described by a Taylor expansion

$$\omega_{\text{cav}}(x) \approx \omega_{\text{cav}} + x\frac{\partial \omega_{\text{cav}}}{\partial x} + \ldots \,. \tag{2.24}$$

We define $G := -\partial\omega_{\text{cav}}/\partial x$. Often, the beyond first-order terms can be neglected due to small displacements but are subject of studies, too [Metzger *et al.*, 2008]. This modulation of the cavity resonance frequency introduces an interaction term between mechanics and optics:

$$\hat{H} = \hbar\Omega_{\text{m}}\hat{b}^\dagger\hat{b} + \hbar\omega_{\text{cav}}(x)\hat{a}^\dagger\hat{a} \tag{2.25}$$

$$\approx \hbar\Omega_{\text{m}}\hat{b}^\dagger\hat{b} + \hbar\left(\omega_{\text{cav}} - G\hat{x}\right)\hat{a}^\dagger\hat{a} \tag{2.26}$$

$$= \hbar\Omega_{\text{m}}\hat{b}^\dagger\hat{b} + \hbar\omega_{\text{cav}}\hat{a}^\dagger\hat{a} - \hbar g_0\hat{a}^\dagger\hat{a}\left(\hat{b} + \hat{b}^\dagger\right) \,, \tag{2.27}$$

where $g_0 = Gx_{\text{zpf}}$ is called the single-photon coupling strength, and x_{zpf} is defined as in Eq. 2.4 [Aspelmeyer *et al.*, 2014].

We can model the optomechanical behavior with linear terms when observing only weak dynamics that the mechanics introduce to the steady field, i.e., in the form of

$$\hat{a} = \bar{a} + \delta\hat{a} \tag{2.28}$$

$$\hat{x} = \bar{x} + \delta\hat{x} \,. \tag{2.29}$$

By calculating the time evolution of the operator, we result in the Heisenberg-Langevin equation:

$$\frac{d}{dt}\delta\hat{a} = \frac{1}{i\hbar}\left[\hat{a}, \hat{H}\right] = \left(i\Delta - \frac{\kappa}{2}\right)\delta\hat{a}(t) - iG\bar{a}\delta\hat{x}(t) \,. \tag{2.30}$$

The fluctuation of $\hat{x}$ with the mechanical frequency ($\delta\hat{x}(t) = x_0 \sin\Omega_{\text{m}}t$) causes the creation of sidebands in the rotating frame onto the optical field in the form of

$$\delta\hat{a}(t) = A_- \exp\left(-i\Omega_{\text{m}}t\right) + A_+ \exp\left(i\Omega_{\text{m}}t\right) \,, \tag{2.31}$$

where the amplitudes A_- and A_+ depend on the cavity enhancement of the sidebands as described by the susceptibility in Eq. 2.20. With $\delta\hat{x} = x_{\mathrm{zpf}}\left(\delta\hat{b} + \delta\hat{b}^\dagger\right)$, the optomechanical (om) interaction Hamiltonian of the linearized terms turns into

$$H_{\mathrm{lin,om}} = \hbar g_0 \bar{a}\left(\delta\hat{b} + \delta\hat{b}^\dagger\right)\left(\delta\hat{a} + \delta\hat{a}^\dagger\right) \ . \tag{2.32}$$

As the amplitude of the sidebands depends on their cavity detuning, we observe an enhanced positive sideband for a red-detuned light field and vice versa. In detail, for a red-detuned operation ($\Delta < 0$), the most dominant terms of the Hamiltonian become

$$\hbar g_0 \bar{a}\left(\delta\hat{b}^\dagger \delta\hat{a} + \delta\hat{b}\delta\hat{a}^\dagger\right) \ . \tag{2.33}$$

This form of Hamiltonian is also referred to as beam-splitter Hamiltonian. It induces the annihilation of a phonon by creating a photon and vice versa.

For a blue-detuned operation (Δ >0), the most dominant terms of the Hamiltonian become

$$\hbar g_0 \bar{a}\left(\delta\hat{b}^\dagger \delta\hat{a}^\dagger + \delta\hat{b}\delta\hat{a}\right) \ . \tag{2.34}$$

This operator, which induces the creation or annihilation of photon-phonon pairs, has the form of a squeezing operator.

2.2.3 Dynamical Backaction

The mechanical resonator's interaction with the optical cavity induces an additional phenomenon. We described in the previous section that the optomechanical interaction gives rise to two optical sidebands at the mechanical frequency. Those sidebands, in turn, act as a driving force on the mechanical resonator, which changes the mechanical susceptibility described in Eq. 2.2 to

$$\chi_{\mathrm{m,eff}}^{-1}(\omega) = \chi_{\mathrm{m}}^{-1}(\omega) + \Sigma(\omega) \ . \tag{2.35}$$

This dynamical modulation term $\Sigma(\omega)$, arising from the force of the optical sidebands, scales linearly with the intracavity power (as in Eq. 2.23) and is described by

$$\Sigma(\omega) = 2m_{\text{eff}}\Omega_{\text{m}}g^2 \left(\frac{1}{(\Delta+\omega)+i\kappa/2} + \frac{1}{(\Delta-\omega)-i\kappa/2} \right) , \tag{2.36}$$

where the two terms represent the amplitudes of the individual sidebands, and $g = \sqrt{n_{\text{cav}}}g_0$. The real part of $\Sigma(\omega)$ introduces a linear resonance frequency shift as in Eq. 2.2, also referred to as spring effect [Aspelmeyer *et al.*, 2014], and the imaginary part introduces an increase in mechanical damping in the form of

$$\delta\Omega_{\text{m}}(\omega) = \frac{\text{Re}\Sigma(\omega)}{2\omega m_{\text{eff}}} = g^2\frac{\Omega_{\text{m}}}{\omega} \left(\frac{\Delta+\omega}{(\Delta+\omega)^2+\kappa^2/4} + \frac{\Delta-\omega}{(\Delta-\omega)^2+\kappa^2/4} \right) , \tag{2.37}$$

$$\Gamma_{\text{opt}}(\omega) = -\frac{\text{Im}\Sigma(\omega)}{\omega m_{\text{eff}}} = g^2\frac{\Omega_{\text{m}}}{\omega} \left(\frac{\kappa}{(\Delta+\omega)^2+\kappa^2/4} - \frac{\kappa}{(\Delta-\omega)^2+\kappa^2/4} \right) . \tag{2.38}$$

Fig. 2.6 shows how dynamical backaction changes the mechanical resonance frequency and mechanical damping rate for different cavity linewidths. For an optical field close to the cavity resonance ($\Delta \approx 0$), the optomechanical coupling rate becomes

$$\Gamma_{\text{opt}} = \frac{4\bar{n}_{\text{cav}}g_0^2}{\kappa} . \tag{2.39}$$

This coupling rate can be compared to the coupling of the mechanical resonator to the thermal bath $\bar{n}_{\text{th}}\Gamma_{\text{m}}$. This can be expressed by the quantum cooperativity which is defined as the ratio of the two:

$$C_{\text{qu}} := \frac{\Gamma_{\text{opt}}}{\bar{n}_{\text{th}}\Gamma_{\text{m}}} . \tag{2.40}$$

For $C_{\text{qu}} \ll 1$, the occupation of the mechanical resonator is set by the thermal bath occupation $\bar{n}_{\text{th}}$, while for $C_{\text{qu}} \gg 1$ it allows to further cool the mechanics to the optical bath temperature. In order to achieve high coupling rates much larger than the coupling rate to a thermal bath $\bar{n}_{\text{th}}\Gamma_{\text{m}}$, it is, therefore, desirable to operate at a high coupling strength g_0, a narrow cavity linewidth κ, and at high cavity photon numbers $\bar{n}_{\text{cav}}$ as in Eq. 2.39. However, high cavity photon

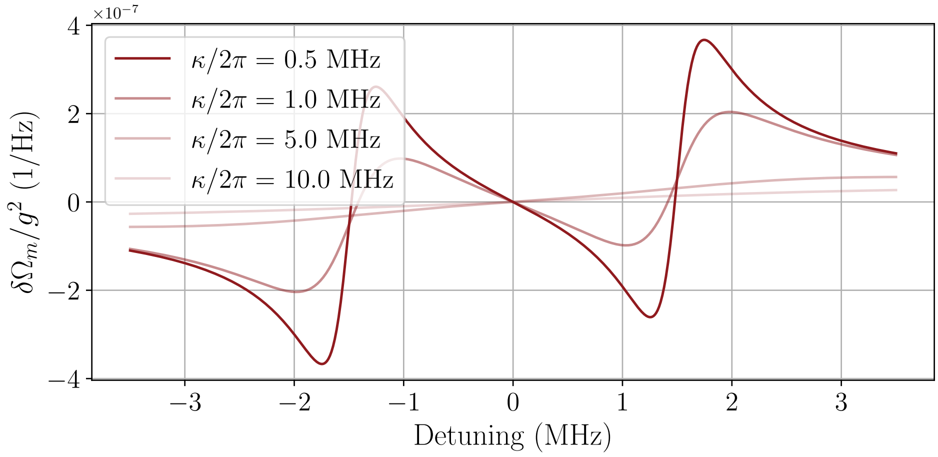

(a)

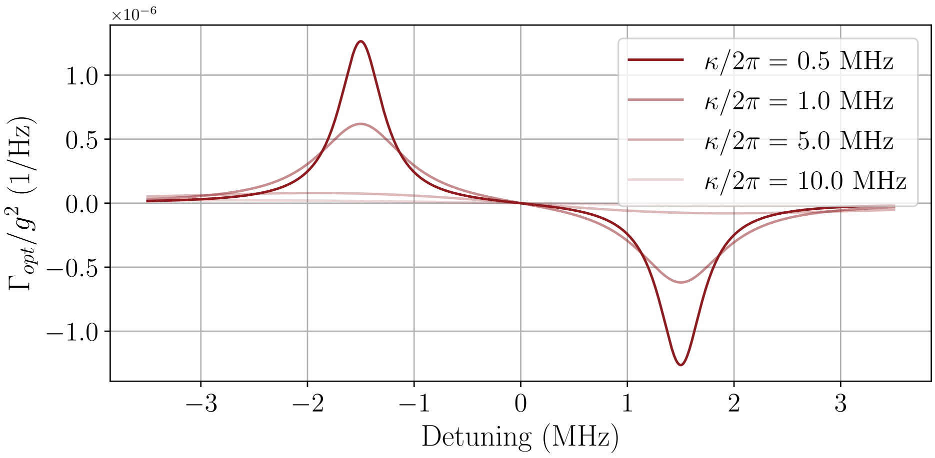

(b)

Figure 2.6: (a) Change in mechanical resonance frequency $\delta\Omega_{\mathrm{m}}$ due to the optical spring effect. For narrow cavity linewidth, additional zero-crossings arise. (b) Optomechanical damping rate Γ_{opt} due to dynamical backaction. For both subfigures, $\omega = \Omega_{\mathrm{m}} = 1.5$ MHz, and the frequencies are divided by g^2.

numbers lead to additional heating effects, as described in the following subsection.

2.2.4 Heating Effects

Several effects lead to induced heating of the mechanics, imposing challenges on reaching the mechanic's ground-state occupation through optomechanical interaction. One of them is the laser phase noise. It needs to be low so that the fluctuations it induces in the radiation-pressure force do not lead to optomechanical heating. A required limit on the allowable laser frequency noise $\bar{S}(\omega)$ to achieve ground-state cooling is set by [Rabl *et al.*, 2009; Aspelmeyer *et al.*, 2014]

$$\bar{S}(\Omega_{\mathrm{m}}) > \frac{g_0^2}{k_{\mathrm{B}}T/\hbar Q_{\mathrm{m}}} \,. \tag{2.41}$$

This requires using low phase/frequency noise laser/microwave sources, or alternatively, filter cavities.

In addition, and what is also being investigated in this thesis is the effect of optical absorption heating of the mechanical resonator. This arises from the imaginary part of the index of refraction of the mechanical resonator $n = n_{\mathrm{real}} + in_{\mathrm{imag}}$. For the propagating electromagnetic field E, this then causes an exponential decay of the field amplitude being absorbed in the material:

$$E(x) \propto e^{ikx} = e^{i2\pi nx/\lambda_{\mathrm{vac}}} = e^{2\pi in_{\mathrm{real}}x/\lambda_{\mathrm{vac}}} e^{-2\pi n_{\mathrm{imag}}/\lambda_{\mathrm{vac}}} \,, \tag{2.42}$$

where k is the wavenumber and λ_{vac} is the vacuum wavelength of the field. In practice, mechanical resonators are usually operated at cryogenic temperatures to reduce the thermal bath occupation. Despite the imaginary part of the index of refraction being around parts-per-million levels, experiments show that optical absorption heating can lead to resonator mode temperatures above the bath temperature. This is particularly true for mechanical resonators for which material has been removed between the resonator and bulk material, which reduces heat transfer. This is being discussed further in Chapters 3 and 6.

2.3 Electromechanics

Now we want to focus on mechanical interaction via electrostatic force instead of radiation pressure force discussed for optical fields earlier. One can derive the same interaction Hamiltonian that we have seen in Eq. 2.25 even though the interaction here is caused by an electrostatic force instead of radiation pressure force. Fig. 2.7 shows how such an interaction can be established. The

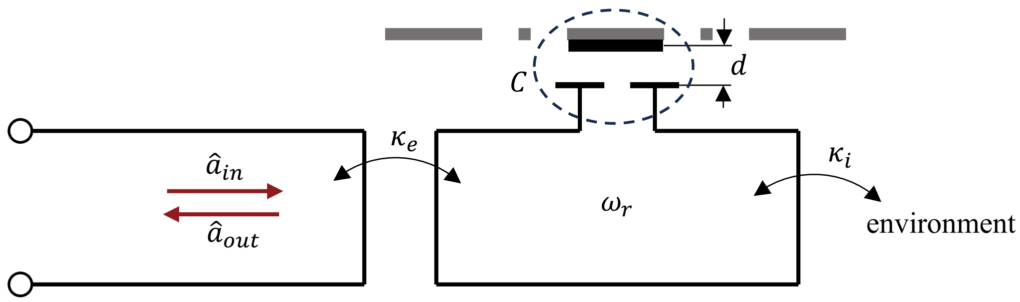

Figure 2.7: Schematic of an electromechanical cavity with a mechanical membrane resonator depicted as a gray dot-dashed line with an attached metal plate participating in the total capacitance. Electric fields $\hat{a}_{in}$ are inductively coupled into the cavity. At the capacitor C, the electric field causes a capacitative force acting on the mechanical resonator. In turn, the displacement of the membrane changes the total capacitance and, therefore, the resonance frequency of the electromechanical cavity.

resonance frequency of an electronic circuit is given by

$$\omega_{\mathrm{r}} = \frac{1}{\sqrt{LC}} , \tag{2.43}$$

where L is the inductance of the circuit and C the total capacitance. It consists of $C = C_{\mathrm{p}} + C_{\mathrm{m}}(x)$, where C_{p} is some parasitic capacitance and $C_m(x)$, the capacitance that the metalization on the mechanical resonator contributes to, by

$$C_{\mathrm{m}}(x) = \frac{\epsilon_0}{2} \frac{A}{d+x} , \tag{2.44}$$

"where ϵ_0 is the vacuum permittivity, x is the amplitude of mechanical motion" [Seis, 2021], A the capacitor plate area building part of the capacitance, and d is the distance between the capacitor plates. This is an approximation for two infinite parallel plates, and where we neglect edge effects. The mechanical frequency shift is then linked to the capacitor as

$$G = \frac{d\omega_\mathrm{r}}{dx} = \frac{d\omega_\mathrm{r}}{dC}\frac{dC}{dC_\mathrm{m}}\frac{dC_\mathrm{m}}{dx} = \frac{-\omega_\mathrm{r}}{2C}\frac{dC}{dC_\mathrm{m}}\frac{-C_\mathrm{m}}{d} = \frac{dC}{dC_\mathrm{m}}\frac{C_\mathrm{m}}{C}\frac{\omega_\mathrm{r}}{2d} = \eta_C\frac{\omega_\mathrm{r}}{2d}\,, \tag{2.45}$$

where η_C is also referred to as participation ratio, i.e., the ratio C_m/C. Identical to the optomechanical coupling rate in Eq. 2.39, the electromechanical coupling rate is given by

$$\Gamma_\mathrm{em} = \frac{4\bar{n}_\mathrm{cav}g_0^2}{\kappa}\,, \tag{2.46}$$

where again $g_0 = Gx_\mathrm{zpf}$ with $x_\mathrm{zpf} = \sqrt{\hbar/2m_\mathrm{eff}\Omega_\mathrm{m}}$. It is therefore desirable to design an electromechanical system with a close to unity participation ratio, balancing the effective mass and capacitor plate area, keeping the distance d small without the capacitor plates collapsing during cooldown, and finally designing a narrow linewidth electric cavity.

2.4 Electro-Optomechanical Transduction

In the scope of quantum transducer practical applications, several figures of merit play key roles. These figures, which will be the main focus of this section, include efficiency, added noise, and transducer bandwidth. Each of these figures will be derived individually.

The first figure of merit, *efficiency*, relates to the probability of a successful conversion of a microwave photon to an optical photon and vice versa [Zeuthen *et al.*, 2020]. Next, we consider the *added noise level*, another important figure in the understanding of quantum transducers, relating to the fidelity of the transduction [Zeuthen *et al.*, 2020]. The third key figure is the *bandwidth* at which the transducer operates. Its role in the performance of a quantum transducer is significant, affecting the speed and reliability of the system [Lauk *et al.*, 2020].

Recently, a new figure of merit has emerged: the *quantum capacity*. This novel metric aims to encapsulate the mentioned figures of merit into a single figure that represents the qubit transfer rate [Wang *et al.*, 2022].

In what follows, the derivation of these figures of merit will be carried out based on internal notes by Thibault Capelle and the work presented in Andrews *et al.*, 2014.

2.4.1 Summary of the Derivation of the Transduction Efficiency

In an electro-optomechanical transducer, two photonic fields, one in the optical domain and one in the microwave domain, are coupled to the phononic field of a mechanical resonator. Fig. 2.8 shows the scheme of the participating fields that are used in the derivation below. The Hamiltonian of the two fields

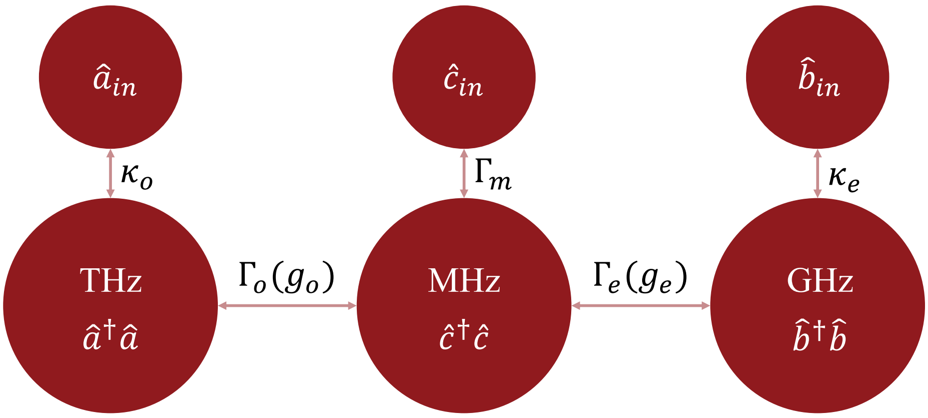

Figure 2.8: Scheme showing the coupling between the various fields participating in the transduction process. What will be of practical interest is the transmission and noise from $\hat{a}_{\text{in}}$ to $\hat{b}_{\text{out}}$ and vice versa.

being coupled to the resonator field $\hat{c}^\dagger\hat{c}$ is

$$\hat{H} = \hbar\omega_o\hat{a}^\dagger\hat{a} + \hbar\omega_e\hat{b}^\dagger\hat{b} + \hbar\omega_m\hat{c}^\dagger\hat{c} + \hbar g_o\hat{a}^\dagger\hat{a}\left(\hat{c}+\hat{c}^\dagger\right) + \hbar g_e\hat{b}^\dagger\hat{b}\left(\hat{c}^\dagger+\hat{c}\right), \quad (2.47)$$

where the suffixes o,e and m refer to the optical, microwave (electric), and mechanical modes, respectively. The time evolution for an operator $\hat{A}$ is

$$\frac{d}{dt}\hat{A} = \frac{1}{i\hbar}[\hat{A},\hat{H}]. \quad (2.48)$$

In addition, we can introduce the loss terms of the three fields. While the microwave field has intrinsic losses and only one channel for extrinsic losses, the optical cavity consists of two mirrors with loss terms, i.e., κ_{oL} and κ_{oR}. The losses are then for the optical field

$$\kappa_{\mathrm{o}} = \kappa_{\mathrm{oL}} + \kappa_{\mathrm{oR}} + \kappa_{\mathrm{o0}} \tag{2.49}$$

and for the microwave field

$$\kappa_{\mathrm{e}} = \kappa_{\mathrm{eR}} + \kappa_{\mathrm{e0}}\ , \tag{2.50}$$

while it is Γ_{m} for the mechanical field $\hat{c}^\dagger\hat{c}$. When linearizing around strong coherent pump fields both from the microwave and the optical side with a detuning off the resonance frequency $\Delta_{\mathrm{o/e}}$, we then get the following equations of motion:

$$\frac{d}{dt}\hat{a} = \left[-i\left(-\Delta_o + g_o\left(\gamma+\gamma^*\right)\right) - \kappa_o/2\right]\hat{a} - ig_o\alpha\left(\hat{c}+\hat{c}^\dagger\right) + \sqrt{\kappa_{\mathrm{oL}}}\hat{a}_{\mathrm{L,in}} + \sqrt{\kappa_{\mathrm{oR}}}\hat{a}_{\mathrm{R,in}} + \sqrt{\kappa_{\mathrm{o0}}}\hat{a}_{\mathrm{0,in}} \tag{2.51}$$

$$\frac{d}{dt}\hat{b} = \left[-i\left(-\Delta_e + g_e\left(\gamma+\gamma^*\right)\right) - \kappa_e/2\right]\hat{b} - ig_e\beta\left(\hat{c}+\hat{c}^\dagger\right) + \sqrt{\kappa_{\mathrm{ec}}}\hat{b}_{\mathrm{c,in}} + \sqrt{\kappa_{\mathrm{e0}}}\hat{b}_{\mathrm{0,in}} \tag{2.52}$$

$$\frac{d}{dt}\hat{c} = \left[-i\omega_m - \Gamma_m/2\right]\hat{c} - ig_o\left(\alpha^*\hat{a} + \alpha\hat{a}^\dagger\right) - ig_e\left(\beta^*\hat{b} + \beta\hat{b}^\dagger\right) + \sqrt{\Gamma_m}\hat{c}_{\mathrm{in}} \tag{2.53}$$

with corresponding equations of motion for complex conjugated and transposed field operators, i.e., $\hat{a}^\dagger$, $\hat{b}^\dagger$, and $\hat{c}^\dagger$. Here, α, β, and γ stand for the amplitudes of the coherent fields. The equations of motion can be summarized in a matrix form:

$$\frac{d}{dt}\mathbf{a} = A\mathbf{a} + B\mathbf{a}_{\mathrm{in}}, \tag{2.54}$$

where:

$$\mathbf{a} = \begin{pmatrix}\hat{a}, & \hat{a}^\dagger, & \hat{b}, & \hat{b}^\dagger, & \hat{c}, & \hat{c}^\dagger\end{pmatrix}^T \tag{2.55}$$

$$\mathbf{a}_{\mathrm{in}} = \begin{pmatrix}\hat{a}_{\mathrm{L}}, & \hat{a}_{\mathrm{R,in}}, & \hat{a}_{\mathrm{0,in}}, & \hat{a}^\dagger_{\mathrm{L,in}}, & \hat{a}^\dagger_{\mathrm{R,in}}, & \hat{a}^\dagger_{\mathrm{0,in}}, & \hat{b}_{\mathrm{c,in}}, & \hat{b}_{\mathrm{0,in}}, & \hat{b}^\dagger_{\mathrm{c,in}}, & \hat{b}^\dagger_{\mathrm{0,in}}, \\ \hat{c}_{\mathrm{in}}, & \hat{c}^\dagger_{\mathrm{in}} \end{pmatrix}^T \tag{2.56}$$

Here, $\mathbf{a}_{\text{in}}$ is meant to be a 1-column vector. Similarly, the input-output relations:

$$\hat{a}_{\text{L,out}} = -\hat{a}_{\text{L,in}} + \sqrt{\kappa_{\text{oL}}}\hat{a} \tag{2.57}$$
$$\hat{a}_{\text{R,out}} = -\hat{a}_{\text{R,in}} + \sqrt{\kappa_{\text{oR}}}\hat{a} \tag{2.58}$$
$$\hat{b}_{\text{c,out}} = -\hat{b}_{\text{c,in}} + \sqrt{\kappa_{\text{ec}}}\hat{b} \tag{2.59}$$

can be rewritten in the matrix form:

$$\mathbf{a}_{\text{out}} = C\mathbf{a} + D\mathbf{a}_{\text{in}}, \tag{2.60}$$

where:

$$\mathbf{a}_{\text{out}} = \left(\hat{a}_{\text{L,out}},\quad \hat{a}^{\dagger}_{\text{L,out}},\quad \hat{a}_{\text{R,out}},\quad \hat{a}^{\dagger}_{\text{R,out}},\quad \hat{b}_{\text{c,out}},\quad \hat{b}^{\dagger}_{\text{c,out}}\right)^{T}. \tag{2.61}$$

We can apply the Fourier transform to the equations above using

$$\mathcal{F}(f)[\omega] = \int_{-\infty}^{\infty} f(t)e^{-i\omega t}dt \tag{2.62}$$
$$f(t) = \int_{-\infty}^{\infty} \mathcal{F}(f)[\omega]e^{i\omega t}d\omega. \tag{2.63}$$

We obtain using Eq. 2.54 and 2.60:

$$(-i\omega I - A)a[\omega] = Ba_{\text{in}}[\omega] \tag{2.64}$$
$$a_{\text{out}}[\omega] = Ca[\omega] + Da_{\text{in}}[\omega], \tag{2.65}$$

where $a = \mathcal{F}(\mathbf{a})$, $a_{\text{in}} = \mathcal{F}(\mathbf{a}_{\text{in}})$ and $a_{\text{out}} = \mathcal{F}(\mathbf{a}_{\text{out}})$. This can be solved in the following way:

$$a_{\text{out}}[\omega] = \left[C(-i\omega I - A)^{-1}B + D\right] a_{\text{in}}[\omega] \tag{2.66}$$

By then performing the inversion of $(-i\omega I - A)$, which can be done as the determinant is non-zero, one can calculate the matrix that provides the coupling of all input fields to all output fields in the form of

$$a_{\text{out}}[\omega] = \left[C(-i\omega I - A)^{-1}B + D\right] a_{\text{in}}[\omega] = Ka_{\text{in}}[\omega], \tag{2.67}$$

The transduction coefficient is the coefficient linking $\hat{a}_{\text{L,out}}$ and $\hat{b}_{\text{c,in}}$. With the assumptions that we are operating in a regime where $\kappa_{o/e} \gg \Gamma_{o/e}$, $\Gamma_m \ll \Omega_m$, and red-detuned pump, detuned off cavity resonance by the detuning $\Delta_{o/e}$, we obtain

$$K_{\hat{a}_{\mathrm{L,out}},\hat{b}_{\mathrm{c,in}}} \approx \sqrt{\frac{\kappa_{\mathrm{ec}}}{\kappa_e}}\sqrt{\frac{\kappa_{\mathrm{oL}}}{\kappa_o}} \frac{\sqrt{\Gamma_e\Gamma_o\mathcal{A}_e\mathcal{A}_o}e^{-i\theta}}{-i\left(\Omega_m+\Omega_e+\Omega_o-\omega\right)-\left(\Gamma_m+\Gamma_e+\Gamma_o\right)/2}, \tag{2.68}$$

where

$$\mathcal{A}_{o/e} = \frac{\left(\frac{\kappa_{o/e}}{2}\right)^2+\left(\Delta_{o/e}-\Omega_m\right)^2}{-4\Delta_{o/e}\Omega_m} \tag{2.69}$$

$$\theta = -\theta_\beta+\theta_\alpha+\theta_e+\theta_o \tag{2.70}$$

$$\theta_{o/e} = \arctan\left(\frac{\Delta_{o/e}+\Omega_m}{\kappa_{o/e}/2}\right) \tag{2.71}$$

$$\alpha/\beta = |\alpha/\beta|e^{i\theta_{\alpha/\beta}}. \tag{2.72}$$

The coefficient for calculating the transmission of an optical signal to a microwave signal, $\hat{a}_{\mathrm{L,in}}$ to $\hat{b}_{\mathrm{c,out}}$, remains identical. For pump fields close to $\Delta_{o/e} = -\Omega_{\mathrm{m}}$, sideband-resolution in the form of $\kappa_{o/e} < \Omega_{\mathrm{m}}$, and strong overcoupling, the transmission efficiency η results in

$$\eta = |K_{\hat{a}_{\mathrm{L,out}},\hat{b}_{\mathrm{c,in}}}|^2 = \frac{4\Gamma_e\Gamma_o}{(\Gamma_m+\Gamma_e+\Gamma_o)^2}\,. \tag{2.73}$$

It shows that in order to reach close to unity efficiency, one needs to fulfill $\Gamma_e = \Gamma_o \gg \Gamma_m$.

2.4.2 Added Noise

In practice, noise is invariably present, and understanding and quantifying added noise is crucial for optimizing transduction as it directly influences the fidelity of information conversion and transfer.

The added noise level can be quantified by calculating the spectral density of a transduction experiment. The spectral density, a measure of the noise power per unit frequency, is given by

$$\begin{aligned} 2\pi\delta(\omega+\omega')S[\omega] &= \langle \mathbf{a}^\dagger_{\mathrm{out}}[\omega']\mathbf{a}^T_{\mathrm{out}}[\omega]\rangle & (2.74)\\ &= K^*[\omega']\langle \mathbf{a}^\dagger_{\mathrm{in}}[\omega']\mathbf{a}^T_{\mathrm{in}}[\omega]\rangle K^T[\omega], & (2.75)\end{aligned}$$

which can be rewritten:

$$S[\omega] = K^*[-\omega]\mathcal{N}K^T[\omega], \tag{2.76}$$

with $\mathcal{N}$ being a matrix with the occupation numbers on the diagonal. This provides the full measured noise level. If we assume $n_o \approx n_e \approx 0$, and operating close to resonance, $\omega = \Omega_m'$, we arrive at

$$\begin{aligned}\langle \hat{a}^\dagger_{\mathrm{L,out}}[\omega']\hat{a}_{\mathrm{L,out}}[\omega]\rangle &= \frac{2\pi\delta(\omega+\omega')}{\left(\frac{\Gamma_m'}{2}\right)^2}\eta_o\Gamma_o\mathcal{A}_o\left[\Gamma_o\left(\mathcal{A}_o-1\right)+\Gamma_e\left(\mathcal{A}_e-1\right)+\Gamma_m n_m\right]\\ &= 2\pi\delta(\omega+\omega')N\end{aligned} \tag{2.77}$$

And as the transduced signal reads

$$|K_{\hat{a}_{\mathrm{L,out}},\hat{b}_{\mathrm{c,in}}}|^2 = \eta_e\eta_o\frac{\Gamma_e\Gamma_o\mathcal{A}_e\mathcal{A}_o}{\left(\frac{\Gamma_m}{2}\right)^2}, \tag{2.78}$$

The added noise level of the transduced signal is

$$n_{\mathrm{add}} = \mathrm{N}/|K_{\hat{a}_{\mathrm{L,out}},\hat{b}_{\mathrm{c,in}}}|^2 = \frac{1}{\eta_e\mathcal{A}_e}\left(\frac{\Gamma_o}{\Gamma_e}\left(\mathcal{A}_o-1\right)+\left(\mathcal{A}_e-1\right)+\frac{\Gamma_m n_m}{\Gamma_e}\right). \tag{2.79}$$

For the direction $\hat{a}_{\mathrm{L,in}}, \hat{b}_{\mathrm{c,out}}$, we reach the same results with the indices e and o being inverted. In order to measure low added noise levels, one, therefore, needs to reach high detection efficiencies η, and the coupling rates need to be larger than the mechanical bath, i.e., $\Gamma_{o/e} > \Gamma_m n_m$.

2.4.3 Bandwidth

The bandwidth of conversion is a valuable performance metric that may hold practical significance, particularly in scenarios where the transducer is expected to be the bottleneck [Lauk *et al.*, 2020]. A broad bandwidth is crucial for time and frequency multiplexing, which can enhance the rate of operations. However, the significance of bandwidth also enters as high-bandwidth photons with respect to potential transducer cavity linewidths will see a low coupling efficiency. Furthermore, the conversion bandwidth has boundaries set by the microwave qubits' GHz resonance frequencies.

The conversion bandwidth of an electro-optomechanical transducer is given by total mechanical damping rate $\Gamma_e + \Gamma_o + \gamma_m$ [Andrews *et al.*, 2014]. This provides another reason why achieving high electromechanical and optomechanical coupling rates is desirable.

3 Low Effective Mass Soft-Clamped Membranes at milliKelvin Temperatures

This chapter describes optical absorption measurements performed with a low effective mass design of soft-clamped membranes, referred to as 'Dandelion' design [Saarinen *et al.*, 2023] and shown in Fig. 3.1. An initial measurement setup has been built by David Mason and Massimiliano Rossi and produced results published in Page *et al.*, 2021 with another membrane design. I further improved the setup and characterized the Dandelion membrane design. I observed that such a design suffers from higher optical absorption heating than the designs in Page *et al.*, 2021. These experimental results agree with qualitative simulation results and shifted the research focus towards a different membrane design. Regardless, here I present a new measurement setup that will allow us to characterize membranes at milliKelvin temperatures with less optical absorption heating based on stroboscopic measurements.

3.1 Motivation and Design

In order to achieve quantum cooperativities $C_{\mathrm{qu}} > 1$, which is desirable for ground-state cooling, but moreover also low-noise quantum transduction, one needs to achieve high optomechanical coupling rates Γ_{o} ($\gg \Gamma_{\mathrm{m}}$). This can be done by increasing the coupling strength g_0, which scales quadratically with Γ_{o} and is described by

$$g_0^{\max} \approx 2\frac{\omega_c}{L} r x_{\mathrm{zpf}} \xi \ , \tag{3.1}$$

where ω_c is the cavity resonance frequency, L the cavity length, r the resonator reflectivity, x_{zpf} the zero-point fluctuation described in Eq. 2.4, and ξ the overlap of optical and mechanical mode shapes [Saarinen *et al.*, 2023].

Concerning the membrane design, it is therefore desirable to either operate a low-frequency resonator or a device with low effective mass. Fig. 3.1 presents the 'Dandelion' design, which - with a modified version - has been showing high coupling rates of $g_0/2\pi = 2.3$ kHz in a fiber cavity assembly [Saarinen *et al.*, 2023], much larger compared to other membrane-in-the-middle assemblies achieving $g_0/2\pi = (127 \pm 2)$ Hz [Rossi *et al.*, 2018]. We use this design and measure mechanical ringdowns at various temperatures and optical powers to infer heating effects of a Dandelion membrane at 20 nm thickness and 18 μm defect size leading to an effective mass of $m_{\text{eff}} \approx 100$ pg, and 19×21 unit cells with a fundamental mechanical mode of approx. 1.5 MHz.

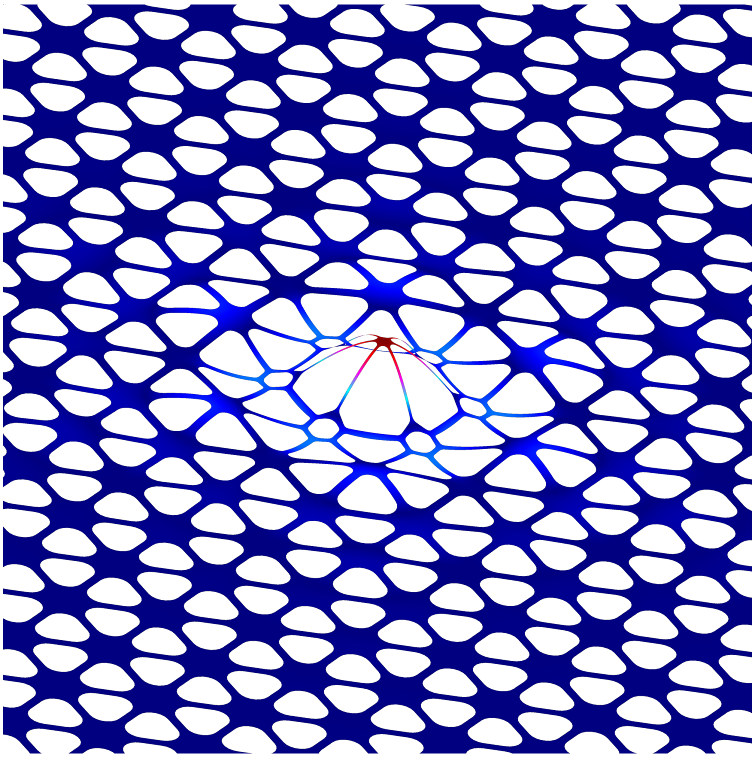

Figure 3.1: Simulated amplitude profile for the Dandelion membrane used in this experiment. Here, red represents a high amplitude in displacement. The low size and thus mass of the displaced mechanical defect in the phononic structure causes a higher coupling strength g_0 compared to other designs, e.g., in Rossi *et al.*, 2018. The unit cell size is 175 μm, the inner defect diameter is 18 μm, the tether width 3 μm, and the thickness 20 nm.

3.2 Setup

We use a heterodyne interferometer measurement for the characterization that has previously been used and set up by Massimiliano Rossi and David Mason [Rossi, 2020, Appendix C] and is shown in Fig. 3.2 and 3.3. The membrane is clamped on top of a ring piezo of type HPCh 150/10-5/3 by Piezomechanik. Despite the piezo resonance frequency being well below 1.5 MHz, corresponding to the resonance frequency of the resonators under study, the amplitude is still sufficient to actuate the membrane. The piezo rests in an oxygen-free high-conductivity (OFHC) copper holder mounted onto a dilution refrigerator's mixing chamber plate. Above the membrane, another OFHC copper holder holds a gradient-index (GRIN) lens of type 2908 glued inside a glass cylinder with a 1.5 mm distance to a pig-tailed fiber of type SMPF0208-APC, both by Thorlabs. This leads to a tight focus of the beam down to 4 μm at the position of the membrane. Fig. 3.3 shows the optical setup used

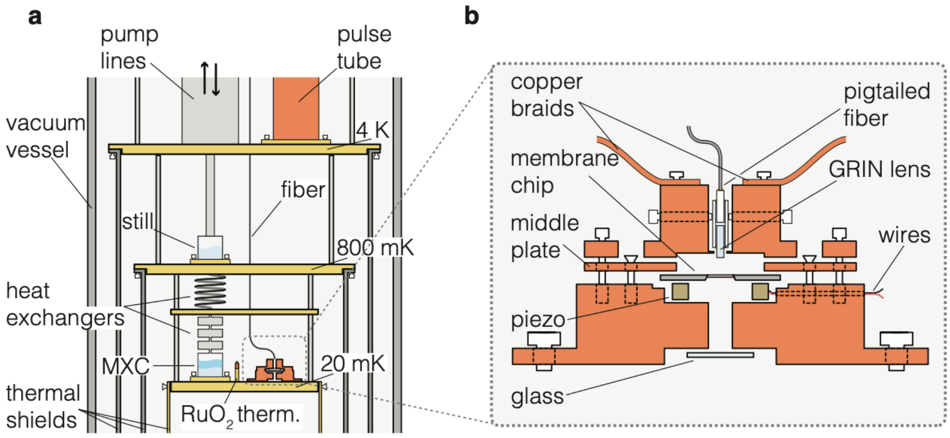

Figure 3.2: Illustration of the mechanical setup, reproduced from Rossi, 2020, Appendix C. The membrane is clamped atop a ring piezo (HPCh 150/10-5/3) resting on an OFHC copper holder attached to a dilution refrigerator's mixing chamber plate. Directly above the membrane, a GRIN lens (type 2908) is secured within a glass cylinder situated 1.5mm from a pig-tailed fiber (type SMPF0208-APC). The resulting system configuration enables a beam focus down to 4 μm at the membrane location.

in the characterization measurement. The initial laser beam is split into two interferometer arms, after which the local oscillator is frequency-shifted using an acousto-optic modulator. The other interferometer arm passes through an attenuator wheel and a shutter, both controlled by an Arduino. The laser beam enters a fiber leading into the dilution refrigerator and onto the mechanical device. The optical power sent into the refrigerator has been calibrated for the accumulated loss of fiber connections. The back-reflected beam is then overlapped with the local oscillator. The heterodyne signal, originated by the interference between the local oscillator and the back-reflection from the SiN membrane, is demodulated and sent into a lock-in amplifier of type HF2LI by Zurich Instruments.

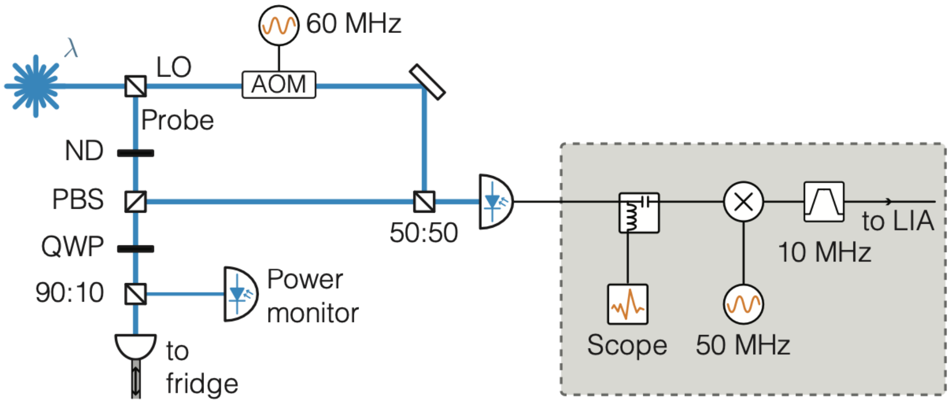

Figure 3.3: Schematic of the optical setup employed in the characterization measurement, reproduced from Rossi, 2020, Appendix C. The initial laser beam is divided into two interferometer arms, with one arm's local oscillator frequency-shifted via an acousto-optic modulator. The other arm passes through an attenuator wheel and a shutter, both motor-controlled by an Arduino. The laser beam then enters a fiber directed towards the mechanical device in the dilution refrigerator, with optical power calibrated to account for the accumulated loss in fiber connections. The back-reflected beam is overlapped with the local oscillator, with the resultant heterodyne signal demodulated and transmitted to an HF2LI lock-in amplifier by Zurich Instruments.

3.3 Results

We excite the mechanical motion by driving the piezo close to the mechanical frequency $\omega_\mathrm{m}/2\pi \approx 1.494$ MHz. After turning off the piezo drive, we can observe a re-thermalization of the mechanical resonator with the thermal bath in the form of a ringdown in the interferometric signal. The Dandelion membrane used in this measurement is 20 nm thick, possesses a mechanical defect of 18 μm inner diameter, and a tether width of 3 μm, leading to an effective mass of approx. 100 pg, and has the size of 19x21 unit cells. Fig. 3.4 shows one mechanical ringdown at 40 mK temperature of the mixing chamber plate, approx. 5 μW optical input power at 800 nm wavelength and a 20 Hz measurement bandwidth. The bandwidth has to be chosen to be 20 Hz, which is much larger than potential Duffing frequency shifts [Catalini *et al.*, 2021]. By fitting an exponential decay function to the amplitude in the form of

$$A(t) = A_0 e^{-\Gamma_m t}\,, \tag{3.2}$$

we can retrieve the mechanical quality factor given by $Q = \omega_{\mathrm{m}}/\Gamma_{\mathrm{m}}$.

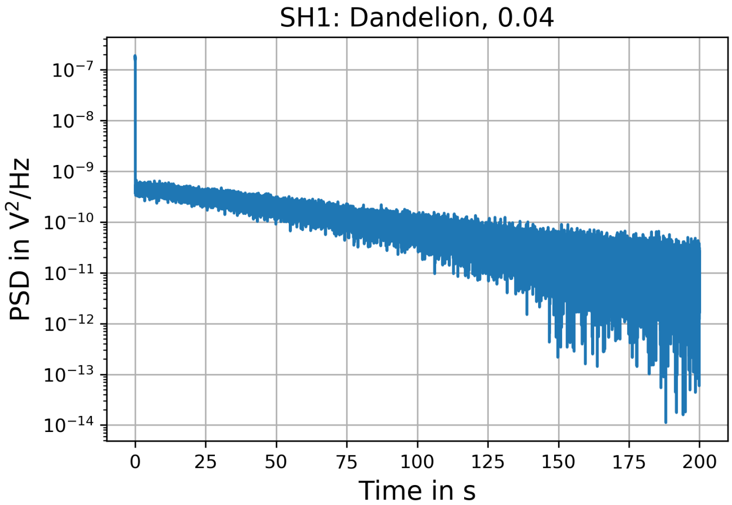

Figure 3.4: Mechanical ringdown measurement at 40 mK temperature of the mixing chamber plate, approx. 5 μW optical input power at 800 nm wavelength

We can perform these ringdown measurements at different probe beam powers and different temperatures. By assuming that a reduction of the quality factor at higher probe powers (at the same dilution refrigerator temperature) is solely due to optical absorption heating around the mechanical defect, we read out the heating effect from these measurements.

We perform ringdown measurements at various set temperatures of the mixing chamber plates with a probe beam power of 0.7 μW. The results are shown in Fig. 3.5(left). Also here, one expects a higher decay at higher path temperatures or due to a change in stress, which has also been phenomenologically reported in Zwickl *et al.*, 2008; Yuan *et al.*, 2015. Here, we do not observe a further increase of the mechanical quality factor Q below 100 mK.

In addition, we perform ringdown measurements at a fixed mixing chamber plate temperature of 40 mK and vary the optical input power. In such a measurement, optical absorption heating increases the mechanical decay rate Γ_{m}. Fig. 3.5(right). While few ringdown measurements have been taken, they indicate that optical absorption heating already induces an effect at 0.2 μW.

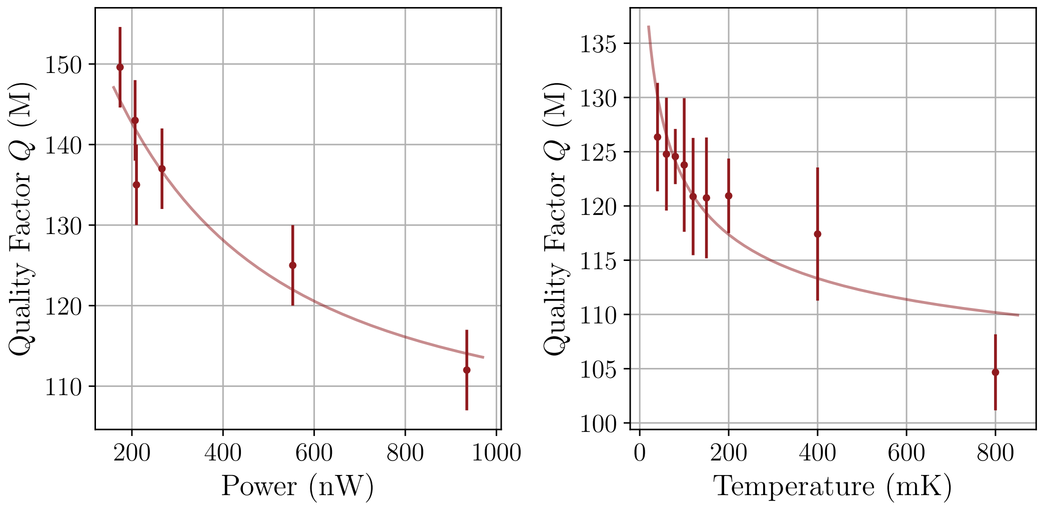

Figure 3.5: (left) Quality factors in millions, derived from ringdown measurements at various optical input powers and at a fixed mixing chamber plate temperature of 40 mK. Measurements have only been taken once, and while the uncertainty of the fit is small, the uncertainty has been given an upper estimate of $\pm 5 \times 10^6$. (right) Quality factors in millions, derived from ringdown measurements at various set temperatures of the mixing chamber plates with a probe beam power of 0.7 μW. We perform nine ringdown measurements at each temperature. Value and uncertainty come from the mean and standard deviation of the nine measurements.

"We fit the data to the following phenomenological model

$$Q(x) = \frac{1}{k_0 + kx^a} + Q_0 \, , \tag{3.3}$$

with k_0, k, a, and Q_0 free parameters" (Rossi, 2020) as shown in Fig. 3.5. This is motivated as we observe a saturation in $Q(T)$ and $Q(P)$ for high and for low optical power [Page *et al.*, 2021]. We can now combine the fit functions $Q(P)$ and $Q(T)$ to derive

$$T(P) = \left(\frac{k_P}{k_T}\right)^{1/a_T} P^{a_P/a_T} \, . \tag{3.4}$$

For the fit, we set $Q_0 = 102 \times 10^6$ and $k_0 = 1/68$ (i.e., a low-power saturaturation of the quality factor at 170M) for both curves. However, as we can see Q_0 and k_0 cancel in Eq. 3.4 as long as kept identical for both curves. From this function that is shown in Fig. 3.6, we calculate $T \propto P^{2.29 \pm 0.69}$. The low number of measurements and the low range of optical powers leads to a large confidence interval. However, in future cooldowns, we lost the coupling to the membrane, which led to changes in the measurement design described in Sec. 3.5.

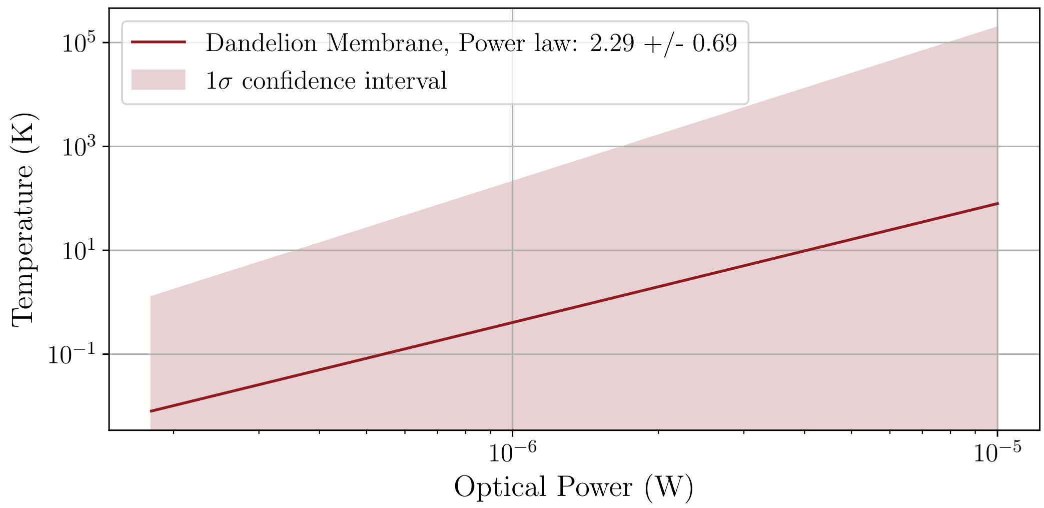

Figure 3.6: Inferred function of mode temperature as a function of optical input power based on the fits in Fig. 3.5 and Eq. 3.4. Note that measurements have only been performed up to optical powers of 935 nW and temperatures of 800 mK. The shaded area represents the 1σ confidence interval, being large due to the low number of data points.

3.4 Comparison to other Designs

For the scope of this thesis, three designs of soft-clamped membrane resonators exist and are depicted in Fig. 3.7.

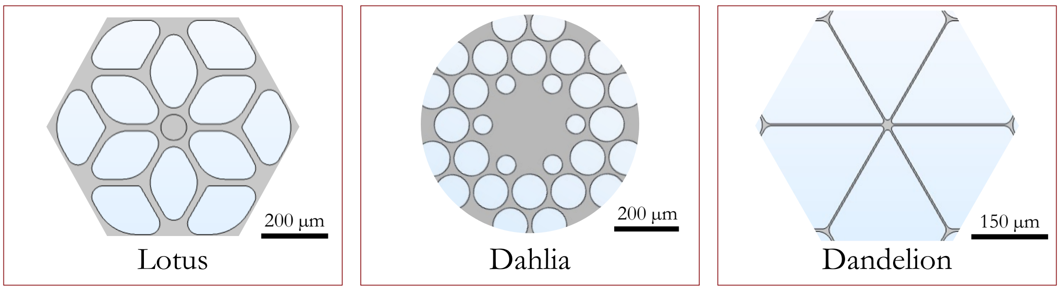

Figure 3.7: Overview of three defect designs for soft-clamped membranes: Lotus, Dahlia, Dandelion, with their naming inspired by similar structured flowers. Designs by Eric Langman.

The Dahlia design stems from the original design published in Tsaturyan *et al.*, 2017, where few defect modes have been observed within its phononic bandgap. The Dandelion design possesses a lower effective mass compared to the other two designs, which can lead to higher optomechanical coupling strength g_0 as described in Sec. 3.1 and demonstrated in Saarinen *et al.*, 2023. The Lotus design shows only a single defect mode within the phononic bandgap [Seis *et al.*, 2022].

For the Dahlia design, optical absorption measurements as in this chapter have been performed previously as in Fig. S2 in Page *et al.*, 2021 and are reprinted here as Fig. 3.8. Here, the temperature has been scaling with optical power as $T \propto P^{0.36}$. Comparing this with the measurement of the Dandelion membrane of this chapter, drawn together in Fig. 3.9, we observe lower absorption heating compared to the Dandelion design, despite the large uncertainty of the fit to the Dandelion data. We suspect that the narrow tether width of Dandelion membranes of 3 μm reduces heat transfer towards the silicon frame, localizing the heat more significantly compared to the Dahlia and Lotus design. Fig. 3.10 shows a COMSOL heat transfer simulation with a Lotus design membrane at various tether thicknesses and optical powers. Here, the optical absorption is modulated via a Gaussian heat source with an assumed absorption coefficient of 1 ppm, which is still unknown. The heat conductivity is set to be $\kappa = 1.58T^{1.54}$ (mW) m^{-1} K^{-1} as it has been measured in a similar design in Leivo and Pekola, 1998. While several assumptions have been made, simulations show in Fig. 3.10 qualitatively that, indeed, the narrow tether width of the Dandelion design could be limiting the heat transfer of the device and lead to higher surface temperatures. Interestingly, we find a power-law scaling of the 10 μm tether width membrane of 0.397 with optical power and for the 20 μm tether width membrane of 0.391, close to the scaling of 0.36 in Page *et al.*, 2021. We can not determine what lead to the significantely larger power-law scaling of the Dandelion membrane as in Fig. 3.6.

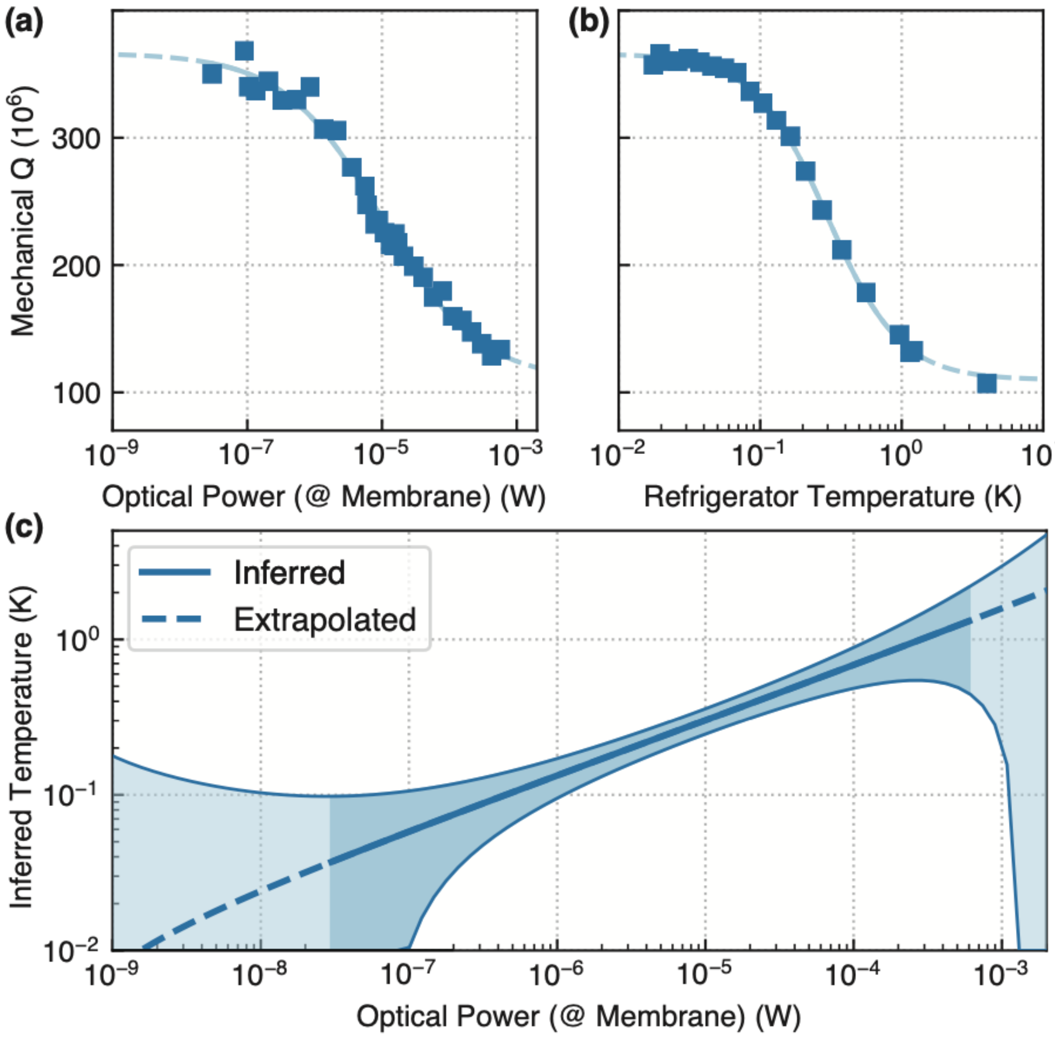

Figure 3.8: Reproduced figure of Page *et al.*, 2021 for optical absorption heating with a Dahlia membrane.

3.5 Conclusion

Low effective mass soft-clamped membranes show strong optical absorption heating imposing limitations on the reachable quantum cooperativity C_{qu} given by

$$C_{\mathrm{qu}} = \frac{\Gamma_{\mathrm{opt}}}{\bar{n}_{\mathrm{th}}\Gamma_{\mathrm{m}}}\,, \tag{3.5}$$

as in Eq. 2.40, where Γ_{opt} is the optomechanical decay rate, and $\bar{n}_{\mathrm{th}}\Gamma_{\mathrm{m}}$ the thermal decay rate. While Γ_{opt} scales linearly with optical power P as in Eq. 2.38, we inferred of these measurements an optical power scaling of the Dandelion membrane of $\bar{n}_{\mathrm{th}} \propto P^{2.29\pm0.69}$. Thus, this measurement indicates

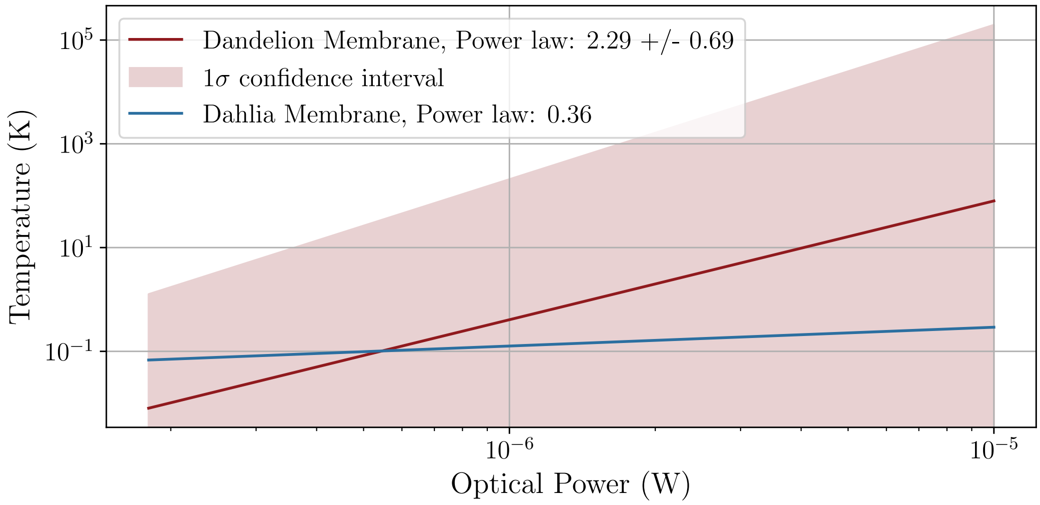

Figure 3.9: Inferred function of mode temperature as a function of optical input power based on the fits to $Q(P)$ and $Q(T)$. The Dandelion design shows a larger power-law scaling compared to the Dahlia design of Page *et al.*, 2021.

that $C_{\mathrm{qu}} > 1$ might not be achievable. However, quantum cooperativities close to unity have been achieved with the Dandelion with a larger defect size of $30\,\mu$m [Saarinen *et al.*, 2023].

The experimental setup of testing absorption heating showed even further, but is not quantified, that it has been challenging assembling a sample holder with a sufficient mode overlap between the optical field and the amplitude of the resonator. In several assemblies, the mechanical resonance could not be measured due to a displacement either when mounting the assembly in the refrigerator or during cool-down. I designed a new sample holder shown in Fig. 3.11. It allows tightly clamping the fiber holder to the piezo holder/bulk part without putting pressure on the membrane. In the past, the fiber hold was resting on the membrane clamp and was loosely clamped, as high pressure broke the silicon chip. Therefore, the new holder design should lead to lower displacements during the mounting process. However, the small defect size of the Dandelion membrane design imposes a challenge in performing more complex cryogenic cavity optomechanics experiments. While this experimental challenge can be solved through the use of actuators such as in the following papers Doeleman *et al.*, 2023, we decided for the measurements in the following chapters to utilize Lotus design membranes instead.

While the experiment was originally performed to specifically characterize the

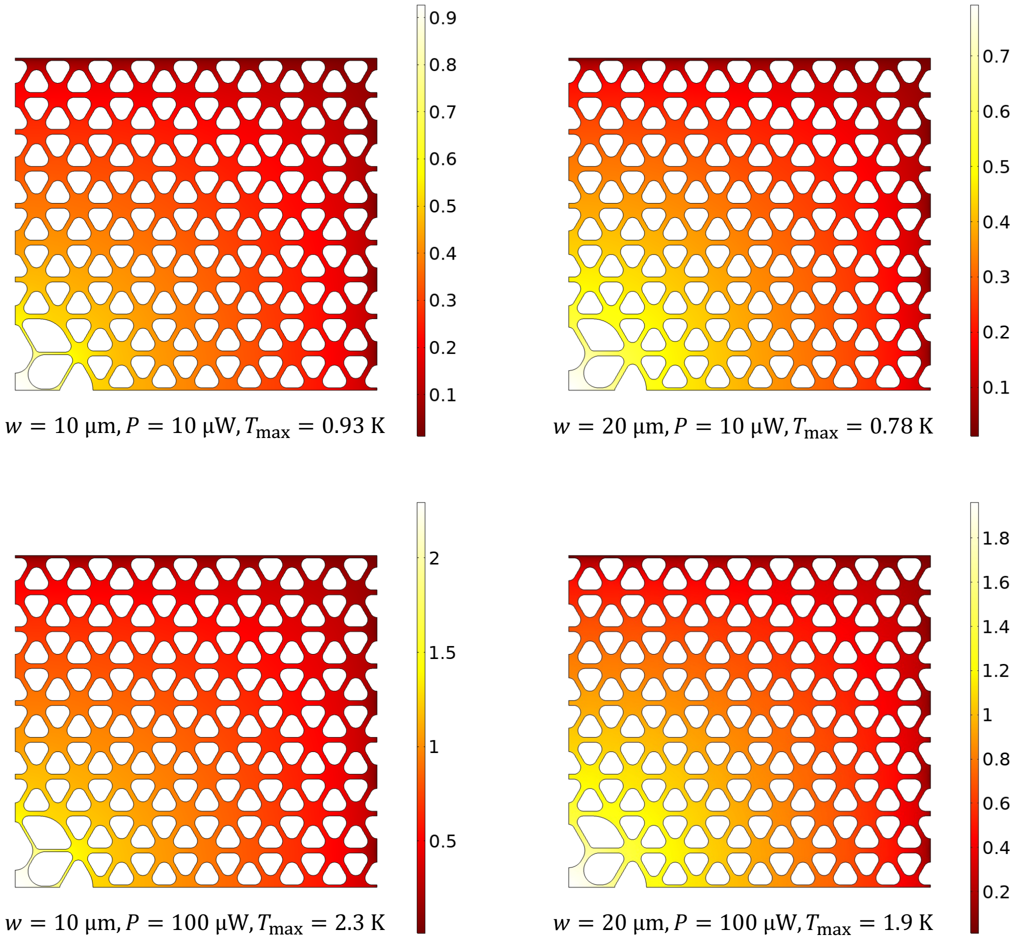

Figure 3.10: Simulation of heat transfer in soft-clamped membranes at the example of a Lotus design membrane, where the color map describes the surface temperature in Kelvin. The optical power is simulated as a heat source with Gaussian envelop function. The membrane frame is set to be at a base temperature of 12 mK. Tether width w and optical power P are varied and the temperature is determined by the maximum surface temperature. While the exact mode temperature would depend on the folding of the heat map and displacement function, under the assumption of identical mode structure in all four simulations, we can compare solely the maximum surface temperature. We find higher temperatures for the more narrow tether width w.

optical absorption effect of soft-clamped membranes, the setup can be repurposed to perform other forms of characterizations. For example, assemblies can be made to study the scaling of the quality factor with the number of unit cells of the phononic crystal material. Current simulations of mechanical quality factors inside the research group solely take into account bending losses but neglect radiation losses. Measurements could shed additional light on this. In addition, stroboscopic ringdown measurements, as they have been performed in Gisler *et al.*, 2022, would allow reducing optical absorption effects upon

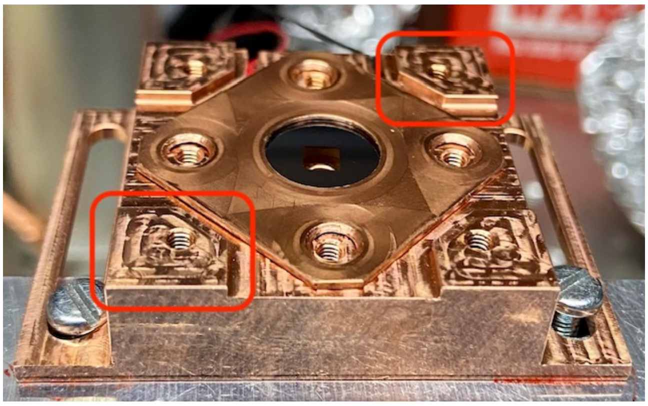

Figure 3.11: Picture of the modified sample holder. Showing the clamping ring of the membrane. The fiber holder can be tightly screwed onto the bulk part in the four corners (shown with two red squares) without applying pressure on the silicon chip.

measurement. While redesigning the membrane sample holder to accommodate many unit cell membranes, I changed the optical setup to what is shown in Fig. 3.12. Here, the acousto-optic modulator has been implemented in the probe beam. The optical power is controlled by the amplitude sent to the modulator. This allowed to remove the mechanical shutter and attenuator wheel in the previous setup, simplifying experimental control. Yannis Trouyet currently uses this setup to study the effect of radiation loss in soft-clamped membranes.

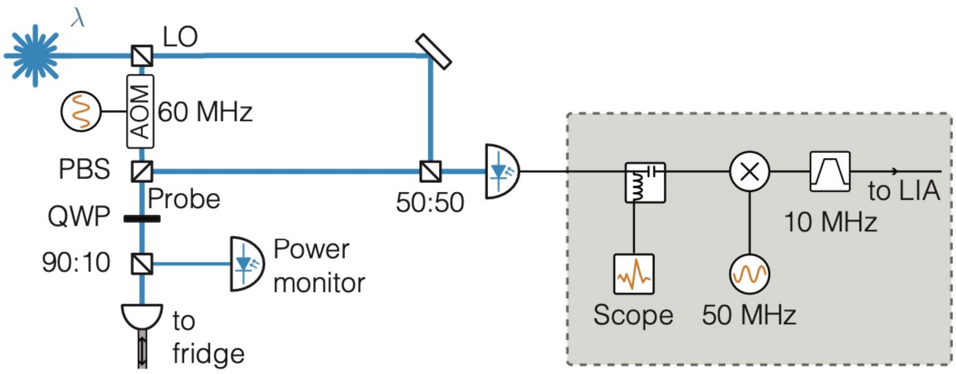

Figure 3.12: Modified optical setup from Rossi, 2020, Appendix 2020, allowing up to tens of kHz switching for stroboscopic measurements similar to Gisler *et al.*, 2022.

4

Enhanced Electromechanical Coupling to Soft-Clamped Membrane Resonators

Attaining quantum cooperativity, $C_{\text{qu}} > 1$, is a desired feature in electromechanical systems for low-noise transduction and quantum memory applications. This chapter summarizes our achievements in coupling a microwave resonator to soft-clamped membranes, where we reached the regime $C_{\text{qu}} > 1$, demonstrated ground-state cooling and showed separate measurements of the temperature and the intrinsic quality factor, indicating a coherence times of $\tau_{\text{coh}} = (n_{\text{th}}\Gamma_{\text{m}})^{-1} \sim 140$ ms. These advancements led to the publication Seis *et al.*, 2022. However, in these experiments, the inductive coupling efficiency η from an antenna to the microwave resonator showed variability for each assembly. Moreover, the electromechanical coupling strength g_0 constrained the achievable electromechanical coupling rate. Moving towards developing integrated systems for quantum transducer applications, we demonstrate how we achieved on-chip coupling between the incoupling antenna and the microwave cavity, and a motor mechanism for tuning the gap between the microwave cavity and membrane. We perform first experiments showing wide tuning of the distance between microwave cavity and membrane at cryogenic temperatures, indicating an improvement in coupling strength g_0 by a factor of 7 compared to the results published in Seis *et al.*, 2022. While I focused on characterization measurements, Thibault Capelle spearheaded the main electromechanical design considerations.

4.1 Ground State Cooling of an Ultracoherent Electromechanical System

In our published article Seis *et al.*, 2022, we showcased our electromechanical system attaining high cooperativities $C_{\mathrm{qu}} > 1$. For this achievement, we utilized a Lotus design membrane with an aluminum deposition illustrated in Fig. 4.1. We brought this membrane in proximity to a microwave cavity, formed as a loop-gap resonator (LGR) with a 10 μm separation between its two parallel capacitors as depicted in Fig. 4.4(a). The LGR's Si chip has pillars with a 300 nm height spaced several millimeters apart that determine the gap between the LGR chip and the frame of the membrane chip, sketched in Fig. 4.2. After gluing the chips together with epoxy, the aluminum metallization of the membrane becomes a part of the capacitance of the LGR (see Fig. 4.1(c)), inducing an electromechanical interaction as discussed in Sec. 2.3. However, the distance between the chips varies in each assembly due to the intrinsic curvature of the Si chips. We couple the LGR to a hand-wound antenna as seen in Fig. 4.1(c) (in black) and Fig. 4.4(b). The assembly is placed inside a gold-coated copper box for electromagnetic shielding, as depicted in Fig. 4.4(d), and mounted on a mass-spring mechanical damper with an approx. 0.5 Hz Eigenfrequency. It is then suspended from the mixing chamber plate, as shown in Fig. 4.5(b), cooled in a dilution refrigerator, and measured in back-reflection (Fig. 4.5(a)).

The thermal noise spectrum of the membrane is measured in a homodyne detection scheme and represented in Fig. 4.6(a). We begin our sequence by first moving the membrane from a large thermal state centered at zero to a displaced cooled thermal state far from zero, achieved by applying a resonant pulse composed of one pump at $\omega = \omega_c - \omega_m$ and another at $\omega = \omega_c$. Next, initial ringdown measurements are performed by amplifying the displaced state using a blue-detuned pulse. We measure exceptionally high-quality factors of $Q \approx 1.5 \times 10^9$ at a base temperature of 30 mK and a red-detuned power that ensures the classical cooperativity is well below 1. These measurements are performed while varying the power of the red-detuned tone, a process we refer to as power series, which allows us to calibrate the cooperativity. Furthermore, we take IQ traces presented in Fig. 4.3. In such IQ traces, the signal is demodulated, and both amplitude and phase quadrature are recorded. The spectrum here shows no additional dephasing. The initialization by the resonant pulse is vital, for without it, amplifying from a thermal state centered in zero would result in low signal-to-noise ratio and possible entry into the nonlinear regime. This resonant pulse efficacy is demonstrated in the subsequent ringdown series.

Subsequently, we performed two calibration measurements to calibrate

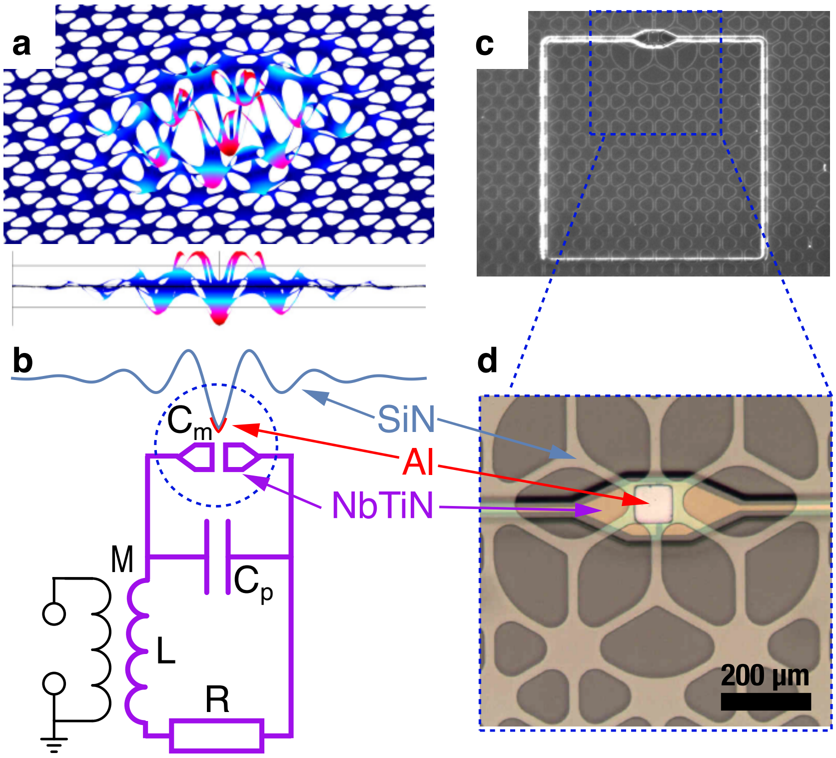

Figure 4.1: "(a) Bird's (top) and side (bottom) view of the simulated displacement of the mechanical mode localized at the defect in the phononic crystal patterned into a silicon nitride (SiN) membrane. False-color indicates displacement amplitude from small (blue) to large (red). (b) The membrane defect is metallized with a pad of aluminum (Al) and brought into proximity of two electrode pads on a different chip, thereby forming a mechanically compliant capacitance C_m. This capacitor is part of a microwave 'loop-gap' resonator made from the superconductor NbTiN, together with a parallel parasitic capacitance C_p, inductivity L and resistance R. Microwave power is coupled into this circuit through the mutual inductance M. (c) Gray-scale optical micrograph (top view) of the flip-chip, in which the microwave loop-gap resonator (bright square) shines through the largely transparent patterned membrane. (d) Color zoom onto the mechanically compliant capacitor, showing the square Al metallization on the patterned membrane above the NbTiN capacitor pads." [Seis *et al.*, 2022]

the thermal bath temperature and the dynamical backaction effect shown

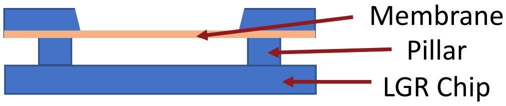

Figure 4.2: Schematic of the chip assembly. The loop-gap resonator (LGR) chip includes 300 nm tall pillars on which the membrane chip rests and is glued together with two drops of epoxy after alignment of the capacitor plates under the microscope.

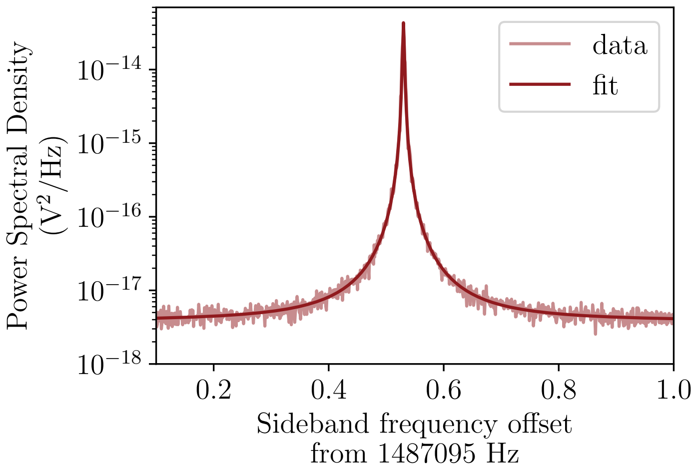

Figure 4.3: Absolute value of the Fourier transform of a 1000 second IQ trace taken with another assembly similar to the one $\Gamma_\mathrm{m} = 1.0$ mHz has been measured. The trace shows no indication of any additional dephasing as we see no spectral broadening in this Lorentzian.

in Fig. 4.7 for an accurate measurement of the thermal bath occupation n_th and the intrinsic mechanical decay rate Γ_m. We varied the dilution refrigerator temperature and measured the area of the mechanical peak as seen in Fig. 4.7(a), corresponding to the phonon occupation number that is dependent on the thermal bath coupling and the dynamical backaction effect of the electromechanical coupling. Notably, dynamical backaction becomes a significant effect at temperatures < 200 mK as the mechanical decay rate Γ_m is temperature dependent and we are keeping the pump power fixed, which led to excluding the blue measurement points from the calibration fit. This fit gives the proportionality constant between temperature and mode area in our data, inferring that the membrane thermalizes at 80 mK when the set dilution refrigerator temperature is 30 mK. Moreover, we calibrated the dynamical backaction effect to find Γ_m. We varied the red-detuned read-out power during the ringdown measurement in 4.7(b), which resulted in the curve in 4.7(c). This indicates that the intrinsic mechanical damping rate is

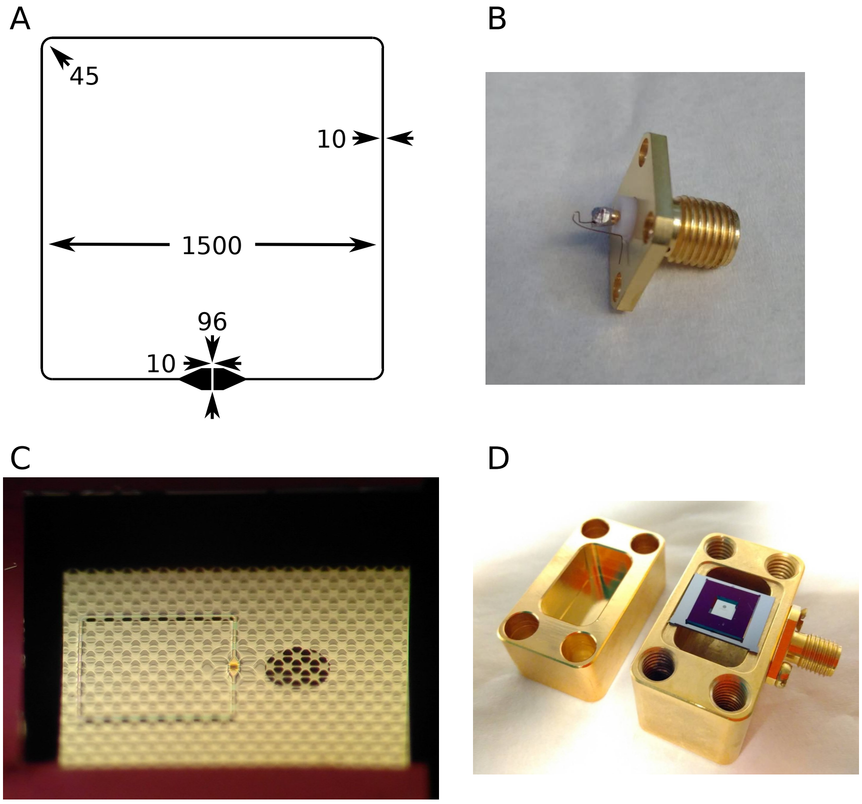

Figure 4.4: "(a) Loop-gap resonator mask with dimension in microns. (b) SMA connector for inductive in-coupling to the microwave cavity: one end of the hand-wound loop is soldered to the central pin of the connector, while the other end is clamped on the sample holder for grounding. (c) Zoom-in at an angle of the assembled flipchip with the patterned membrane hovering over the loop- gap resonator. (d) The flipchip is placed in the middle of a hollow volume of a copper (gold-coated) sample holder. The inductive in-coupling loop (shown in (b)) protrudes into the hollow volume underneath the resonator to achieve the mutual inductive coupling." [Seis *et al.*, 2022]

indeed approx. 1 mHz. Furthermore, by phase-modulating the pump beam, we create a distinct calibration tone in our spectrum, a technique adapted from the Gorodetsky method [Gorodetsky *et al.*, 2010]. This method crucially combines phase modulation and amplitude demodulation, enabling us to selectively capture light that has undergone quadrature phase shift in the cavity. Incorrectly applying phase modulation and phase demodulation might yield an artifactual peak even in the absence of cavity-bound light. In our experiment, the modulation by the mechanical movement and that by the calibration tone, though originating from different sources, generate an identical proportionality constant. This allows us to calibrate the mechanical resonance in the spectrum to the input power by calculating the ratio of the area of the mechanical peak and the calibration tone, where the calibration tone's area depends only on

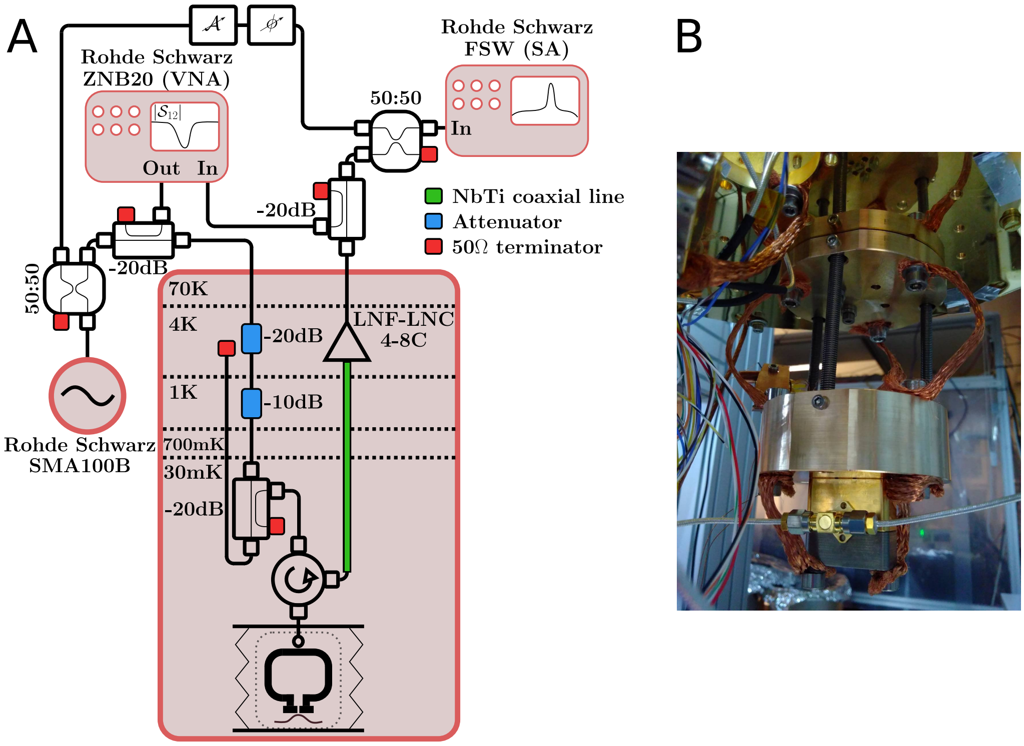

Figure 4.5: "(a) Setup of the microwave equipment around the dilution refrigerator. (b) Photograph of the single-stage mechanical damper mounted to the mixing chamber plate (top) of the dilution refrigerator to isolate from environmental vibrations, especially the pulse tube." [Seis *et al.*, 2022]

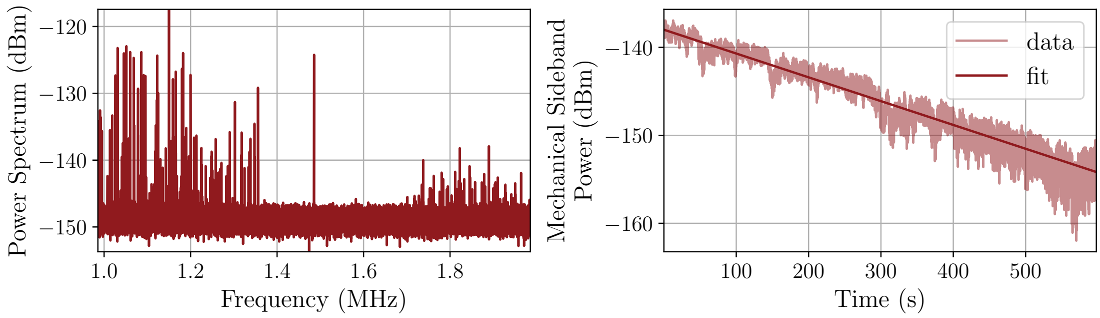

Figure 4.6: "(a) Thermal noise spectrum showing a large bandgap between 1.35 and 1.7 MHz around the mode of interest at approx. 1.5 MHz. (b) Mechanical ringdown of the defect mode of a metallized membrane at cryogenic temperature, yielding an ultrahigh quality factor of approx. 1.5 billion." [Seis *et al.*, 2022]

the input power.

Finally, we performed a cooling measurement that is shown in Fig. 4.8. We set our microwave pump beam red-detuned at $\Delta = -\Omega_\mathrm{m}$, increase the pump beam power, and measure the back-reflected spectrum. At low cooperativity we observe solely an increase in optomehcnical gain, or signal-to-noise ratio,

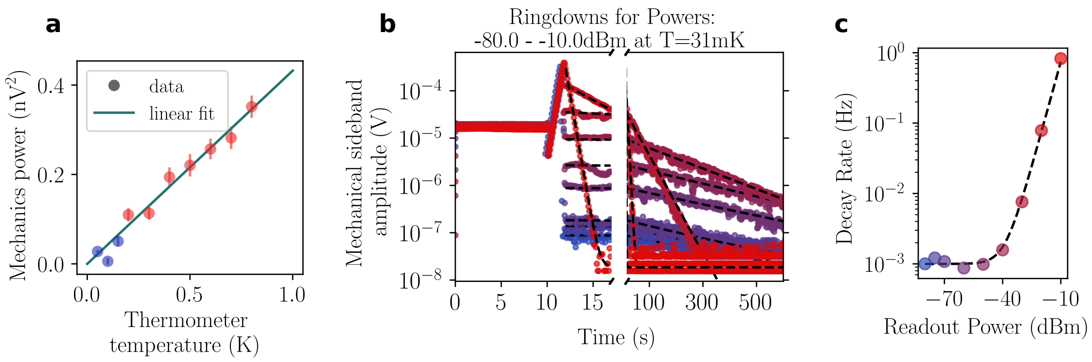

Figure 4.7: "(a) The mechanical occupation is calibrated by thermal anchoring at temperatures above 200 mK. The linear relationship between the area of the mechanical peak in the spectrum and the sample holder temperature confirms that the mechanics is thermalized. Only the red data are used for the fit (see main text). Error bars are std. dev. of the mechanical sideband area fits. (b) A mechanical energy ringdown series measured as function of the applied cooling power, measured at 30 mK. Overlayed temporal series show repeatable initialization of the mechanical energy (up to 12 s) and increasing decay rates as the cooling power is turned up. (c) The fit of mechanical decay rates gives the intrinsic decay rate Γ_m, without dynamical backaction, and the corner power P_0, where the cooling rate $\Gamma_\mathrm{e}(P_0)$ is equal to Γ_m. Points' color code is the same as in panel (b)." [Seis *et al.*, 2022]

while at higher cooperativity we observe dynamical backaction broadening, shown in Fig. 4.8(a). We observe destructive interference within the noise spectrum due to an additional power dependent noise term at very high pump powers as in Fig. 4.8(b). This we attribute to some microwave noise heating.

We use the background level of the acquired traces at different microwave source powers to calibrate our intracavity photon number. After including the additional noise effect of Fig. 4.8(b), we extracted the phonon occupations for the individual traces via a fit. The spectrum fit function considers three terms, the optical shot-noise, mechanical noise, and the cross-correlation noise. It results in a spectrum of

$$S(\omega) = n_\mathrm{add} + 4\eta\left(\tilde{n} + 1/2\right) + \eta\Gamma_\mathrm{m}\Gamma_\mathrm{e}\frac{\bar{n}_\mathrm{th} + \frac{1}{2} - \left(2 + \frac{\Gamma_\mathrm{e}}{\Gamma_\mathrm{m}}\right)\left(\tilde{n} + \frac{1}{2}\right)}{\left(\Gamma_\mathrm{m} + \Gamma_\mathrm{e}\right)^2/4 + \left(\omega - \omega_\mathrm{p} - \Omega_\mathrm{eff}\right)^2}, \quad (4.1)$$

"where we have defined $\tilde{n} = \eta n_\mathrm{c} + (1-\eta)\, n_0$, with $\eta = \kappa_\mathrm{c}/\kappa$, κ_c the coupling rate to the microwave cavity, n_c the microwave noise occupation coming from either the pump phase noise or the cavity frequency noise, n_0 the noise occupation of the microwave thermal environment (which is negligible in the considered experimental conditions). In the above expression, $\Omega_{\text{eff}}/2\pi$ is the effective mechanical frequency, including the frequency shift induced by the dynamical backaction." [Seis *et al.*, 2022] The results of those fits shown in 4.8(d) indicate that we have been able to reach the mechanical ground state with an occupation of $\bar{n}_{\text{min}} = 0.76 \pm 0.16$. To summarize, Tab. 6.1 shows the

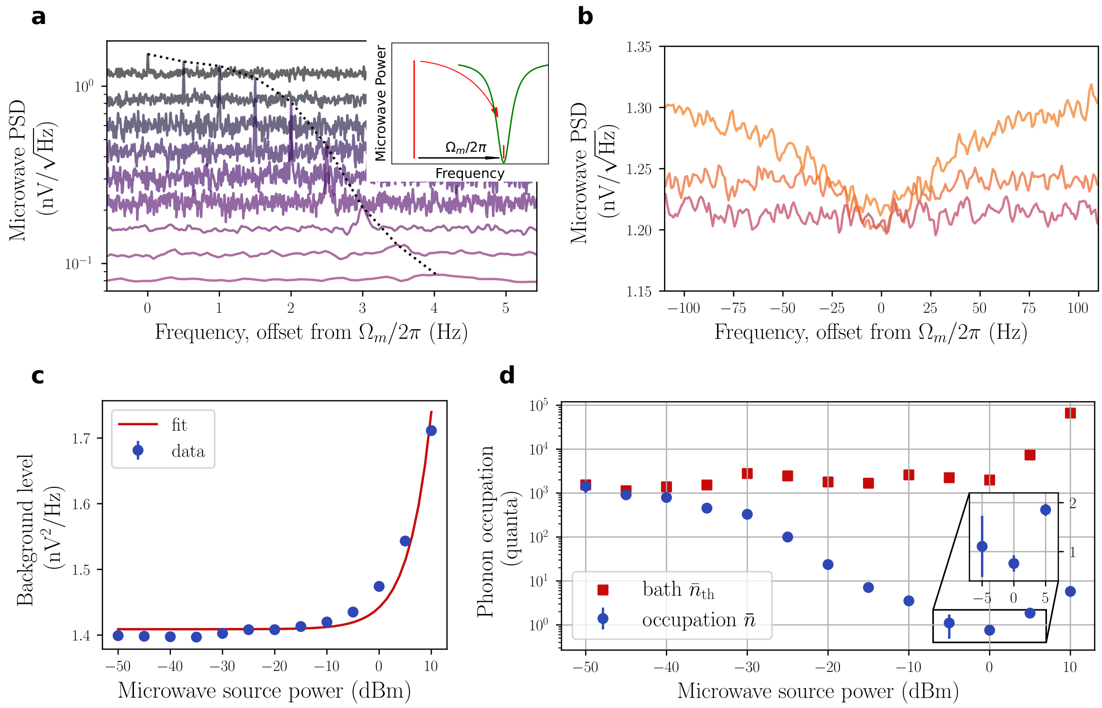

Figure 4.8: "(a) Mechanical power spectral density (PSD) around the defect mode as the cooling power is increased: the peak first increases in height with measurement gain, then visibly broadens as cooling takes place. For readability, spectra are artificially offset downward and to the right in equal steps, respectively, as the power is increased. The dotted line is a guide to the eye for the location of the mechanical peaks. The inset depicts the scattering process due to the mechanics, which creates a sideband (small vertical red line) in the microwave cavity (green dip) at an angular frequency m above the pump tone (tall vertical red line). (b) At high pump powers, the cavity is populated due to the microwave phase noise: the noise occupancy is visible in the 'squashing' of the mechanical feature. (c) The increased background level of the mechanical spectrum allows to extract the cavity occupation $\bar{n}$. d The mechanical occupation, calibrated in number of motional quanta, reaches below one phonon by dynamical backaction cooling before being heated up by cavity occupation due to input phase noise. Error bars are std. dev. of the mechanical sideband area fits." [Seis *et al.*, 2022]

parameters achieved in this experiment.

In conclusion, the electromechanical coupling rate and with that the quan-

Table 4.1: Summary of parameters of the experiment in Seis *et al.*, 2022

Parameter	Value
Microwave cavity frequency	$\omega_c/2\pi = 8.350$ GHz
Cavity total decay rate	$\kappa/2\pi = 226$ kHz
Cavity coupling efficiency	$\eta = 0.81$
Mechanical frequency	$\Omega_m/2\pi = 1.487$ MHz
Mechanical energy decay rate	$\Gamma_m/2\pi = 1.0$ mHz
Electromechanical coupling strength	$g_0 = (0.89 \pm 0.11)$ Hz
Thermal bath occupation	$n_{th} \approx 1.1 \times 10^3$
Highest electromechanical coupling rate demonstrated	$\Gamma_e \approx 80$ Hz

tum cooperativity has been limited by an additional heating effect at high pump powers $\bar{n}_{cav}$. Experimentally, it also required several assemblies to achieve a coupling efficiency of 81%. The following two sections show how we achieved, moving forward, to establish reliable cavity coupling efficiencies and how we implemented an actuator that reduced the gap distance between the microwave cavity and the membrane, indicating in first measurements an increase in coupling strength g_0 by a factor of 7, which would allow us to reach electromechanical coupling rates approx. 50 times higher than what has been presented in the paper.

4.2 Implementing Coplanar Microwave Coupling

Microwave fields are coupled in and out of the LGR via electromagnetic induction. Previously, the connection was accomplished using a manually wound antenna coupling from below the LGR chip, as per the methodology outlined in [Seis *et al.*, 2022]. We have since evolved this approach to incorporate coplanar coupling into the microwave cavity, a practice prevalent in superconducting circuits.

As illustrated in Fig. 4.9, our new methodology involves the utilization of a coplanar waveguide running close to the LGR. This is more explicitly depicted in Fig. 4.9(b). The next stage involves the wire bonding of this antenna with deposited gold to the pin of an SMA connector, as shown in Fig. 4.9(c).

For the SMA wirebond, we subsequently smoothen the SMA pin using sandpaper, and post-wire bonding. In a parallel operation, we wirebond the chip's ground to the casing of the chip, which in this case is a gold-plated copper box. This box is, in turn, interconnected with the ground of the SMA connector. Finally, we employ this coplanar coupling for the measurements in the following section.

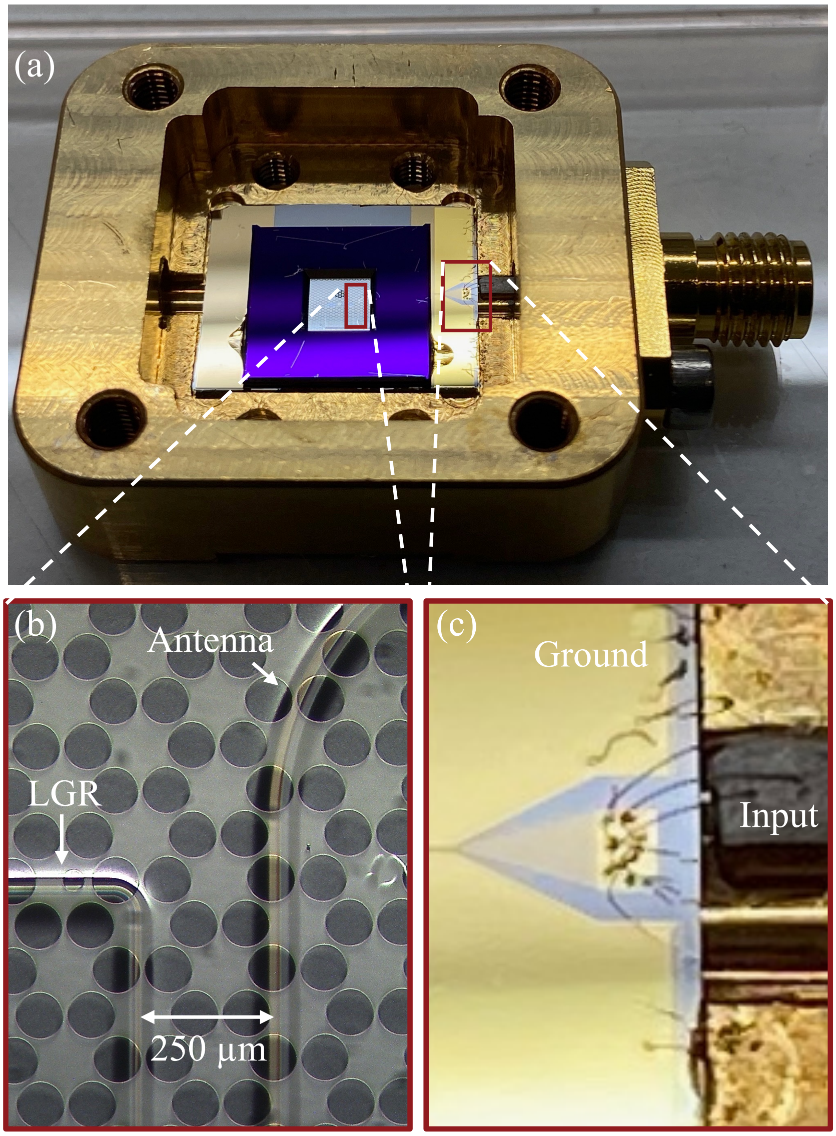

Figure 4.9: On-chip coupling to the LGR via a coplanar antenna. Note the coplanar antenna running parallel to the LGR at a designated distance (b), and its subsequent wire bonding to an SMA connector (c).

4.3 Increased Coupling Strength g_0 via Actuator-Based Capacitor Gap Tuning

Furthering our endeavor to boost the electromechanical coupling rate Γ_e, we realized that the crux lies in enhancing the electromechanical coupling strength g_0, given that $\Gamma_\mathrm{e} \propto g_0^2$ for a phase noise level at a given $\bar{n}_\mathrm{cav}$. While we already dictated the zero-point fluctuation through meticulous design choices of the mechanical resonator (m_eff and Ω_m), we focused on tuning the optical frequency shift per displacement $G = -\partial\omega_\mathrm{cav}/\partial x$. For two parallel plate capacitors, the resonance frequency can be described as

$$\omega_\mathrm{r} = \frac{1}{\sqrt{L\left(C_\mathrm{p} + \frac{\alpha'}{d}\right)}} = \frac{\omega_\mathrm{f}}{\sqrt{1+\frac{\alpha}{d}}}\,, \tag{4.2}$$

where C_p is the parasitic capacitance, $\alpha = \alpha'/C_\mathrm{p}$, and d the distance between the capacitor plates of the LGR and the aluminum metallization of the membrane. Then,

$$G = -\frac{d\omega_\mathrm{r}}{dd} = -\omega_\mathrm{f}\left(-\frac{1}{2}\right)\left(1+\frac{\alpha}{d}\right)^{-3/2}\alpha\,(-1)\left(\frac{1}{d^2}\right)^2\,. \tag{4.3}$$

With the measured resonance frequency and knowing the zero-point fluctation, we can then derive find both the distance d and the inferred coupling strength g_0.

Historically, this gap d has been defined by 300 nm tall pillars bridging the frames of both chips. However, this approach presented challenges. The inherent curvature of the chips led to a substantial variation in the gap d, resulting in a broad spectrum of observed g_0 values in different flip-chip assemblies, ranging from 26 mHz to 1.5 Hz [Seis, 2021]. In certain assemblies, the curvature even provoked a collapse between the capacitor plates, limiting the potential pillar size reduction. Moreover, situating these pillars closer to the capacitor plates would mean placing pillars directly on the membrane - a scenario that would introduce considerable clamping losses.

We invested in the cryo linear actuator 2201 from JPE to overcome these limitations. Capable of tuning with a minimal step size of 1 nm and an extensive travel range of 12 mm, this motor was attached to a cantilever, facilitating the adjustment of the LGR from below to achieve closer proximity with the membrane metallization, as depicted in Fig. 4.10. Initial tests at room temperature indicated that the travel range of the motor was more than sufficient to navigate between no contact and the point at which the distance between the capacitor plates was reduced, a transition evidenced by a color shift in the thin-film interference between the LGR and the membrane.

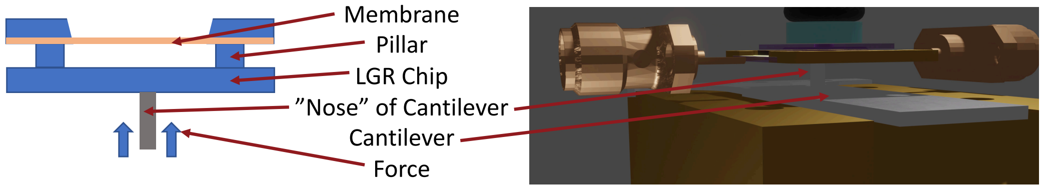

Figure 4.10: Schematic of how the cryo linear actuator reduces the gap between the LGR chip and membrane. The actuator pushes the cantilever, whose nose applies a force to the back-side of the LGR chip. This causes a bending of the chip, pushing the parallel capacitor plates of the LGR closer to the metalization of the membrane chip.

We installed an assembly with coplanar coupling as shown in Fig. 4.9 and the cantilever and motor attached inside a 4K cryostat and gauged the microwave cavity resonance frequency. Upon tuning the motor to various positions, we observe a shift in resonance frequency as shown in Fig. 4.11. Assuming this to be a consequence of the gap between the capacitor plates changing and hence modulating the total capacitance of the LGR (given the identical LGR used as in Seis *et al.*, 2022), we could extrapolate the changes in the resonance frequency to equivalent modifications in the gap distance d and the coupling strength g_0. We use the same calculation with a parasitic capacitance of $C_\mathrm{p} = 75$ fF as shown in Fig. S2 and Eq. S48 in Seis *et al.*, 2022. Assuming that in this new measurement, the g_0 and gap distance d would be identical to that in the publication at the same resonance frequency – renormalized to the specific zero-point fluctuation of the individual membrane design – , we can draw the results of 4.12.

Remarkably, we managed to augment the coupling strength by a factor of 7.6. While it would be prudent to conduct additional measurements inside a dilution refrigerator, where the inherent LGR losses are significantly diminished, allowing for more reliable g_0 measurements via dynamical backaction and Gorododetsky calibration, our current data paints an optimistic picture. It hints at the possibility of enhancing the electromechanical coupling rate by 50, a development of high relevance, particularly for low-noise quantum transduction applications.

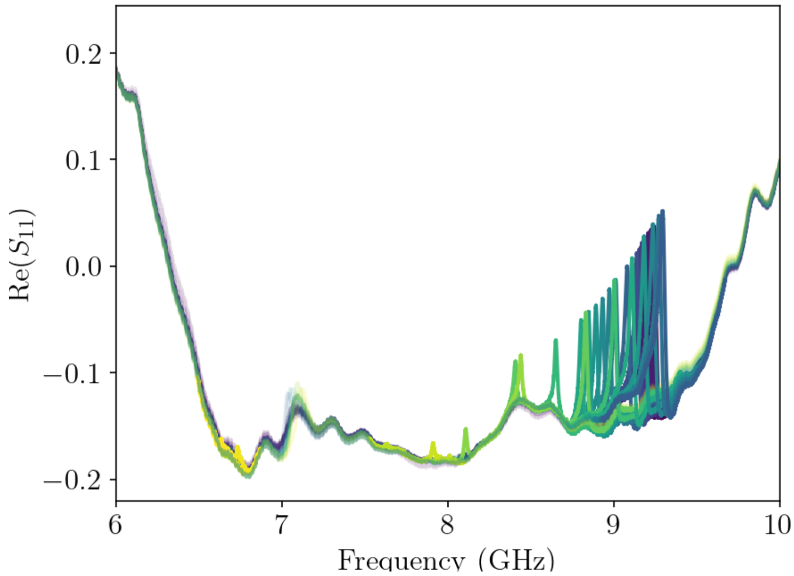

Figure 4.11: VNA transmission measurement of the device. For different motor positions (different colors), one can see a shift in peak frequency from 8 to 9.3 GHz that we attribute as LGR resonance frequency. While I assembled the system and performed initial measurements, this dataset has been recorded by Thibault Capelle.

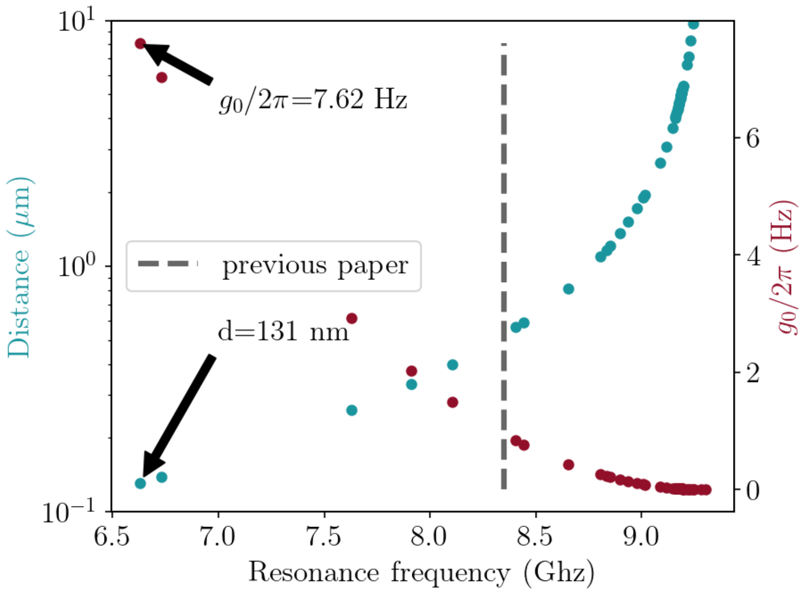

Figure 4.12: Plot showing inferred coupling strength g_0 and gap distance d of the microwave cavity resonator, achieved by adjusting the LGR chip's proximity to the membrane metallization using the cryo linear actuator. Analysis by Thibault Capelle, following the equations described here as Eq. 4.2 and Eq. 4.3.

5 High-Finesse Optomechanical Cavity Inside Dilution Refrigerators

For both quantum memory and low-noise quantum transduction, it is desirable to achieve optomechanical coupling rates Γ_{opt} much larger than the mechanical resonator's coupling to the thermal bath $n_{\mathrm{th}}\Gamma_{\mathrm{m}}$, i.e., $\Gamma_{\mathrm{opt}} \gg n_{\mathrm{th}}\Gamma_{\mathrm{m}}$. As the optomechanical coupling rate is inversely proportional to the cavity linewidth κ, it is desirable to design high-finesse/narrow-linewidth cavities and place them in low thermal bath environments. Operating high-finesse optomechanical cavities at milli-Kelvin temperatures, however, is challenging due to strong vibrations inside dilution refrigerators and due to cavity losses. This chapter describes vibrations encountered with dilution refrigerators and the design considerations that have been taken for cavity design, vibration isolation, and optical access to tackle this challenge. In addition, we study how the membrane resonator leads to additional losses in MIM assemblies and which design considerations have been taken to mitigate losses.

5.1 Vibrations of Dilution Refrigerators

Dilution refrigerators have become an essential tool for many quantum physics experiments, allowing to cool experiments down to milli-Kelvin temperatures in commercial, automated experiments. A dilution refrigerator works by circulating a mixture of two isotopes of helium: helium-3 and helium-4. As the mixture passes through a phase-separating area, the helium-3 dilutes into the helium-4, an endothermic process that cools the surrounding environment. The now-separated isotopes are recompressed and recombined at the top of the system, allowing the cycle to begin anew and achieve temperatures very close to absolute zero. Particularly common are 'dry' dilution refrigerators running without an external supply of liquid helium, which is also used in these experiments and sketched in Fig. 5.1. In such a dry dilution refrigerator, the helium-4 pre-cooling is performed by a circulation line at the '4K Plate' and is operated by a pulse tube system. The pulse tube works as a heat engine cooling the liquid helium. Its valve operates at approx. 2 Hz [Olivieri *et al.*, 2017]. In addition, the helium gas flow, when passing through the valve and hoses, creates vibrations in the kHz regime [Uhlig, 2023]. This frequency range causes measurable vibrations on optical systems inside the dilution refrigerator as shown in Fig. 5.2. In this data taken by Massimiliano Rossi, an optomechanical cavity has been mounted on a rigid platform hanging from the mixing chamber plate that will be explained later in this chapter. The cavity was slope-locked in transmission at a finesse of approx. 400, corresponding to a cavity linewidth of 14 MHz, due to the strong vibrations in the system. The lock beam and the photodiode in transmission were mounted with a Thorlabs cage system on the outer shield of the dilution refrigerator. At approx. 80 kHz, one can see the fundamental frequency of the 15x15 mm Si chip of the SiN membrane part of the optomechanical cavity. In addition, one sees imprinted sidebands at approx. $\pm$ 8 kHz. As these sidebands are significantly reduced when turning off the pulse tube, we attribute this frequency to the whistling of helium-4 through the pulse tube valve and hoses. The peak at approx. 19 kHz in both spectra can be identified as the dither tone to the etalon lock used inside the Ti:sapphire laser used in this experiment. The resolution of the measurement is not sufficient to identify the 2 Hz noise of the valve.

As vibrations of pulse tubes inside dry dilution refrigerators appear significant, it requires to mitigate this by reducing vibrations and instabilities of optical experiments. We therefore researched several design configurations, including the cavity design, material choice, and a vibration isolation platform, described in this chapter's next sections.

5.2 Cavity Parameters

We decided to build a hemispherical Fabry-Pérot cavity with two separate mirror coatings, which allows us to achieve high overcoupling >90%. Moreover, as we are using a widely tunable titanium-sapphire laser SolsTiS by Msquared

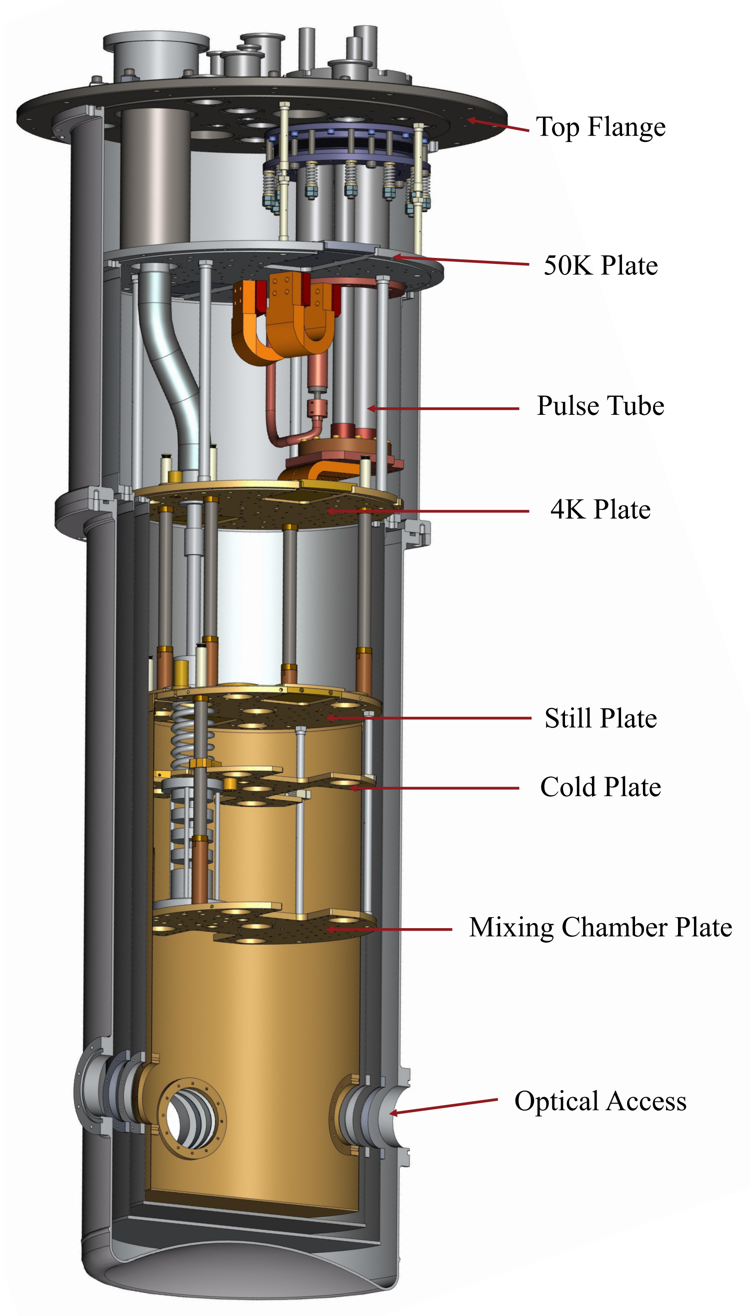

Figure 5.1: Drawing of the dry dilution refrigerator *Bluefors LD-250* used in our experiments. Helium-3 and -4 are mixed inside the mixing chamber, cooling the environment to milli-Kelvin temperatures. Pre-cooling is performed via a pulse tube mounted on the 4K plate. Optical experiments are mounted on platforms hanging from the mixing chamber plate and using the optical free-space access.

with a narrow linewidth of < 100 kHz RMS over $100\ \mu$s, we can tune the laser wavelength and with that change the finesse and coupling ratio we are operating at. Fig. 5.3(a) shows the transmission curves of the high-reflectivity mirror coatings we purchased. Furthermore, the manufacturer claims an absorption

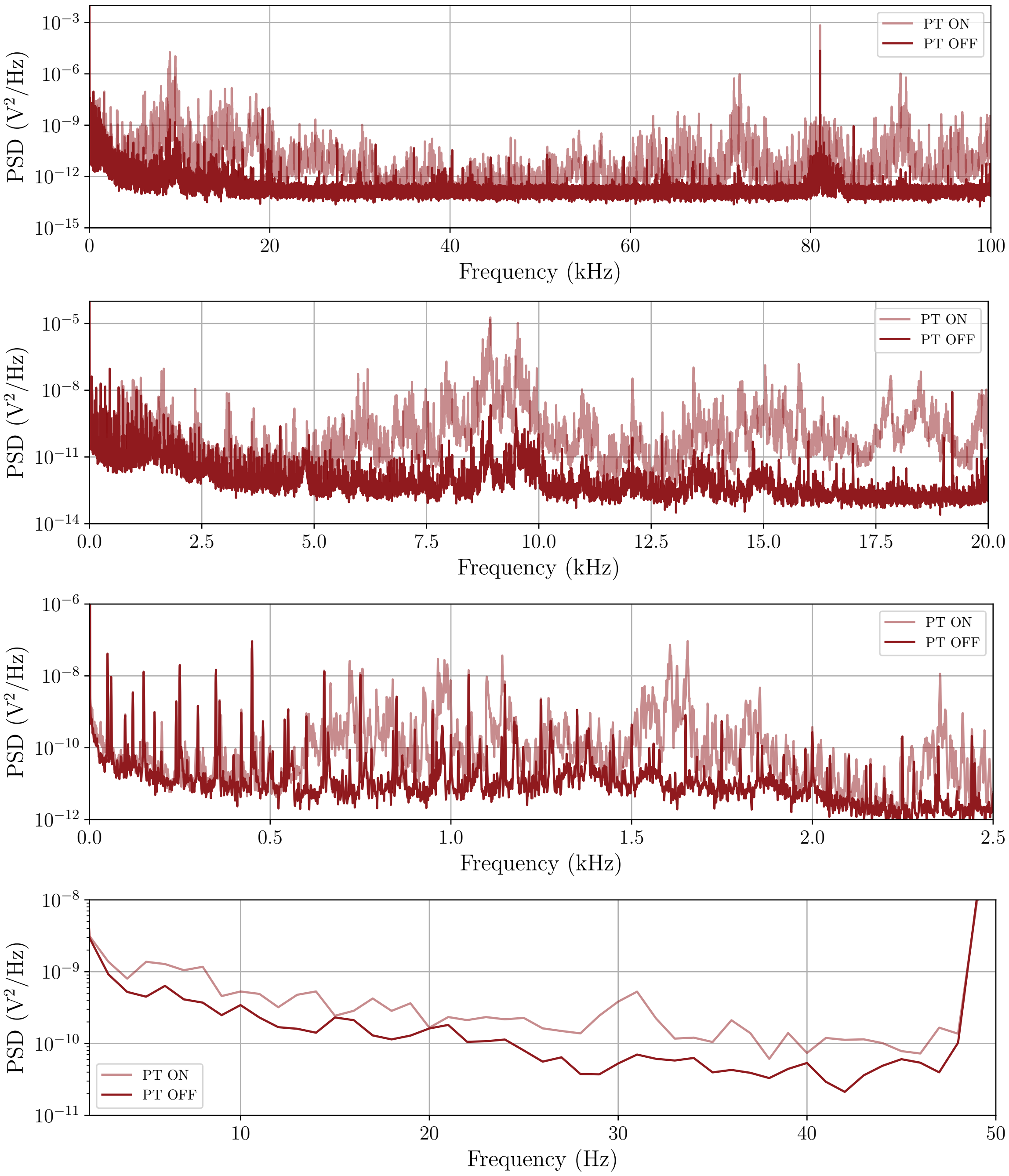

Figure 5.2: Vibrational spectra of the optomechanical system mounted in the dilution refrigerator, as measured by Massimiliano Rossi. Key resonant frequencies are observable such as the fundamental frequency of the Si chip at 80 kHz and the dither tone from the laser lock at 19 kHz. Notable sidebands at approximately ± 8 kHz are associated with the pulsation of helium-4 through the system. Lower frequency noise from the valve operation is not sufficiently resolved in this data.

loss <3 ppm. Fig. 5.3(b-d) shows the expected finesse, cavity linewidth, and coupling ratios for a 24 mm cavity based on these specifications.

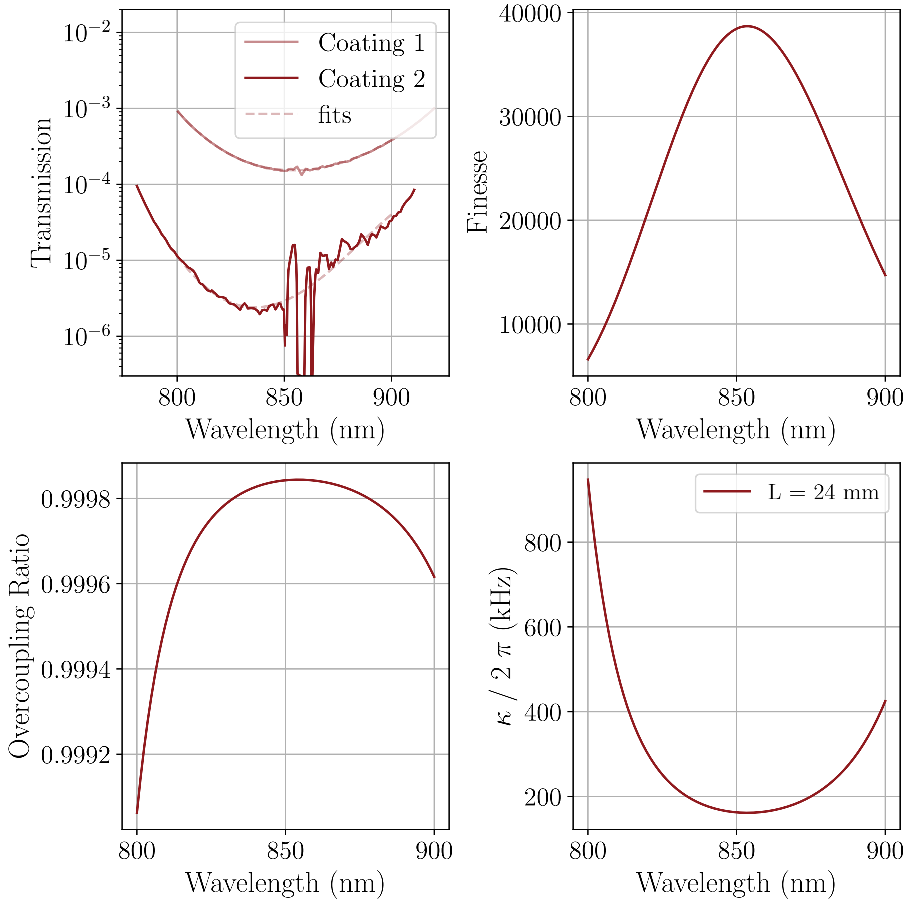

Figure 5.3: (a) Transmission curves for the high-reflectivity mirror coatings used in constructing our hemispherical Fabry-Pérot cavity. The manufacturer claims an absorption loss of less than 3 ppm. (b-d) Projected finesse, cavity linewidth, and coupling ratios for a 24 mm cavity built with these coatings. The tunable SolsTiS laser by Msquared allows us to operate at varying finesses and coupling ratios by adjusting the laser wavelength.

5.3 Vibration Isolation

We investigated two types of copper platforms that can suspend an optical system from the mixing chamber plate. One that I will refer to as rigid platform, with pillars of the dimensions 8 mm × 10 mm × 24 cm, for which I am presenting the first four simulated Eigenfrequencies in Fig. 5.4, and one, that I will refer to as soft platform, with pillars of the dimensions 5.1 cm × 0.6 mm × 24 cm, for which the first six simulated Eigenfrequencies are shown in Fig. 5.5. While the soft platform shows in the simulation lower Eigenfrequencies, it also shows displacement only in one propagation axis. In comparison, the rigid platform shows displacements in all three dimensions and potential rotation.

This difference in behavior is of relevance to us. While oscillations in the propagation axis of the cavity mode will induce an additional fluctuating phase term, it will not be measured as the measurement in direct detection that we are dealing with in this thesis will only care about the phase difference between the back-reflected electric field at the first mirror and the leak out of the cavity. However, any vibrations out of the cavity axis will influence the intracavity field and is therefore undesirable.

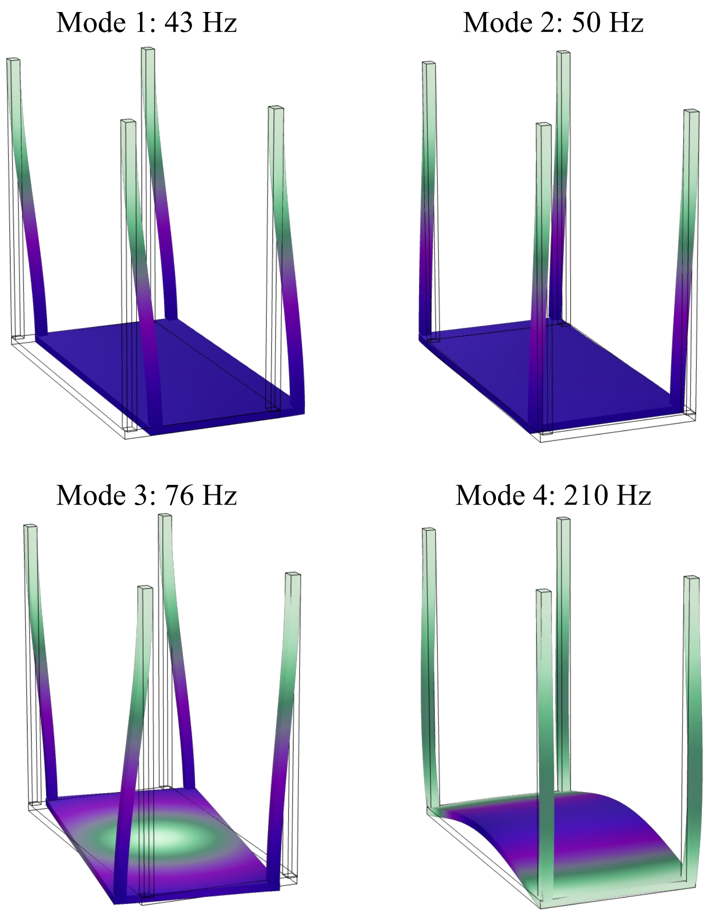

Figure 5.4: Simulated Eigenfrequencies for the first four modes of a rigid platform made of copper, featuring pillars with 8 mm x 10 mm x 24 cm dimensions. Note the three-dimensional displacement and potential rotation in the vibrations.

We test these two platforms in an experimental setup that is shown in Fig. 5.6. We mount both platforms one after another hanging from the mixing chamber plate and place a standard Thorlabs mirror on it. We send in a free-space laser beam from an optical table next to the dilution refrigerator and measure the back-reflected spectrum in a heterodyne interferometer scheme. Any broadening of the interference peak seen in the spectrum, we attribute then

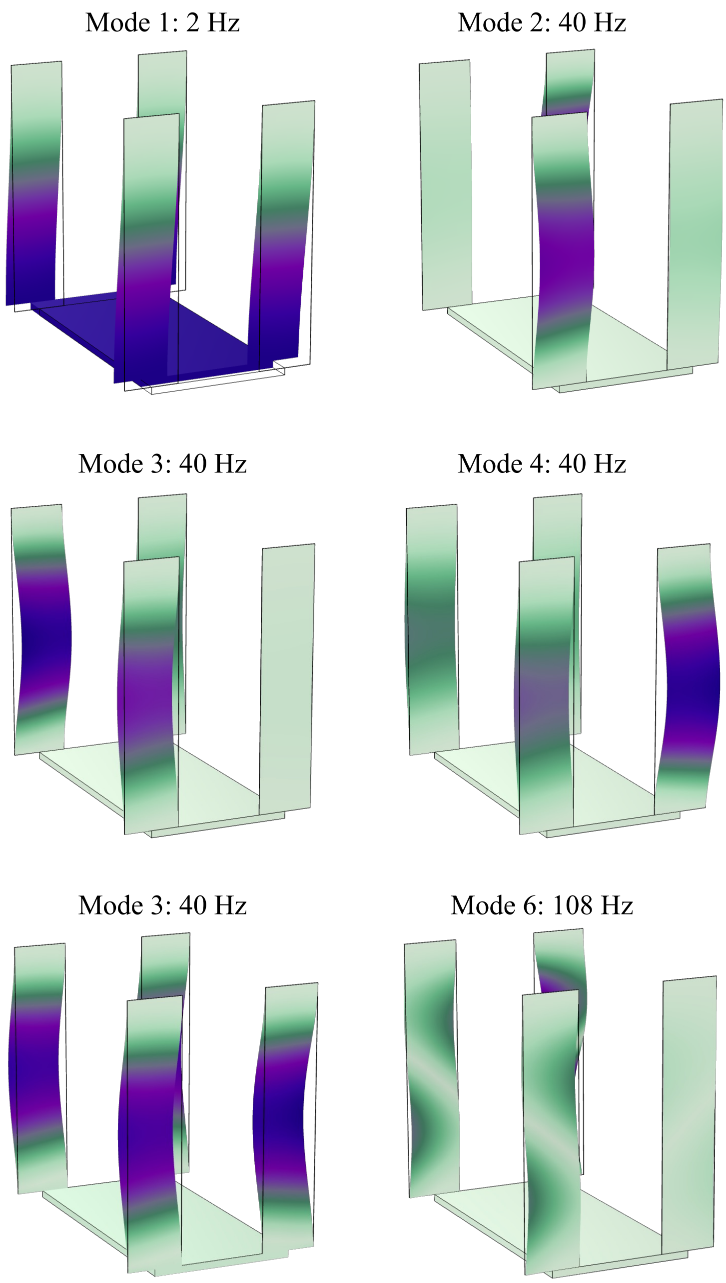

Figure 5.5: Simulated Eigenfrequencies for the first six modes of a softer platform made of copper, featuring pillars with dimensions of 5.1 cm x 0.6 mm x 24 cm. This design exhibits lower Eigenfrequencies with displacement limited to a single propagation axis. The difference in vibrational behavior between the two designs has significant implications for the intracavity power of optomechanical cavities suspended from these platforms.

to Doppler shifts due to relative displacements between the optical table and the mirror mounted to the platform inside the dilution refrigerator. We close the fridge and pump vacuum; however, we do not cool down. Fig. 5.7 shows the results of this measurement. We see significant additional broadening with the rigid platform. This is why further measurements have been performed using the soft platform. However, it is worth noting that we did not investigate the direction of the displacements. Furthermore, in the experiments described in this thesis, we mount additional copper braids for improved thermal conductivity of the optomechanical setups. As one cools down the experiments, both the platform and the copper braids become much more stiff, making the system much more complex to describe and simulate as it has been done in this section.

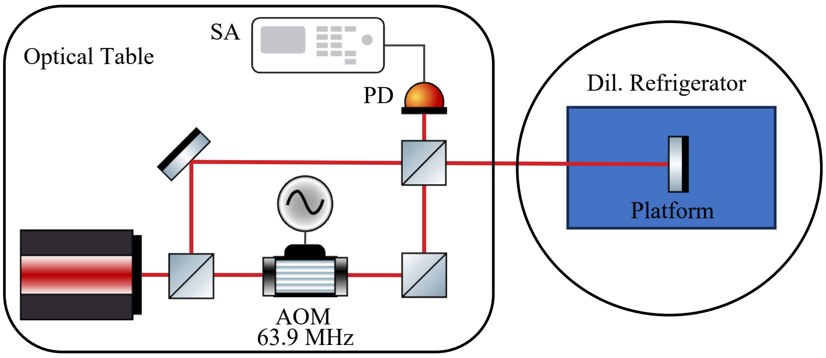

Figure 5.6: Experimental setup to test the vibrational behavior of the rigid and soft copper platforms. A free-space laser beam is sent from an optical table into a dilution refrigerator, where it is reflected off a mirror mounted on each platform in turn. The back-reflected beam's spectrum is analyzed using a heterodyne interferometer scheme. AOM stands for acousto-optic modulator, PD for photodiode, and SA for spectrum analyzer.

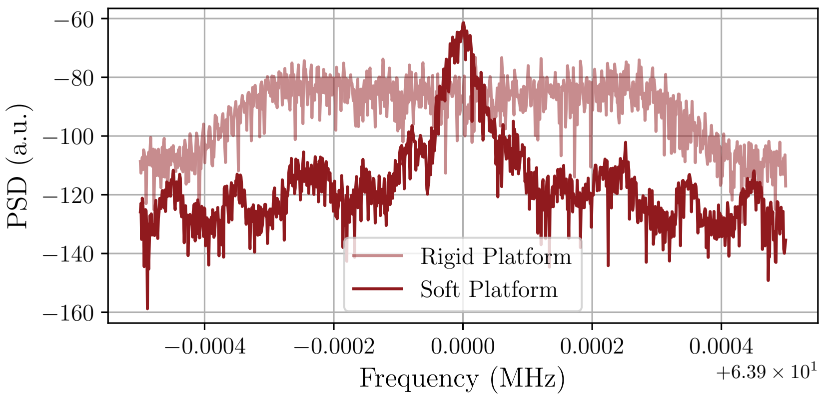

Figure 5.7: Results from the platform vibrational tests. We observe significant additional spectral broadening when using the rigid platform, which we attribute to Doppler shifts due to relative displacements between the mirror (inside the refrigerator) and the optical table. Subsequent tests were performed using the soft platform.

5.3.1 Breadboards Clamped to the Dilution Refrigerator

As fiber-based cavity setups are challenging, requiring meticulous design and alignment choices [Fedoseev *et al.*, 2022] or the use of actuators [Doeleman *et al.*, 2023], we decided to build a free-space optical setup. This allows not only to easily tune the cavity in-coupling but also to monitor the cavity mode in transmission with a camera. Thibault Capelle designed and implemented a circular Aluminum holder holding two standard Thorlabs breadboards that are used for holding optical elements and is also what is used for further experiments in this thesis.

5.4 High-Finesse Optical Cavity at milli-Kelvin Temperatures

We assembled an optical cavity with a pair of high-reflectivity mirrors, as shown in Fig. 5.3. The design of this cavity is shown in Fig. 5.8. Here, the flat cavity mirror is held in place using a silicon spacer that is clamped via a clamping ring to the bottom part of the cavity. The curved mirror is screwed on yet another cavity bulk part. Both mirrors are held in place using nitrile o-rings. This particular cavity is made of aluminum. We observed experimentally that using aluminum screws instead of stainless steel screws to mount cavity parts together is crucial. This could be explained by the thermal contraction coefficients for various materials. The length change, given by

$$\lambda_i = \frac{L_{293\,\mathrm{K}} - L_{0\,\mathrm{K}}}{L_{293\,\mathrm{K}}}\,, \tag{5.1}$$

is 4.15×10^{-3} for aluminum and approx. 2.97×10^{-3} for various stainless steel alloys [Corruccini and Gniewek, 1961]. In later experiments, we used copper cavity parts showing a thermal contraction coefficient of 3.26×10^{-3} [Corruccini and Gniewek, 1961], closer to steel, together with stainless steel screws. In addition, we noticed that it is crucial to keep the cavity mirrors very clean to prevent additional absorption loss or scattering. We apply a polymer solution, First Contact, before preparing an assembly, removing most particles off the mirror surface. We mount the assembled cavity on the vibration-isolated platform as shown in Fig. 5.9 and perform two types of measurements: (i) we measure the cavity linewidth, (ii) we lock the cavity via a Pound-Drever-Hall lock and take a spectrum of the error signal. For both measurements, we use the same optical setup that is shown in Fig. 5.10. The laser beam travels through an electro-optic modulator used to modulate the light amplitude, and another one to modulate the light phase. The laser beam is measured both in back-reflection and transmission.

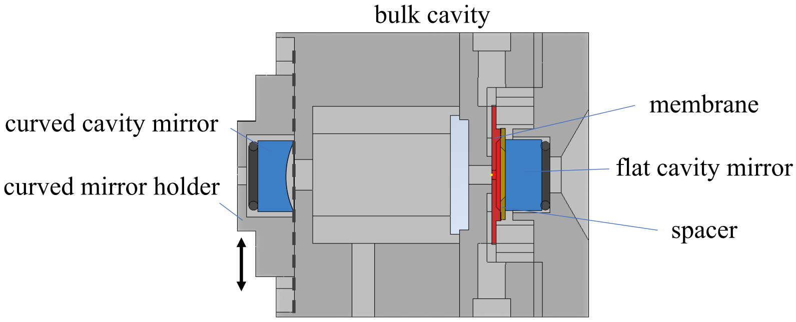

Figure 5.8: Design of the optical cavity used in our experiments. A silicon spacer hold the flat mirror in place and is clamped to the lower cavity part with a clamping ring. The curved mirror is affixed to another cavity part. The cavity is made of aluminum and assembled using aluminum screws due to the thermal contraction characteristics of the materials. Please note that no membrane is included in this assembly, only the spacer. The arrow on the left indicates that the curved mirror holder can be adjusted orthogonally to the cavity axis, a feature relevant for later experiments focusing on the membrane defect.

(i) To measure the cavity linewidth, we tune the laser frequency close to cavity resonance and modulate the light amplitude with a square signal. In transmission, we observe, instead of a square signal, a periodic, exponential decay of the intracavity field towards the photodiode at a rate given by the total cavity loss rate κ. Fitting to

$$P(t) = P_0 e^{-\kappa t} + c \, , \tag{5.2}$$

we can find the cavity linewidth as shown in Fig. 5.11. With five of such cavity ringdown measurements, we find $\kappa/2\pi = (208 \pm 10)$ kHz.

(ii) We modulate the phase with a sine frequency ω_{mod} and measure the cavity response in back-reflection. When mixing the photodiode signal with the modulation frequency and filtering out $2\omega_{\text{mod}}$, we receive what is known as Pound-Drever-Hall signal (PDH signal) [Black, 2001]. We feedback this

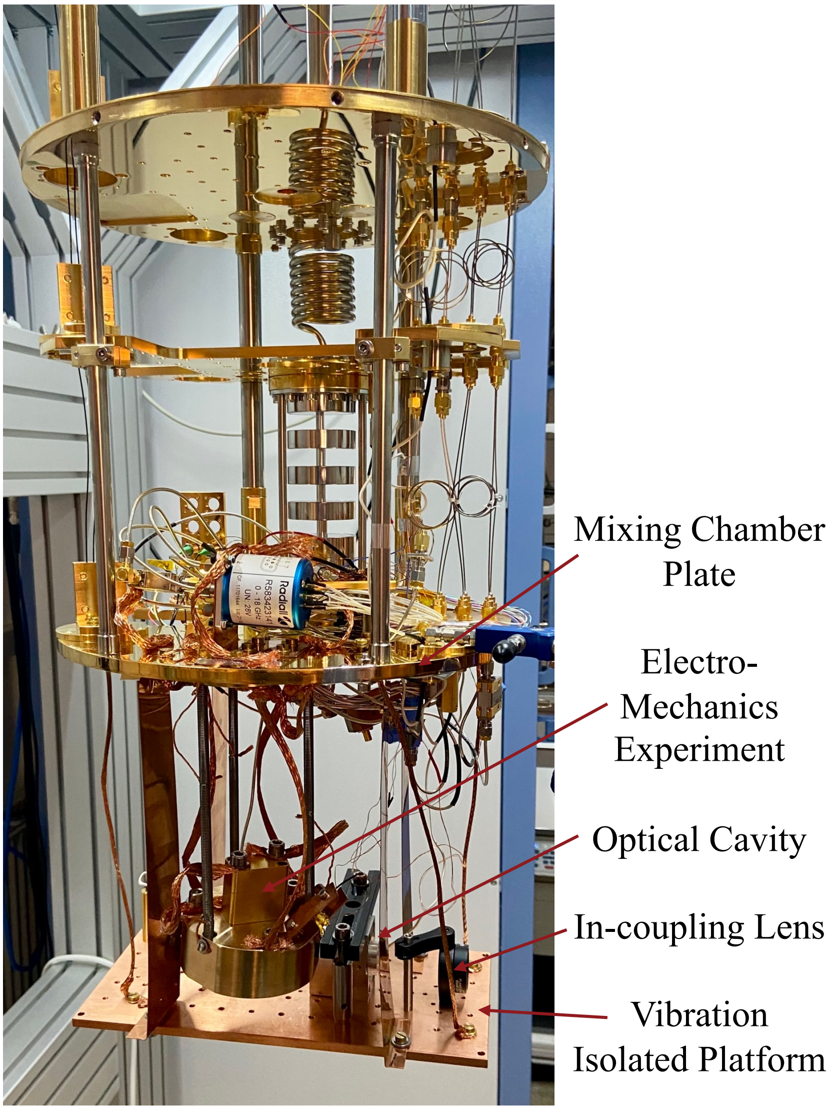

Figure 5.9: Assembly inside the dilution refrigerator for locking a high-finesse optical cavity at milli-Kelvin temperatures. The aluminum cavity is mounted on the vibration isolation platform hanging from the mixing chamber plate. In the front, one can see the electro-mechanics experiment suspected from a spring system, further described in Chapter 4.

PDH signal via a proportional-integral controller (PI controller) to the Piezo of our laser that is actively tuning the laser frequency and manage with this to stabilize the laser to the cavity resonance. While this cavity lock is not nearly as optimized as for the optomechanical cavity presented later in this thesis, Fig. 5.12 shows that we have indeed been able to generally lock to an optical cavity of $\kappa/2\pi = (208 \pm 10)$ kHz corresponding for a cavity length of 23 mm in this setup to a finesse of $(31.3 \pm 1.5) \times 10^3$.

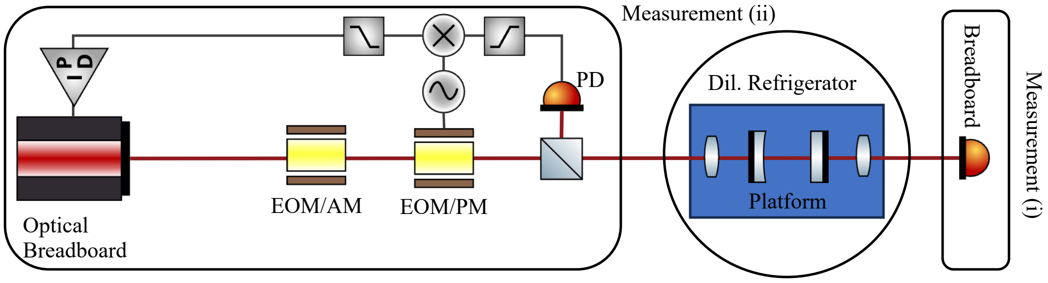

Figure 5.10: The optical setup for cavity linewidth measurement and Pound-Drever-Hall lock spectrum analysis. The laser beam passes through an amplitude modulator (EOM/AM) and a phase modulator (EOM/PM) before being directed into and out of the cavity mounted inside the dilution refrigerator. The reflected and transmitted beams are measured. The lock signal is processed through filters, a mixer, and a PID controller before being sent to the laser piezo.

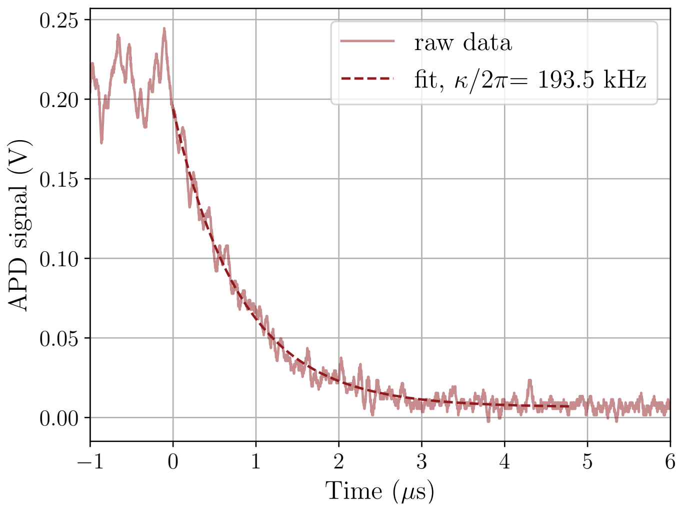

Figure 5.11: Cavity ringdown measurement to determine the cavity linewidth at milli-Kelvin temperatures. We modulate the laser amplitude to create a square pulse and measure the cavity response. The plot shows the exponential decay of the intracavity field and the fit using the loss rate (κ). Five of such measurements yield a linewidth of (208 ± 10) kHz.

5.5 Membrane Design

In order to achieve cavity linewidths as low as shown in Fig. 5.3, additional losses by the mechanical resonator need to be minimized. We found a significant source of loss and show to which design considerations of the membrane resonator it led. The following text is partially based on my text in our recent manuscript in preparation, which is why I am putting this section in quotation

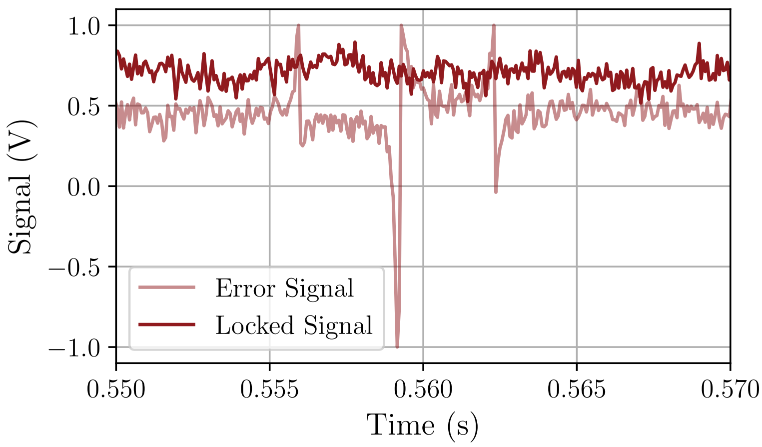

Figure 5.12: Cavity lock at milli-Kelvin temperatures using the Pound-Drever-Hall technique. The plot shows the PDH signal used to stabilize the laser frequency to the cavity resonance, achieving a lock to an optical cavity with a finesse of $(31.3 \pm 1.5) \times 10^3$.

marks.

"In optomechanical systems, the ratio of the defect diameter to the laser beam diameter can introduce additional cavity losses. These are mainly due to clipping along the edges of the silicon nitride (SiN) material and the phase difference between the light field that travels through the material and that outside the defect. This results in altering the cavity wavefront and promotes coupling into higher-order modes. Minimizing these additional cavity losses is crucial to attain sideband resolution, i.e., a cavity linewidth κ smaller than the mechanical frequency Ω_m.

To gain insights into this cavity loss effect, we carried out a series of tests using optomechanical cavity assemblies with varied defect sizes. Fig. 5.13 displays the type of 200 nm thick SiN membranes with a hexagonal structure of holes used in these tests to simulate a soft-clamped membrane defect.

In the assembly procedure for these tests, the membrane and flat cavity mirror are first clamped together. Then a laser beam is orthogonally scanned in x and y direction across the SiN material, and its back-reflected power is measured as shown in Fig. 5.14. These scans show interference between the light reflected directly from the membrane and off the flat cavity mirror behind the membrane. With a scan in x and y direction, the tilt between the membrane and cavity mirror can be calculated from the interference fringe,

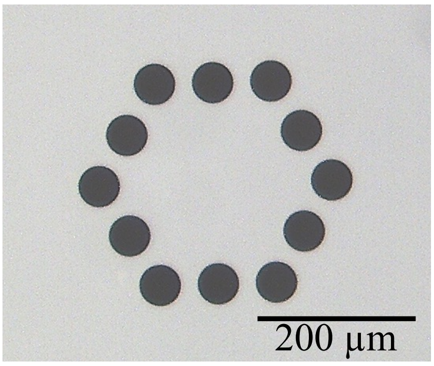

Figure 5.13: The 200 nm thick silicon nitride (SiN) membrane with a hexagonal structure of holes used to simulate a soft-clamped membrane defect. We used membranes with different defect sizes in order to study cavity losses introduced by clipping and phase differences.

which in the example in Fig. 5.14 leads to an angle of approx. 1 mrad for one interference fringe across 0.8 mm with a 830 nm laser beam. For all test assemblies, the angle is kept $<$1 mrad to ensure tilt is not the dominant source of cavity loss. The same scan method is then used to find the center of the cavity defect as in Fig. 5.15, where it has been found to be around 7.93 mm.

The curved cavity mirror is added once the x and z positions are found for the in-coupling laser beam. However, also along the cavity axis y, the position of the membrane with regard to the standing wave of the optical cavity changes the optomechanical coupling. To identify the optomechanical coupling points, we measure the cavity resonance frequency at various free spectral ranges (FSRs). The phase difference inside the SiN material causes a deviation of the resonance frequencies from the FSR splitting given by

$$\omega_{\text{res}} = N\omega_{\text{FSR}} + \frac{\omega_{\text{FSR}}}{\pi}\arctan\left(\frac{\cos(\phi_{\text{r}}) + r_{\text{m}}\cos(2k_N\Delta x)}{\sin(\phi_{\text{r}}) - r_{\text{m}}\sin(2k_N\Delta x)}\right), \tag{5.3}$$

showing a periodicity of $2kz = 2\pi Nz/L$, where N is the number of FSRs, z the distance to the closest cavity mirror, here 1 mm, and L is the cavity length, here 24 mm [Dumont *et al.*, 2019]. From $G = -\partial\omega_{\text{res}}/\partial\Delta x$ as in the model provided in Dumont *et al.*, 2019, we can convert this frequency deviation into a coupling point. To cover the entire periodicity, we record the resonance frequency of 24 FSRs to observe all coupling points and obtain the graph in Fig. 5.16. Subsequently, we perform cavity linewidth measurements via cavity ringdowns at various coupling points, yielding the data presented in Fig. 5.17. The findings demonstrate that the defect size does impact the cavity loss. We found that small defect sizes can lead to significant enough cavity losses that disrupt sideband resolution. Based on these results, we designed our 'Lotus' membranes with a defect size of 230 μm." [Planz et al., submitted to Optics Express].

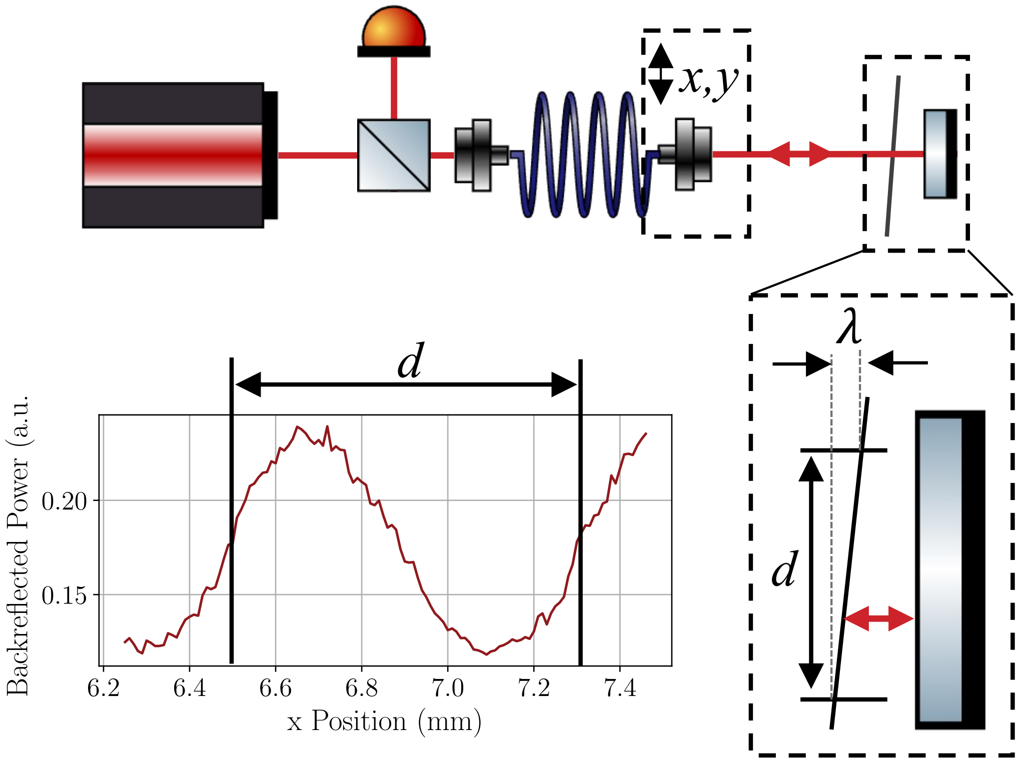

Figure 5.14: Laser beam scanning method to measure the tilt between the SiN membrane (gray line) and the flat cavity mirror. The fiber coupler is mounted on a translation stage and can be moved in plane with the flat mirror. By moving the fiber coupler, interference fringes result from the light reflected directly off the membrane and the mirror are shown. The tilt is calculated from these fringes, where the spacial distance corresponds to height difference between mirror and membrane due to tilt of the laser wavelength λ. In this example, periodicity of 0.8 mm shown in the graph at a laser wavelength of 830 nm corresponds to an angle $\theta \approx \lambda/d \approx 1$ mrad.

5.6 Design with Integrated Electromechanical Access

We revised the design, incorporating all relevant experimental insights described throughout this chapter, to enable electromechanical coupling using

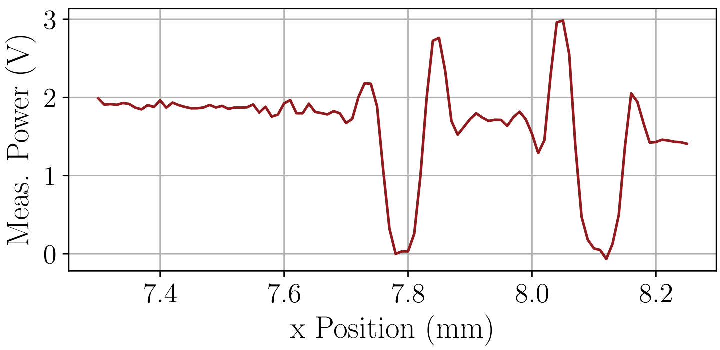

Figure 5.15: Location determination of the cavity defect center by scanning the laser beam across the membrane surface. In this example, the defect center is found at around 7.93 mm.

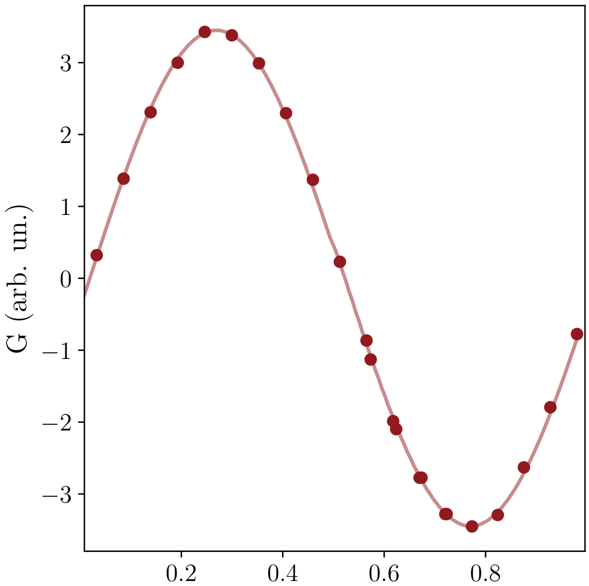

Figure 5.16: Resonance frequencies measured at different free spectral ranges (FSRs) to identify the optomechanical coupling points. Deviation of the resonance frequencies from the FSR splitting due to phase difference inside the SiN material is shown.

the same cavity components. Although the specifics of the electromechanical experiments are discussed more extensively in the subsequent chapter, Fig. 5.18 illustrates the design. A microwave resonator chip is wire-bonded to an SMA connector. The membrane chip and a silicon spacer, similar to those shown in Fig. 5.8, are placed on top of the resonator. The flat mirror and a nitrile o-ring are placed above these components, as depicted in Fig. 5.18(a). These elements are secured using a lid shown in Fig. 5.18(b). The assembly is then attached to the main part of the cavity, shown in Fig. 5.18(c). The

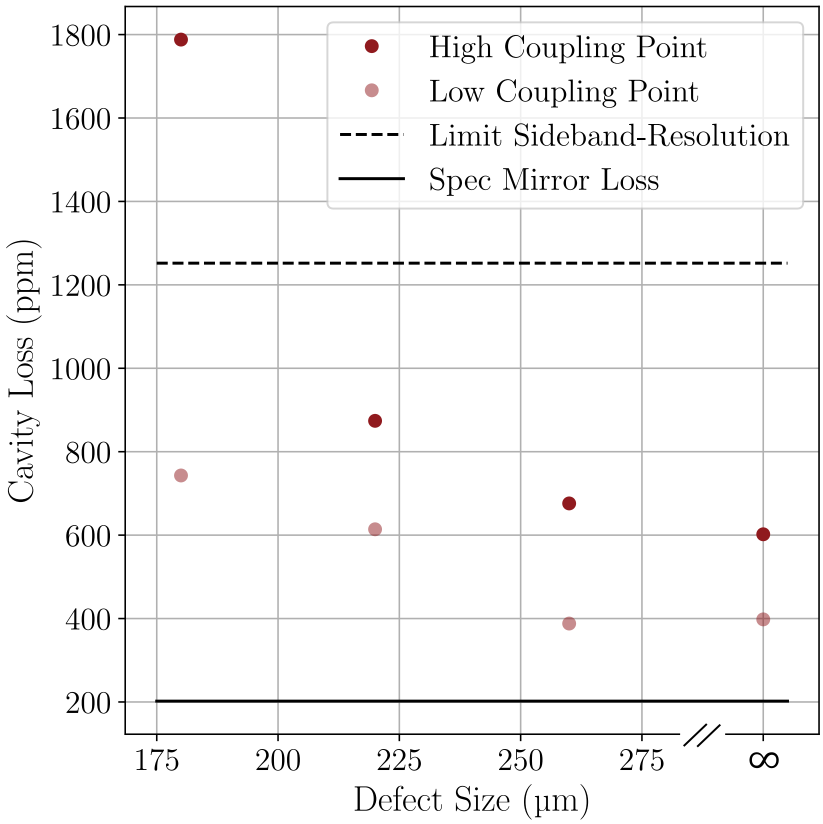

Figure 5.17: Cavity linewidth measurements conducted at various coupling points for different defect sizes. These measurements show how defect size influences cavity loss, with small defects leading to significant losses that disrupt sideband resolution. Data point at defect size ∞ stemming from a plane membrane without any holes simulating a phononic crystal.

curved mirror and another o-ring are attached at the other end of the cavity, as shown in Fig. 5.18(d). These components are secured using the curved mirror holder shown in Fig. 5.18(e), which can be adjusted by approximately 1 mm orthogonal to the cavity axis.

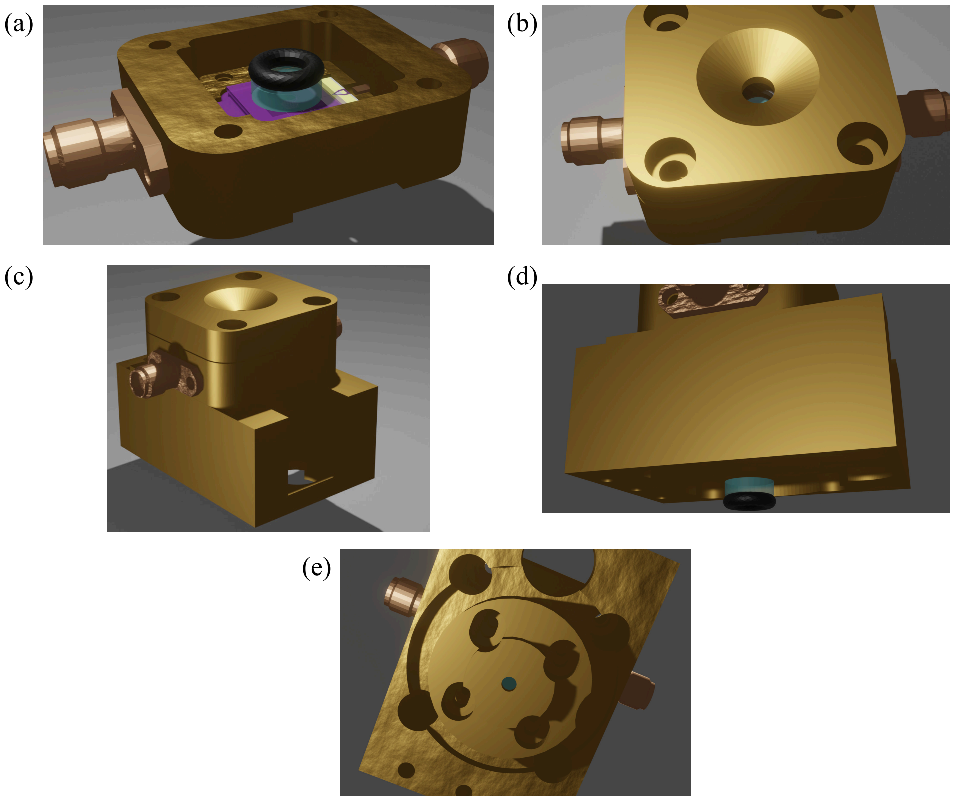

Figure 5.18: Rendered images of the cavity design with integrated electromechanical access. The components include a microwave resonator chip, membrane chip, silicon spacer, flat mirror, o-rings, and curved mirror, secured by specific holders. The design allows adjustments orthogonal to the cavity axis. Blender images by Thibault Capelle.

6 Optomechanical Cooling and Absorption Heating of Soft-Clamped Membranes at Milli-Kelvin Temperatures

Our initial experiments, as shown in Chapter 3, have indicated that optical absorption heating of soft-clamped SiN membranes can cause a noticeable increase in the thermal bath temperature, $\bar{n}_{\mathrm{th}}$. Further, it was observed that the bath temperature has an influence on the intrinsic mechanical decay rate $\Gamma_{\mathrm{m}}(T)$ as shown in Chapter 4. As such, optical absorption can adversely affect the coherence time of the mechanical resonator, given by $\tau = (\bar{n}_{\mathrm{th}}\Gamma_{\mathrm{m}})^{-1}$, and the quantum cooperativity C_{qu}, defined by:

$$C_{\mathrm{qu}} = \frac{4\bar{n}_{\mathrm{cav}} g_0^2}{\kappa \Gamma_{\mathrm{m}} \bar{n}_{\mathrm{th}}} \,. \tag{6.1}$$

This chapter aims to further explore the effect of optical absorption heating via optomechanical cooling of the phononic occupation number of a soft-clamped membrane, situated within a near-sideband-resolved optomechanical cavity at milli-Kelvin temperatures.

6.1 Phonon Occupation of Radiation-Pressure Cooling

As we established in Sec. 2.2.3, the optomechanical interaction leads to the generation of two sidebands with respect of the carrier of the optical field, each with a frequency of Ω_{m}. In this scenario, the blue-detuned sideband (anti-Stokes process) results in the annihilation of a mechanical phonon, while the red-detuned sideband (Stokes process) leads to the creation of a mechanical phonon.

$$\Gamma_{\text{opt}} = A^- - A^+ \tag{6.2}$$

By setting the optical field on the red-detuned side of the cavity resonance, the anti-Stokes process dominates due to the cavity enhancement as described in Eq. 2.20. The Langevin equation for the phonon occupation then comprises two parts and two fields: creation and annihilation, each linked to the optical field and the thermal bath:

$$\dot{\bar{n}} = (\bar{n}+1)\left(A^+ + A^+_{\text{th}}\right) - \bar{n}\left(A^- + A^-_{\text{th}}\right) , \tag{6.3}$$

where $A^+_{\text{th}} = \bar{n}_{\text{th}}\Gamma_{\text{m}}$ and $A^-_{\text{th}} = (\bar{n}_{\text{th}}+1)\,\Gamma_{\text{m}}$. The steady state solution can be expressed as:

$$\bar{n} = \frac{A^+ + \bar{n}_{\text{th}}\Gamma_{\text{m}}}{\Gamma_{\text{opt}} + \Gamma_{\text{m}}} = \frac{\bar{n}_{\text{min}}\Gamma_{\text{opt}} + \bar{n}_{\text{th}}\Gamma_{\text{m}}}{\Gamma_{\text{opt}} + \Gamma_{\text{m}}} , \tag{6.4}$$

where n_{min} refers to the minimum achievable phonon number assuming $\Gamma_{\text{m}} = 0$, which can be determined along with Eq. 2.38 to be:

$$\bar{n}_{\text{min}} = \frac{A^+}{\Gamma_{\text{opt}}} = \left(\frac{(\kappa/2)^2 + (\Delta - \Omega_{\text{m}})^2}{(\kappa/2)^2 + (\Delta + \Omega_{\text{m}})^2} - 1\right)^{-1} . \tag{6.5}$$

When optical absorption heating is present, both Γ_{m} and $\bar{n}_{\text{th}}$ become optical power-dependent. While the theoretical description of the optical power scaling for either parameter is relatively complex for soft-clamped membranes, some experimental results can provide insights into the underlying power scaling. Fig. 3.9 suggests that $\bar{n}_{\text{th}} \propto \bar{n}_{\text{cav}}^{0.36}$ for Dahlia membranes, while for Dandelion membranes $\bar{n}_{\text{th}} \propto \bar{n}_{\text{cav}}^{2.29\pm0.69}$. However, this measurement infers the temperature by comparing quality factors for temperature and power sweeps. For Γ_{m}, Fig. S9 in Seis *et al.*, 2022 and the data in Zhou *et al.*, 2019 present a scaling approximation of $\Gamma_m \propto \bar{n}_{\text{th}}^{-2/3}$, which, in combination with Page *et al.*, 2021, infers $\Gamma_{\text{m}} \propto \bar{n}_{\text{cav}}^{-2/9}$.

In this chapter, we aim to measure the phonon occupation for various optical powers of the cooling beam, with the objective of determining the power scaling of these two parameters.

6.2 Mechanical Resonator

The mechanical resonator utilized in this study is a Lotus membrane characterized by two distinct defects, as depicted in Fig. 6.1. These two defects form a phononic dimer that shares two delocalized modes shown in Fig. 6.2, mirroring the behavior described for a double-defect Dahlia membrane in Catalini *et al.*, 2020. The membrane hosts one defect that is receptive to optical addressing and another, with a square metalization of aluminum, that couples to a microwave resonator. This microwave resonator chip includes a radial hole of $750\ \mu$m in diameter, positioning the optical defect directly in the path of an optical cavity mode. The optical defect spans $230\ \mu$m, a size determined in Sec. 5.5 to enable sideband-resolved optomechanics operation. The microwave resonator paves the way for transduction experiments in the future. It's important to note that the design depicted here does not incorporate the microwave incoupling antenna because it represents a previous design iteration, in which we employed inductive coupling from below rather than a coplanar approach.

6.3 Optomechanical Cavity

We insert this membrane into a cavity assembly, as detailed in Sec. 5.6. We then undertake scans parallel to those described in Sec. 5.5. This allows for accurate positioning of the incoupling laser beam to target the center of the optical defect, as illustrated in Fig. 5.15. Following this, we introduce the curved cavity mirror. Regrettably, since Chapter 5, due to technical complications with the Msquared laser, we are unable to execute a comprehensive 2kz measurement. Nonetheless, we manage to gauge the cavity linewidth at 3 FSRs. The results of this are portrayed in Fig. 6.3, demonstrating clear sideband-resolution of the optomechanical cavity.

6.4 Measurement Setup

The optomechanical cavity is mounted on a soft vibration isolation platform, as outlined in Sec. 5.3. To interact with the cavity optically and execute

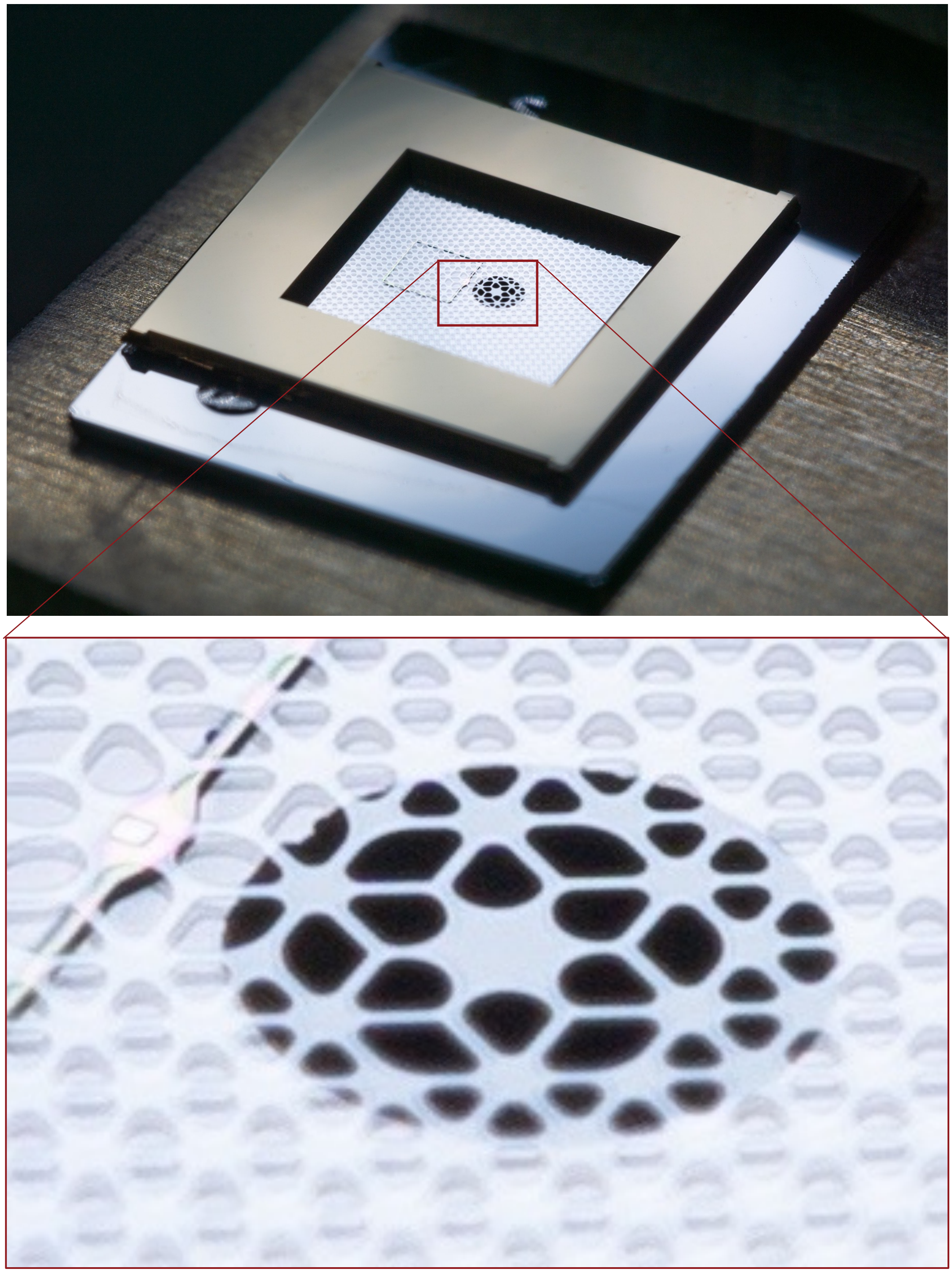

Figure 6.1: Photograph of the soft-clamped Lotus membrane showcasing two defects: one situated over a microwave resonator on the left, and the other on the right, positioned within a 750 μm hole in the Si chip of the microwave chip, permitting membrane-in-the-middle cavity optomechanics.

credible optomechanical cooling experiments with a red-detuned beam, we employ two laser beams originating from the same laser as shown in the drawing of the optical setup in Fig. 6.4. A picture of the optical setup on the

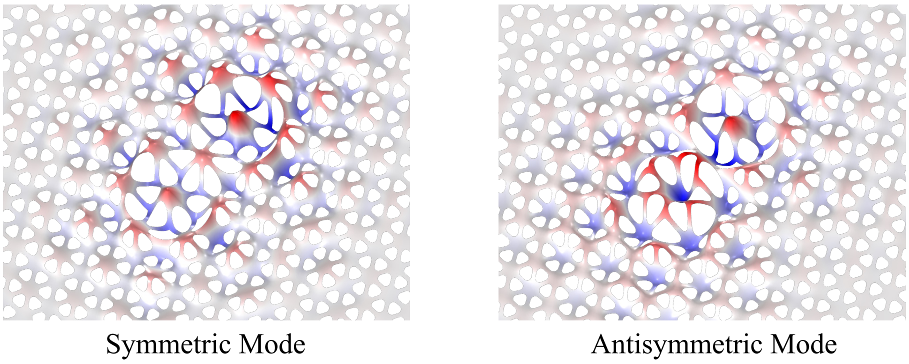

Figure 6.2: Simulation of the symmetric and antisymmetric mode of the phononic dimer with the optically addressable mechanical defect in the top right. In this color code, blue stands for negative displacement, gray for low displacement and red for positive displacement. Simulation by Eric Langman.

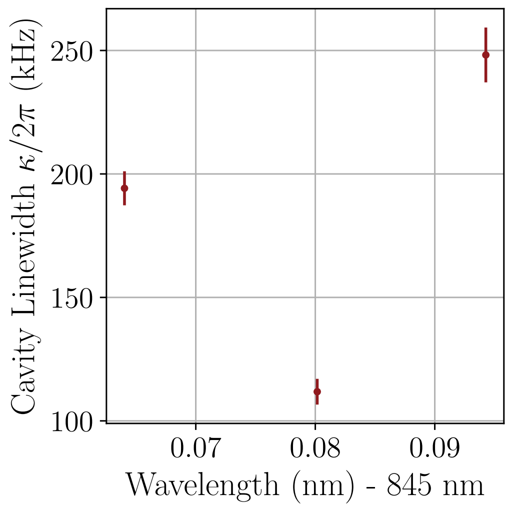

Figure 6.3: Ringdown measurement of the cavity linewidth at 3 FSRs, showing clear sideband-resolution, i.e., $\kappa/2 < \Omega_\mathrm{m}$ of the optomechanical cavity at room-temperature.

breadboard mounted to the outer shell of the dilution refrigerator is shown in Fig. 6.5. One laser is used to lock on cavity resonance, while the second one is utilized as the red-detuned 'science' beam. Given that we aim for a frequency difference on the order of magnitude of $\Delta/2\pi \approx \Omega_\mathrm{m}/2\pi \approx 1.5$ MHz, one of the laser beams is passed through two acousto-optic modulators, where their frequency difference can be in the MHz regime. To maintain minimal leak-through into the science detection of the other beam frequency that will be detuned by approx. Ω_m, we carry out this process with the lock beam. Subsequently, the lock beam travels through an electro-optic phase modulator, which is responsible for generating a Pound-Drever-Hall error signal to lock the laser beam on cavity resonance. The science and lock lasers are polarization filtered to be linear polarized in different polarizations with respect to each other. After polarization filtering, their optical power stabilized, which could drift due to changes in fiber incoupling or polarization drifts, using two photodiodes, PD 2 and PD 4. For the lock beam, power stabilization is achieved by controlling the RF voltage sent to one of the two AOMs. Similarly, the science beam's power is stabilized by controlling the voltage sent to an electro-optic amplitude modulator. Both photodiodes' voltages are calibrated from PD voltage to optical power before conducting any measurements, with calibration achieved through a linear calibration function with offset after measuring the PD voltage with a blocked laser beam and with the laser beam on. When using this feedback to control laser power, we additionally ensure to avoid saturating the photodiodes to remain in the linear power-to-voltage regime of the diodes.

Both laser beams' back-reflection from the optomechanical cavity is measured. The back-reflection of the lock beam on PD 3 is employed for the Pound-Drever-Hall lock. The optical sidebands are produced at 10 MHz, both generated and demodulated by a RedPitaya with a high pass filter before demodulation. The demodulated error signal is filtered at a frequency of 600 Hz to further reduce noise in the electronic measurement. This demodulated error signal is then used to control both the slow and fast piezo of the Msquared Ti:sapphire laser, tuning the laser frequency. Fig. 6.6 depicts the scheme of how the demodulated error signal is used to control both piezos and Fig. 6.17 shows the error signal at as low as 2 nW optical input power. The error signal is then sent to a New Focus LB1005-S high-speed servo controller, where the overall gain and P-I corner (the frequency from which the product gain dominates over the integral gain) are controlled. The output is split, with one part going directly to the fast piezo of the laser and the other one being further low-pass filtered in a RedPitaya at 10 Hz, then sent to the slow piezo of the laser. This approach enables us to achieve a stable lock to the optomechanical cavity over days.

The measurement of the back-reflected science beam, i.e., the red-detuned beam, is routed to a Rohde&Schwarz spectrum analyzer, where we can detect the mechanical sideband.

A thermal spectrum at room temperature is measured, as shown in Fig. 6.7.

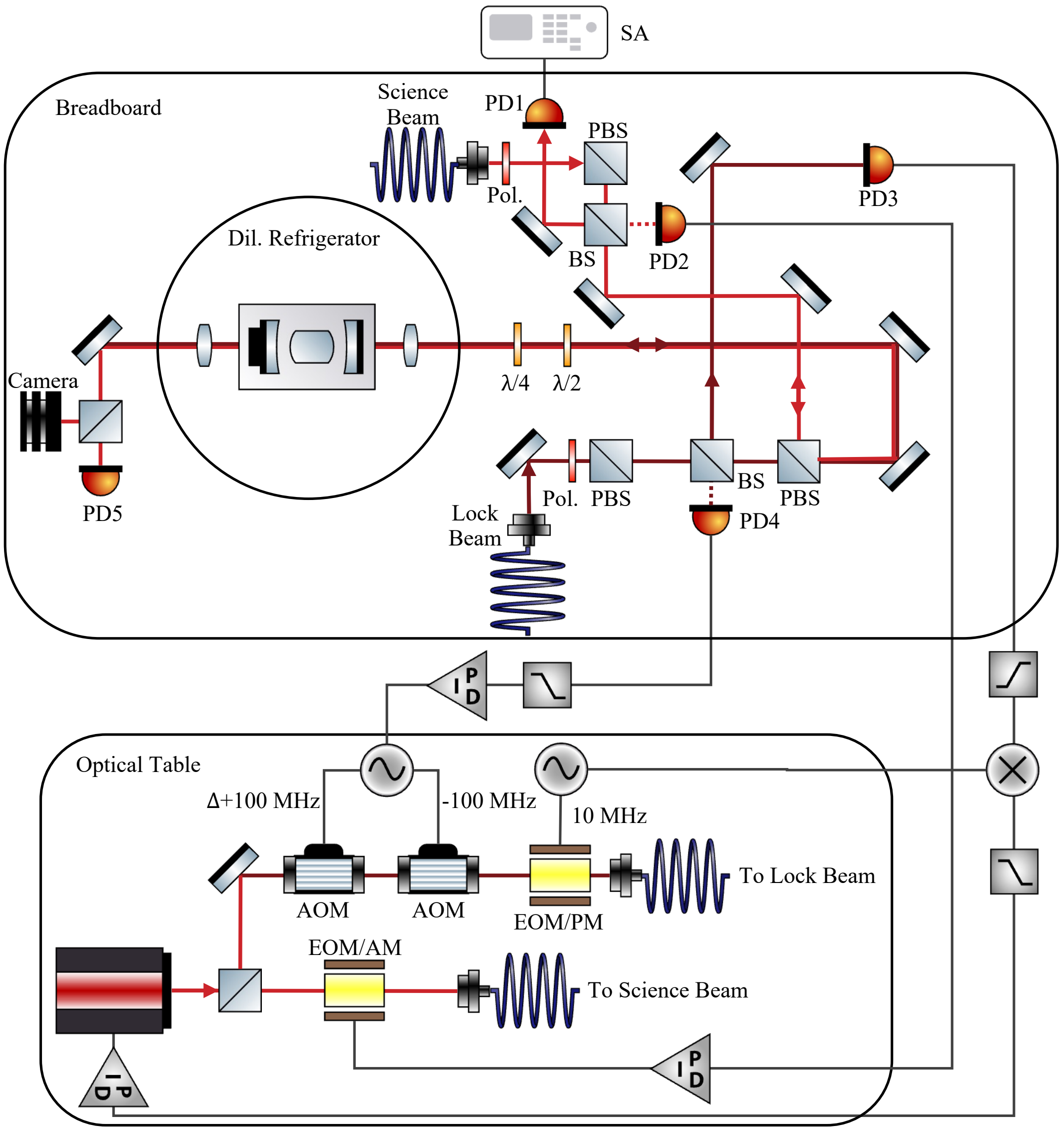

Figure 6.4: "Experimental Setup. Diagram shows the generation of lock and cooling beam via two acousto-optic modulators (AOM) as in Brubaker *et al.*, 2022. The optical power is controlled and monitored via the AOM amplitude and an amplitude modulator as well as PD2 and PD4. The laser frequency is locked to the cavity via an error signal detected on PD3 and feed back to the slow and fast piezo of the Ti:sapph laser. The optomechanical cavity is mounted on the vibration isolation platform inside the dilution refrigerator together with two in- and out-coupling lenses. Spectra are taken in back-reflection and measured on PD1. In addition, the cavity mode can be monitored in transmission via a Camera and PD5." Figure and caption repreduced from Planz et al., submitted to Optics Express

Here, we can clearly observe the bandgap of the membrane design, which lies between approximately 1.28 MHz and 1.4 MHz. We identify two distinct modes. As we monitor the alignment to the optomechanical cavity during cooldown, we retake the spectrum at 4 Kelvin, depicted in Fig. 6.8. A notice-

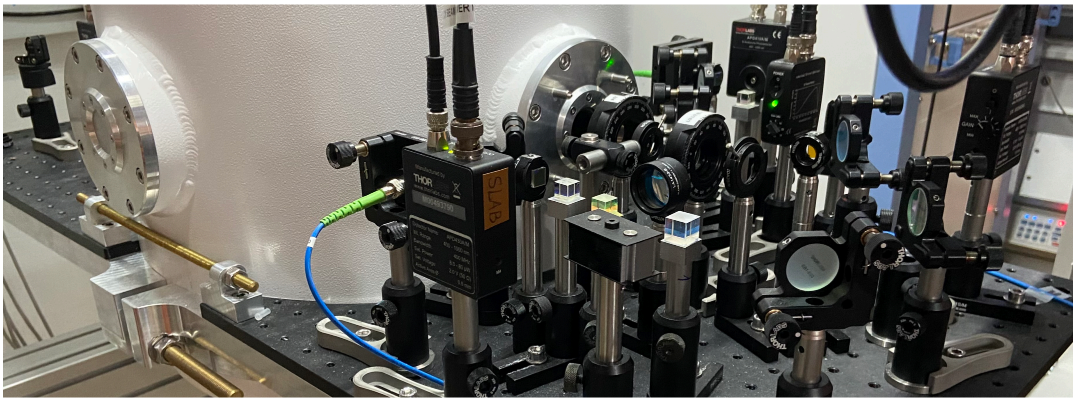

Figure 6.5: Picture of the optics mounted on the breadboard as described in the schematic of Fig. 6.4

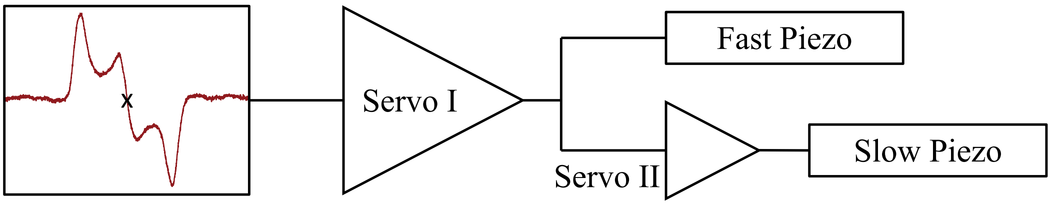

Figure 6.6: Schematic representation of the signal control process for the laser piezos, illustrating how the demodulated error signal is processed and used to control both the slow and fast piezos. The lock point is set to be on cavity resonance, indicated by the 'x' in the error signal. Servo I represents the New Focus LB1005-S high-speed servo controller, while Servo II represents a RedPitaya.

able down-shift in the frequency of both resonances by approximately 2% can be observed.

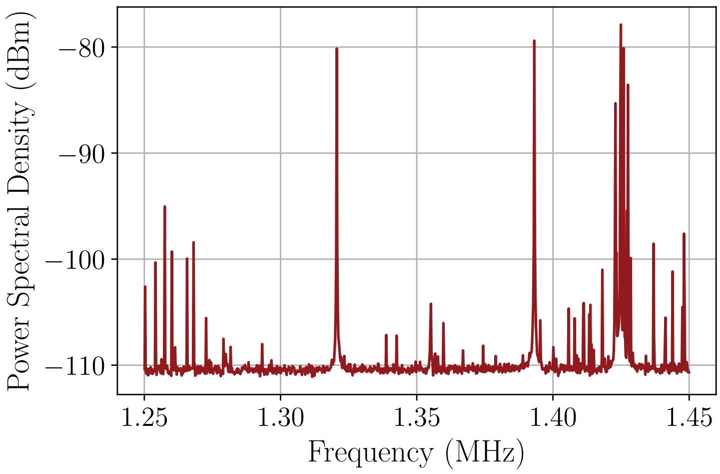

Figure 6.7: Thermal spectrum at room temperature, showcasing the membrane design's bandgap and the presence of two distinct modes.

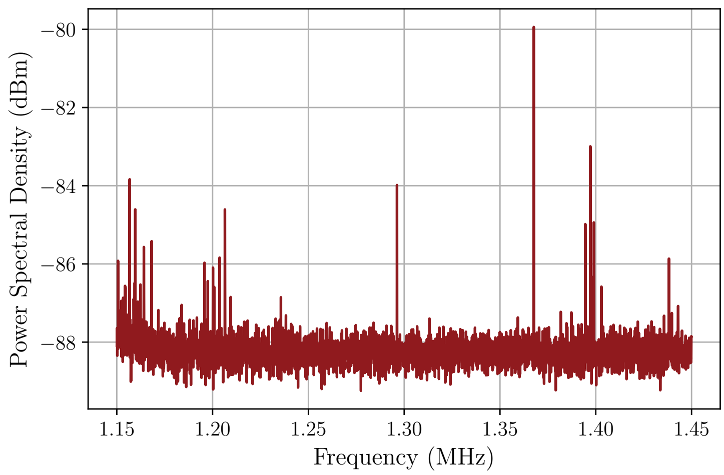

Figure 6.8: Spectrum at 4 Kelvin, displaying a notable down-shift in the frequency of both resonances.

We also gauge the leak-through of the original beam frequency resulting from passing through the two AOMs in our setup. A representative diagram and the consequent result can be found in Fig. 6.9 and Fig. 6.10. One AOM contributes an addition of 101.5 MHz, while the other subtracts 100 MHz. We overlap the beam with a local oscillator that did not propagate through the AOMs as in Fig. 6.9 and record a spectrum at 1.5 MHz. We observe a strong beat signal as shown in the light red curve in Fig. 6.10. We repeat the measurement without the local oscillator and compensate for the change in optical power (see identical noise level to previous measurement), shown in the dark red curve. We observe a 71 dB reduction in the signal at 1.5 MHz. Nonetheless, we adopt additional precautions to minimize cross-talk. Polarizers are em-

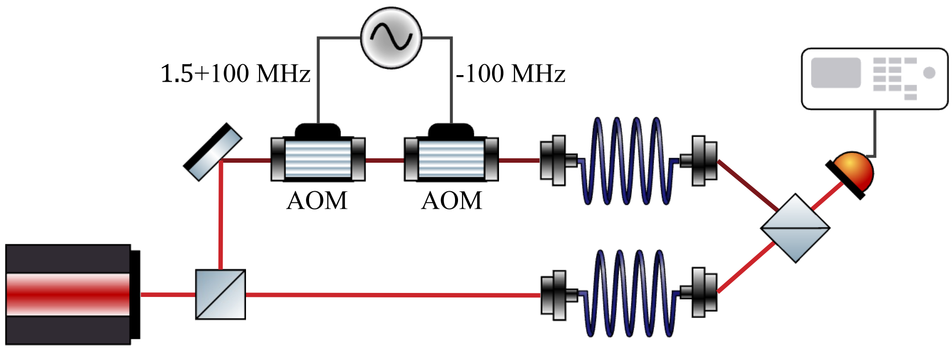

Figure 6.9: Cross-talk spectrum measurement of fiber-coupled acousto-optic modulators in the experiment, showing a reduction of 71 dB at a spectrum of 1.5 MHz.

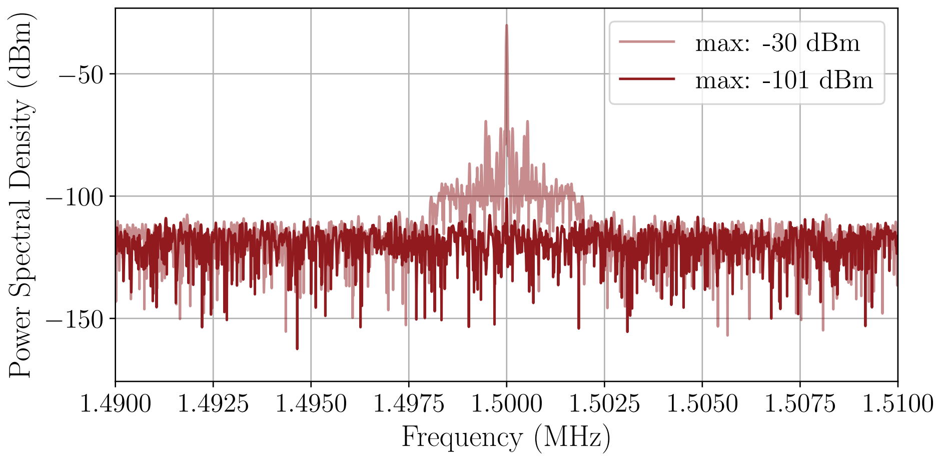

Figure 6.10: Cross-talk spectrum measurement of fiber-coupled acousto-optic modulators in the experiment, showing a reduction of 71 dB at a spectrum of 1.5 MHz.

ployed after both fiber couplers on the optical breadboard, to orient the lock and science beam in separate polarizations, indicated in black behind the red polarizers in the schematic of the setup in Fig. 6.4. Additionally, $\lambda/2$ and $\lambda/4$ waveplate are included to adjust for the birefringence effects from the optical cavity or the dilution refrigerator windows. These precautions, while seeming overcautious, have their value, as I will demonstrate with measurement results from an experiment where the waveplates were not adequately optimized and significant cross-talk was evident in the measurement.

Figure 6.11 presents two cross-talk spectra measured at the science beam photodiode for different orientations of the $\lambda/2$ and $\lambda/4$ plates that are used to compensate for birefringence. We first measure with the not optimized cross-talk spectrum. In this configuration, as we modify the optical power in the science beam, we observe significant cooling at approximately 1.39 MHz, indicating squeezing of the mechanical mode, as illustrated in Fig. 6.12 and being described, e.g. in Nielsen *et al.*, 2016. However, the same feature is visible on the other side of the cross-talk peak, and we note this feature's frequency shifts when the detuning between lock and science beam is varied. Therefore, we conclude that this feature is actually a bulk mode of the membrane chip, not the fundamental mode of the mechanical defect. A further confounding factor is the background noise level, which scales linearly, suggesting that it is shot-noise limited. This, however, is not accurate. The linear power scaling arises from the cross-talk term, which also scales linearly. The measurement shows how crucial the reduction of cross-talk is in such measurements.

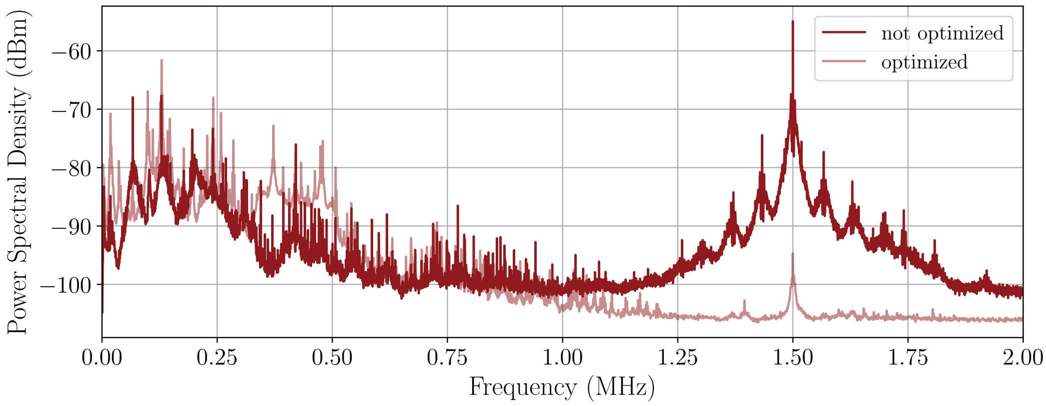

Figure 6.11: Cross-talk spectra for different orientations of $\lambda/2$ and $\lambda/4$ plates.

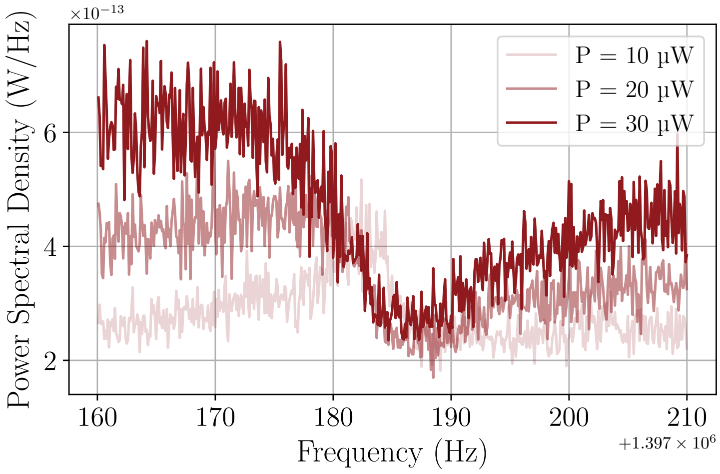

Figure 6.12: Illustration of observed mechanical mode squeezing at approximately 1.39 MHz under varying optical power conditions in the science beam.

6.5 Results

We conducted multiple measurements of the mechanical spectrum, varying the detunings of the cooling beam, optical powers of the science beam, and dilution refrigerator temperatures. Fig. 6.13 displays a set of spectra from one of the optical power sweeps. The spectra are computed by taking the Fourier transform of I-Q traces that are 20 seconds long, and averaging over 40 spectra. The lock beam is maintained at a power of 2 nW. The lock and detuning are stable enough to prevent noticeable shifts in the resonance frequency or amplitude within the 40 contained spectra and one averaged spectrum. However, for narrower optical linewidths, we encounter the bandwidth limit of the IQ trace, implying that the Lorentzian peak is barely resolved, as demonstrated in

Fig. 6.14.

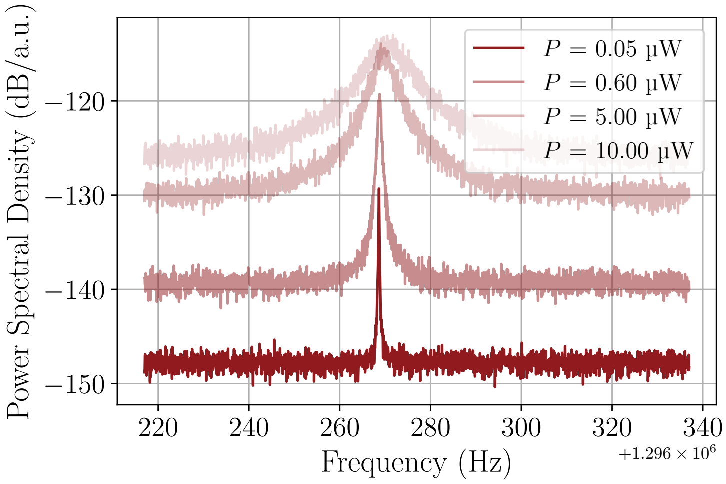

Figure 6.13: Set of spectra from optical input power P sweeps, computed via Fourier transformation of I-Q traces and subsequent averaging. Showing a shift in resonance frequency and linewidth broadening due to dynamical backaction.

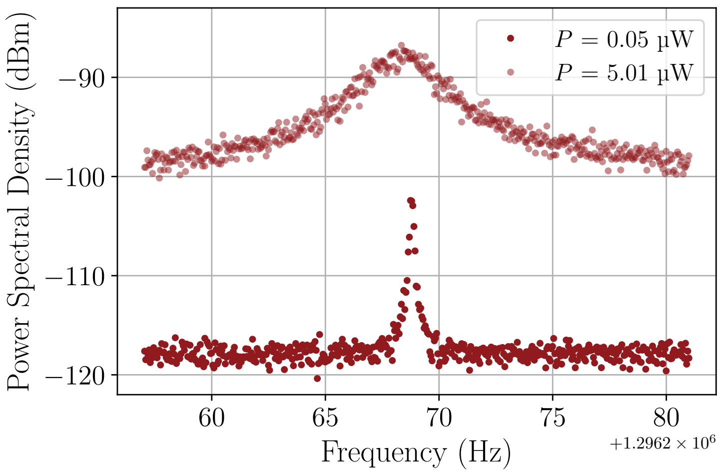

Figure 6.14: Two averaged Fourier spectra at optical input powers P at a detuning $\Delta/2\pi = 2$ MHz. At low optical powers, where the linewidth is ≈ 100 mHz, the Lorentzian fit is limited by the spectral resolution.

The cross-talk between lock and science beam is minimized by the steps discussed in the previous section. Fig. 6.15 shows expanded spectra of the science beam. We carry out sweeps of the optical power for the set detunings between lock and science beam of $\Delta/2\pi = -1.0$ MHz, -1.5 MHz, -2.0 MHz and at the set temperatures of the dilution refrigerator of $T_{\text{set}} = 20$ mK, 100 mK, 300 mK. We then perform Lorentzian fits on the mechanical peaks of the spectra and illustrate their resonance frequency, mechanical linewidth, and background noise level in Fig. 6.16.

As expected, we notice different shifts in resonance frequency for different detunings due to the optical spring effect described in Sec. 2.2.3 and Fig. 2.6(a). Additionally, the mechanical linewidth follows the expected pattern due to dynamical backaction for different detunings as outlined in Fig. 2.6(b). We do observe a linear scaling of the background noise level. However, it is not yet clear from this data whether it is quantum noise limited.

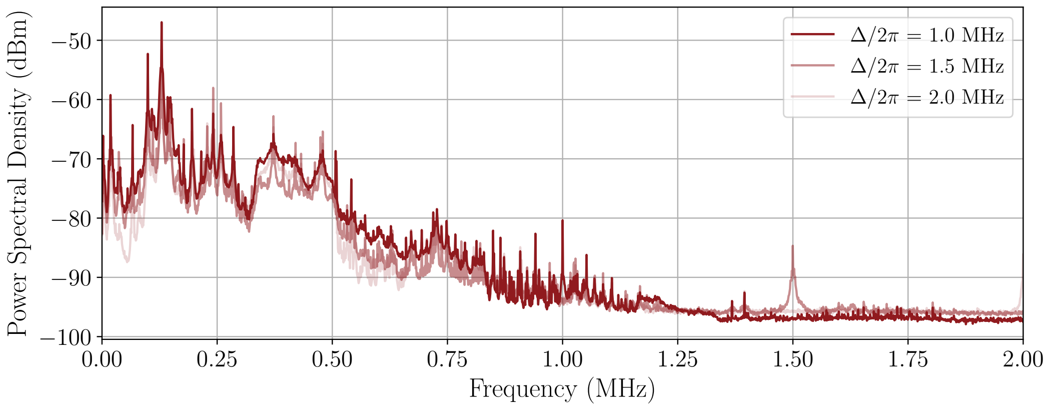

Figure 6.15: Broad spectra of the science beam, conducted through sweeps of the optical power at set detunings and dilution refrigerator temperatures.

To further characterize the characteristics of the optomechanical system, we aim to derive the coupling strength g_0, the cavity linewidth κ, and the detuning of the cooling beam to cavity resonance that might be offset by not locking the lock beam directly on cavity resonance $\Delta' = \Delta + \omega_{\text{offset}}$. These three parameters will allow to find the multi-photon coupling strength $g = g_0\sqrt{\bar{n}_{\text{cav}}}$ at which we have been performing thermometry measurements.

We obtain the cavity linewidth by fitting the Pound-Drever-Hall (PDH) signal of the lock beam, as depicted in Fig. 6.17. This measurement is performed multiple times, yielding a cavity linewidth of $\kappa/2\pi = (2.0 \pm 0.2)$ MHz. Given that the PDH signal output has undergone low-pass filtering at a frequency of 600 Hz, we adjust the laser frequency's ramp scan speed to a lower value. However, the derived linewidth can be viewed as an upper limit for the anticipated linewidth. Additionally, we calculate the mechanical damping rate, $\Gamma_{\text{m},0}$. For this, we utilize an extra data set, captured at a lower optical power range as shown in Fig. 6.18, which exhibits less dynamic backaction broadening. Linear fits yield $\Gamma_{\text{m},0}/2\pi = (79 \pm 3)$ mHz.

To derive the coupling strength g_0 and ω_{offset}, we plot the results of linear fits to the power-dependent frequency shift and linewidth broadening as shown in Fig. 6.19. We then fit their dynamic backaction model to the data using the free parameters g_0 and ω_{offset}. Setting $\kappa/2\pi = (2.0 \pm 0.2)$ MHz, $\kappa_{\text{ex}} = 0.75\kappa$, which is estimated based on the depth of the Lorentzian when scanning over the cavity resonance, wavelength and other parameters, we find as weighted mean and uncertainty on the mean for the two fits combined $\omega_{\text{offset}}/2\pi = (438 \pm 55)$ kHz and $g_0/2\pi = (1.19 \pm 0.03)$ Hz. "For comparison, the maximum achievable coupling rate in a membrane-in-the-middle configuration can be approximated as $g_0^{\text{max}} \approx 2(\omega_c/L)|r|x_{\text{zpf}}\xi$, as in Chapter 3, where $\omega_c/2\pi$ is the cavity resonance frequency, L is the cavity length, r the optical field reflectivity of the membrane, x_{zpf} is the zero-point fluctuation, and ξ is the mode overlap between membrane displacement and optical field Saarinen *et al.*, 2023. With the 50 nm thick membrane and 24 mm long optical cavity, we anticipate $g_0^{\text{max}}/2\pi \approx 8$ Hz at perfect mode-overlap. We attribute the discrepancy with the measured g_0 to the unoptimized positioning of the membrane along the cavity axis and a potentially imperfect transverse overlap ($\xi < 1$)." [Planz et al. 2023, submitted to Optics Express.]

These results reveal $\bar{n}_{\text{min}}$, as described in 6.5, to be $\bar{n}_{\text{min}} < 1$ for all measured detunings. Although we do not have a measure for $\bar{n}_{\text{th}}$, we vary the dilution refrigerator's set temperature and, after 10 minutes of thermalization, measure the mechanical peak's area as given by $A = \frac{\pi}{2}\Gamma h$, where Γ is the linewidth as full width at half maximum and h the height of the peak, at an optical power of 80 nW for the science beam and 3 nW in the lock beam, and at a detuning of $\Delta/2\pi = -1$ MHz. The results are shown in Fig. 6.20. We do not observe an increase in mode area proportional to temperature, as suggested by the fluctuation-dissipation theorem when in equilibrium with the thermal bath. Despite lacking a measure for $\bar{n}_{\text{th}}$, we conclude that we are thermalized at $T \geq 300$ mK, which implies $\bar{n}_{\text{th}} \geq 4.8 \times 10^3$. Additionally, our thermometry analysis only considers spectra taken at $P_{\text{in}} \geq 2\,\mu$W. Thus, for all data points as shown in Fig. 6.16, Γ_{opt} is $10\Gamma_{\text{m}} < \Gamma_{\text{opt}} < 140\Gamma_{\text{m}}$. We therefore draw the conclusions

$$\bar{n}_{\text{min}}\Gamma_{\text{opt}} \ll \bar{n}_{\text{th}}\Gamma_{\text{m}} \tag{6.6}$$

$$\Gamma_{\text{opt}} \gg \Gamma_{\text{m}} \tag{6.7}$$

and we simplify the formula for the steady-state phonon occupation as

$$\bar{n} = \frac{\bar{n}_{\mathrm{th}}\Gamma_{\mathrm{m}}}{\Gamma_{\mathrm{opt}}} \,. \tag{6.8}$$

The area of a Lorentzian curve is given as

$$A = \frac{\pi}{2} h\Gamma \,, \tag{6.9}$$

where h represents the curve's height and Γ denotes the full width at half maximum, in our case the linewidth Γ_{tot} as depicted in Fig. 6.19. Since the photodiode measures a voltage proportional to the optical power, we need to divide by the optical power squared to derive a phonon occupation $\bar{n}_{\mathrm{m}} = m\frac{A}{P^2}$, where m accounts for any gains within the measurement chain. Without calibrating the measurement gain m and the thermal bath occupation $\bar{n}_{\mathrm{th}}$, we cannot ascertain the absolute occupation number. However, we can still extract the phonon occupation's optical power scaling through a fit. The optomechanical damping linearly scales with the optical photon number, $\Gamma_{\mathrm{opt}} \propto \bar{n}_{\mathrm{cav}}$, while the power law scaling of the decoherence rate with the optical photon number remains unknown, $\bar{n}_{\mathrm{th}}\Gamma_{\mathrm{m}} \propto \bar{n}_{\mathrm{cav}}^{\alpha}$. This derives to an overall power law scaling of

$$\frac{A}{P^2} = \frac{1}{m}\frac{\bar{n}_{\mathrm{th}}\Gamma_{\mathrm{m}}}{\Gamma_{\mathrm{opt}}} \propto \frac{\bar{n}_{\mathrm{cav}}^{\alpha}}{\bar{n}_{\mathrm{cav}}} = \bar{n}_{\mathrm{cav}}^{\alpha-1} \,. \tag{6.10}$$

Performing a linear fit on the log-log scale reveals the results illustrated in Fig. 6.21. Taking the statistical mean and standard deviation, we find a power law scaling of the decoherence rate of $\bar{n}_{\mathrm{th}}\Gamma_{\mathrm{m}} \propto \bar{n}_{\mathrm{cav}}^{0.34\pm0.04}$.

In addition, we are summarizing the main characteristics of the optomechanical system in the table below.

6.6 Discussion

We constructed an optomechanical cavity, demonstrating optomechanical cooling within a dilution refrigerator. This cavity was employed to investigate optical absorption heating, which influences both $\bar{n}_{\mathrm{th}}$ and Γ_{m}. As our ability to calibrate the measurement and the thermal occupation was limited, we could only determine the power law scaling of their product—specifically, the thermal

Table 6.1: Summary of parameters of the experiment.

Parameter	**Value**	Method
Optical wavelength	$\lambda = 804$ nm	Wavemeter
Cavity finesse	$F = (3.1 \pm 0.3) \times 10^3$	Fit to PDH Signal
Cavity linewidth	$\kappa/2\pi = (2.0 \pm 0.2)$ MHz	Fit to PDH Signal
Cavity length	$L = 24$ mm	Design & 2kz fit (Eq. 5.3)
Cavity coupling efficiency	$\eta = 0.75$	Measured Back-reflection
Mechanical frequency	$\Omega_\mathrm{m}/2\pi = 1.296$ MHz	Spectrum
Mech. decay rate	$\Gamma_\mathrm{m}/2\pi = (79 \pm 3)$ mHz	DBA fit
Coupling strength	$g_0 = (1.19 \pm 0.03)$ Hz	DBA fit
Thermal bath occupation	$\bar{n}_\mathrm{th} > 4.8 \times 10^3$	Temperature sweep

decoherence rate $\bar{n}_\mathrm{th}\Gamma_\mathrm{m}$. We discovered that it scales as $\bar{n}_\mathrm{th}\Gamma_\mathrm{m} \propto \bar{n}_\mathrm{cav}^{(0.34\pm0.04)}$, which roughly aligns with the literature values discussed in Sec. 6.1. There, $\bar{n}_\mathrm{th} \propto \bar{n}_\mathrm{cav}^{1/3}$ and $\bar{n}_\mathrm{th} \propto \bar{n}_\mathrm{cav}^{2/9}$, implying that $\bar{n}_\mathrm{th}\Gamma_\mathrm{m} \propto \bar{n}_\mathrm{cav}^{5/9}$. Our experiments were conducted at lower optical power levels. We did not repeat measurements across different free-spectral ranges, which could have resulted in varied coupling strengths g_0. Nor did we conduct additional linewidth measurements at higher optical wavelengths that could correspond to greater reflectivity of the cavity mirrors. Despite these limitations, we did note additional cavity losses when compared to Fig. 5.3.

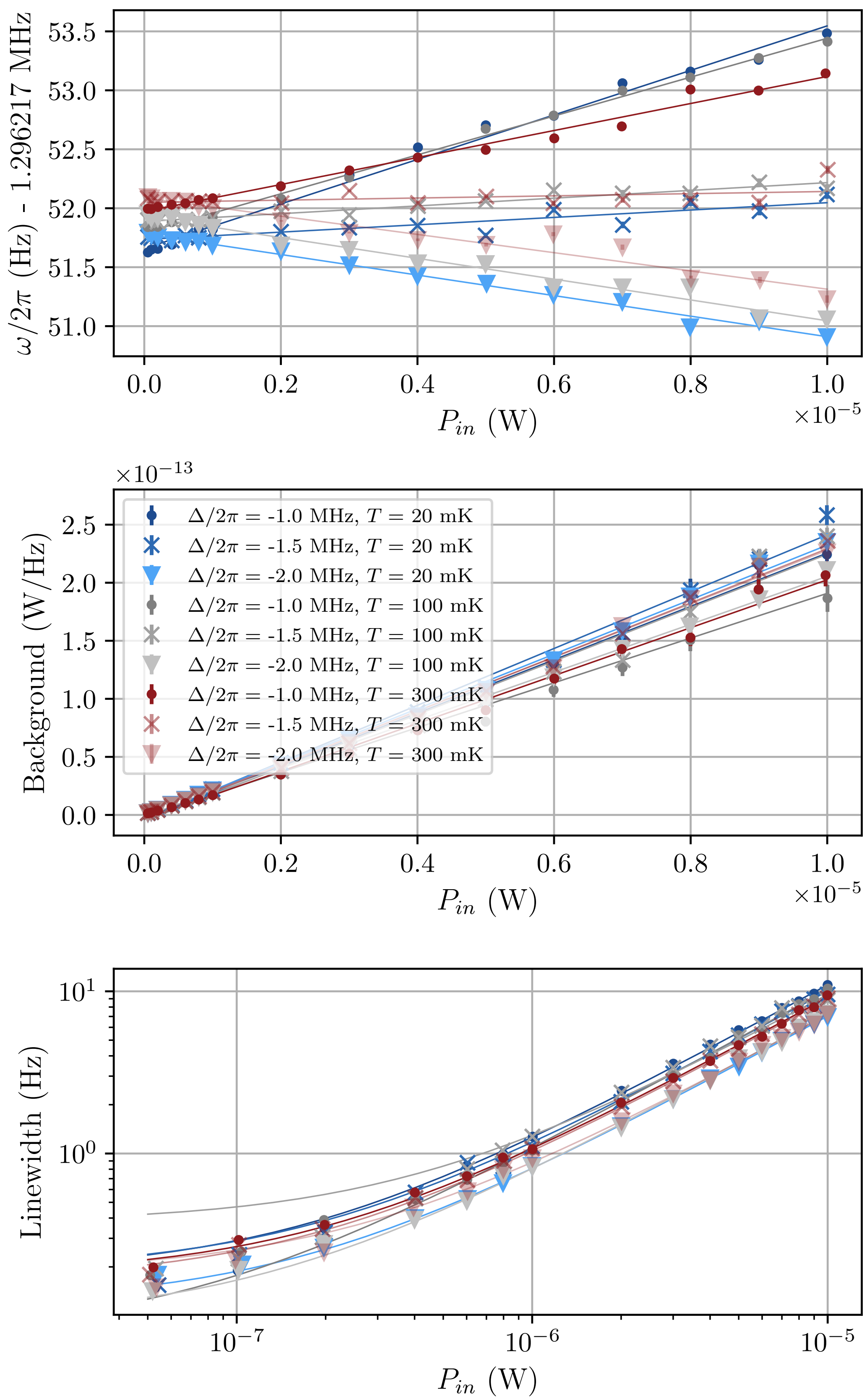

Figure 6.16: Illustration of resonance frequency, mechanical linewidth, and background noise level derived from Lorentzian fits on the mechanical peaks of the spectra. "For example, $P_{\text{in}} = 5\,\mu$W at -1.5 MHz detuning corresponds to an intracavity photon number of 2.2×10^6." [Planz et al. 2023, submitted to Optics Express]

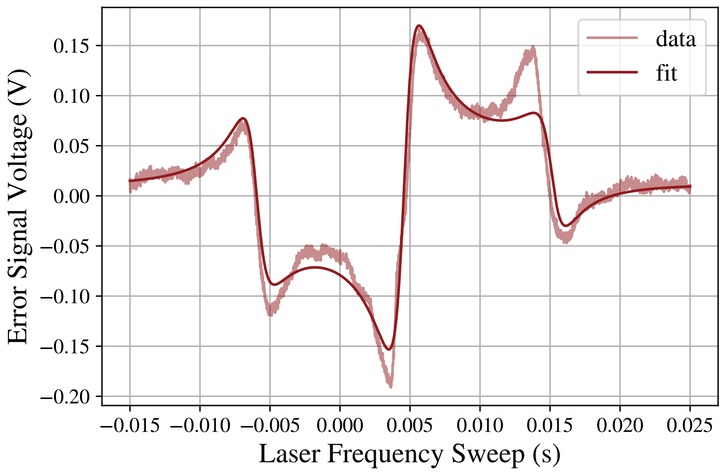

Figure 6.17: Fit to the Pound-Drever-Hall signal at a lock-beam power of 2 nW. We perform the fit at several curves and extract a cavity linewidth of $\kappa/2\pi = (2.0 \pm 0.2)$ MHz.

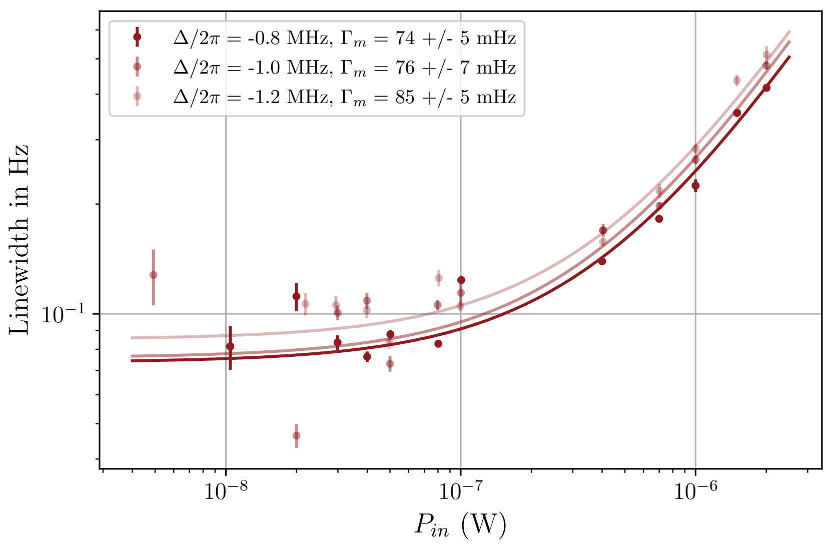

Figure 6.18: Data set captured at a lower optical power range used to calculate the mechanical damping rate, $\Gamma_{\mathrm{m},0}$. The derived rate is determined via linear fits.

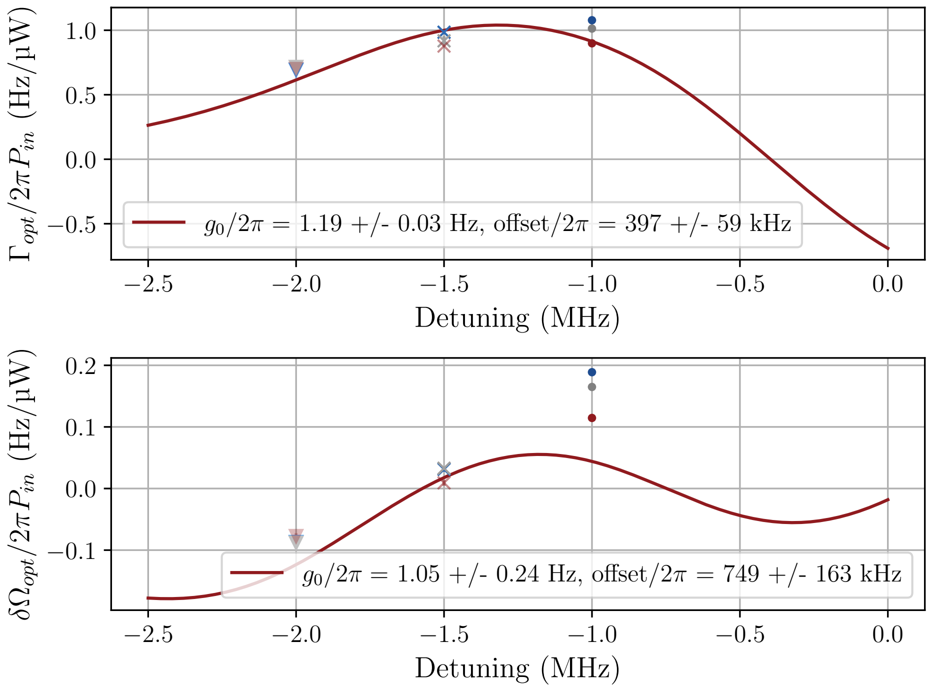

Figure 6.19: Results of linear fits to the power-dependent frequency shift and linewidth broadening utilized to derive coupling strength g_0 and ω_{offset}. The fitted dynamic backaction model is plotted on top the data. “For example, $P_{\text{in}} = 5\ \mu$W at -1.5 MHz detuning corresponds to an intracavity photon number of 2.2×10^6." [Planz et al. 2023, submitted to Optics Express]

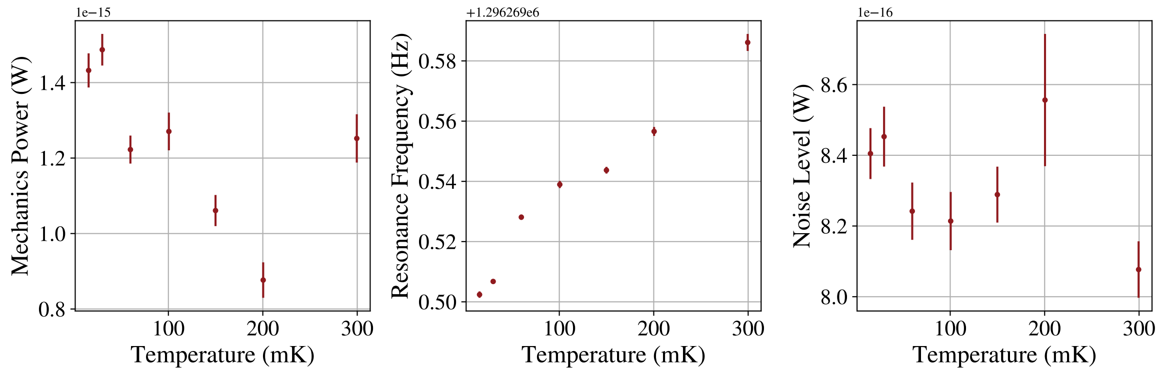

Figure 6.20: Results for the mechanical power, linewidth and background level for a sweep of the set temperature of the dilution refrigerator. Values and error bars given by Lorentzian fits.

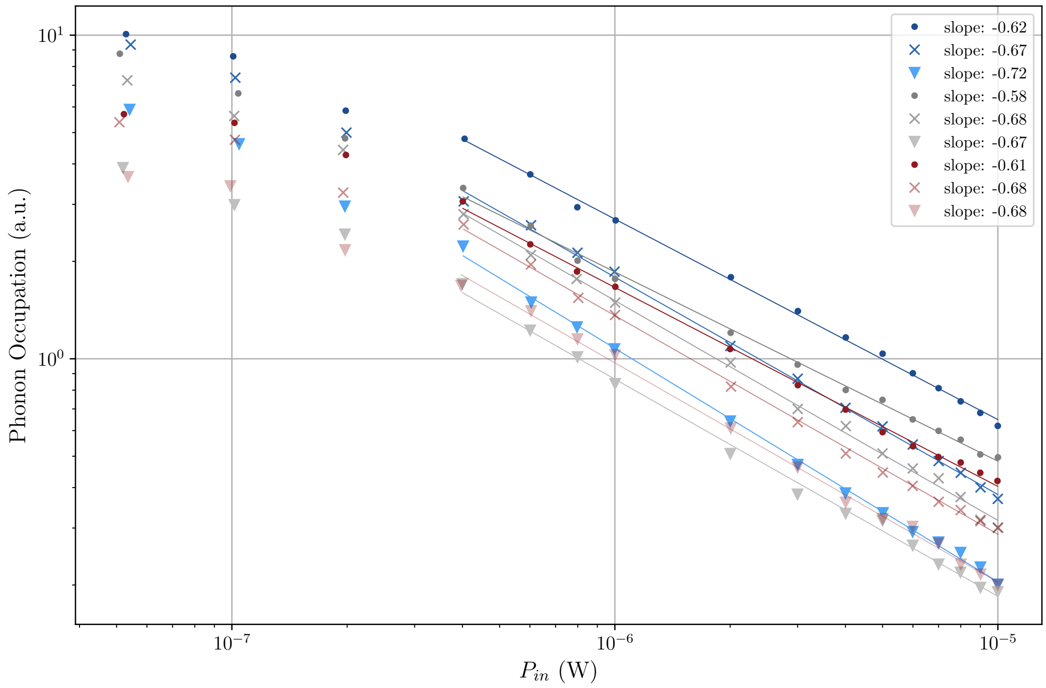

Figure 6.21: Plot of the log-log scale linear fit, revealing the phonon occupation's optical power scaling. Color and marker code identical to 6.16. The statistical mean and standard deviation of the fitted data suggest a power law scaling of the decoherence rate of 0.34 ± 0.04. "For reference, $P_{\text{in}} = 5\ \mu$W at -1.5 MHz detuning corresponds to an intracavity photon number of 2.2×10^6." [Planz et al. 2023, submitted to Optics Express]

7 Conclusion

Throughout this dissertation, I explored electro- and opto-mechanical systems using soft-clamped membrane resonators operating at milliKelvin temperatures. Due to their design, soft-clamped membranes enable reaching extremely low mechanical decay rates, represented as $\Gamma_{\mathrm{m}}/2\pi = 1$ mHz. This, together with effective thermalization to low bath temperatures, leads to coherence times of $\tau = (\bar{n}_{\mathrm{th}}\Gamma_{\mathrm{m}})^{-1} > 140$ ms [Seis *et al.*, 2022]. This feature positions electro- and optomechanical systems using soft-clamped membrane resonators as compelling candidates for quantum memory and low-noise quantum transduction, thus fulfilling a pressing requirement for the further progression of quantum networks.

In this thesis, I showed how we accomplished high cooperativities, i.e., large ratios of the mechanical resonator's coupling to the optical/microwave bath relative to the mechanical decay—depicted as $C = \Gamma_{\mathrm{opt}}/\Gamma_{\mathrm{m}} \gg 1$ for both electro- and opto-mechanical systems. For the electro-mechanical system, we successfully demonstrated cooling to the quantum ground state. However, we identified heating effects in both systems, which posed a damping on the minimal achievable phonon occupation and on attaining high quantum cooperativities, defined as $C_{\mathrm{qu}} = \Gamma_{\mathrm{opt}}/\bar{n}_{\mathrm{th}}\Gamma_{\mathrm{m}}$. To deepen our understanding and increase the electro-/opto-mechanical coupling rate, we undertook several measures, including comparing the heat conductivity of different soft-clamped membrane resonator designs, demonstrating ground-state cooling of an electro-mechanical system and implementing potential future enhancements, establishing sideband-resolved optical cavities and locking them inside a dilution refrigerator, demonstrating optomechanical coupling with a cavity design that can incorporate both opto- and electromechanical systems, and characterizing the optical absorption effect of soft-clamped membranes at milliKelvin temperatures.

(i) We studied the optical absorption heating of a 'Dandelion' membrane, a design characterized by a low effective mass of $m_{\mathrm{eff}} \approx 100$ pg, leading to high coupling strengths of $g_0/2\pi = 2.3$ kHz in other assemblies [Saarinen *et al.*, 2023]. We evaluated the mechanical quality factor across various optical powers and set temperatures, and found substantial heating, stronger than previous measurements with the 'Dahlia' design [Page *et al.*, 2021]. Our COMSOL simulations suggested that this higher heating effect relates to the tether width of the design, resulting in a lower heat conductivity for narrower tethers.

(ii) Utilizing a 'Lotus' membrane, we showcased electromechanical coupling, achieved the mechanical ground state, and deduced coherence times of $\tau = (\bar{n}_{\mathrm{th}}\Gamma_{\mathrm{m}})^{-}1 > 140$ ms [Seis *et al.*, 2022]. Further, we enhanced the design by incorporating wire-bond coplanar incoupling waveguides. We also introduced a cryogenic actuator that permitted tuning of the gap between the microwave cavity and mechanical resonator. From the shift in microwave resonance, we inferred a distance of $d = 131$ nm, which according to Seis *et al.*, 2022, could result in a seven-fold improvement in coupling strength g_0, and thus a 50-fold increase in the electromechanical coupling rate at the same level of microwave heating. Further tests via the electromechanical interaction are anticipated.

(iii) We designed and locked overcoupled optical cavities within a dilution refrigerator, achieving a cavity linewidth of $\kappa/2\pi = (208 \pm 10)$ kHz, corresponding to a finesse $(31.3 \pm 1.5) \times 10^3$. We further investigated with a series of SiN membranes how clipping of the hole structure of soft-clamped membranes affects cavity losses. This led to the design consideration of a mechanical defect size of 230 μm for a 43 μm beam waist for subsequent optomechanics experiments.

(iv) We constructed an optomechanical cavity with a phononic dimer membrane as illustrated in Fig. 6.1, setting the stage for future probing of electro-optomechanics. We tested it within the dilution refrigerator, focusing on optomechanics. We characterized the optical absorption heating effect and discovered $\bar{n}_{\mathrm{th}}\Gamma_{\mathrm{m}} \propto \bar{n}_{\mathrm{cav}}^{0.34\pm0.04}$. This does not prevent us from achieving quantum cooperativity. The coupling strength g_0 was slightly low, but if it can be increased, quantum cooperativity is attainable.

In summary, we are now equipped with the devices to build electro- and optomechanical systems within the same setup. With a comprehensive understanding of the system, electro-optomechanics still remains a viable platform for achieving low-noise transduction.

8 Prospective Directions

Within this thesis, we have managed to build and test electro- and optomechanical systems. Electro-mechanical systems successfully reached a state of quantum cooperativity at an electromechanical coupling rate of $\Gamma_\mathrm{e}/2\pi = 80$ Hz. However, the introduction of higher microwave powers resulted in phase noise levels which hindered quantum cooperativity. For the optomechanical systems, it remains open reach quantum cooperativity - an essential step to achieve ground-state cooling and functioning as a quantum transducer.

As calculated in Sec. 2.4, an important prerequisite for unity efficiency in the transducer is the equality of the coupling rates of both systems, i.e., $\Gamma_\mathrm{e} = \Gamma_\mathrm{opt}$. We identified an absorption heating effect in the optomechanical system inside the dilution refrigerator, a phenomenon characterized in detail in Chapter 6. Fortunately, this effect is less intense than the power scaling for the optomechanical coupling rate, leading us to believe that with the systems illustrated in that chapter, quantum cooperativity can potentially be achieved.

Figure 8.1 depicts the value of quantum cooperativities for different optomechanical coupling rates, using the parameters from Chapter 6. Here, the function is

$$C_\mathrm{qu} = \frac{\Gamma_\mathrm{opt}}{\bar{n}_\mathrm{th}\Gamma_\mathrm{m}\left(1 + (m\bar{n}_\mathrm{cav})^\alpha\right)} = \frac{4g_0^2\bar{n}_\mathrm{cav}}{\kappa\bar{n}_\mathrm{th}\Gamma_\mathrm{m}\left(1 + (m\bar{n}_\mathrm{cav})^\alpha\right)}\,, \tag{8.1}$$

where $\alpha = 0.34 \pm 0.04$ as found in the previous chapter, and m a constant we cannot determine to date without calibration of the thermal bath occupation and set to $m = 1$ in Fig. 8.1.

As per the calculations, quantum cooperativity can be achieved at sufficiently large Γ_opt. Our next objective is to amplify Γ_opt without necessitating an increase in optical power. The following paragraphs provide some possible directions to achieve this.

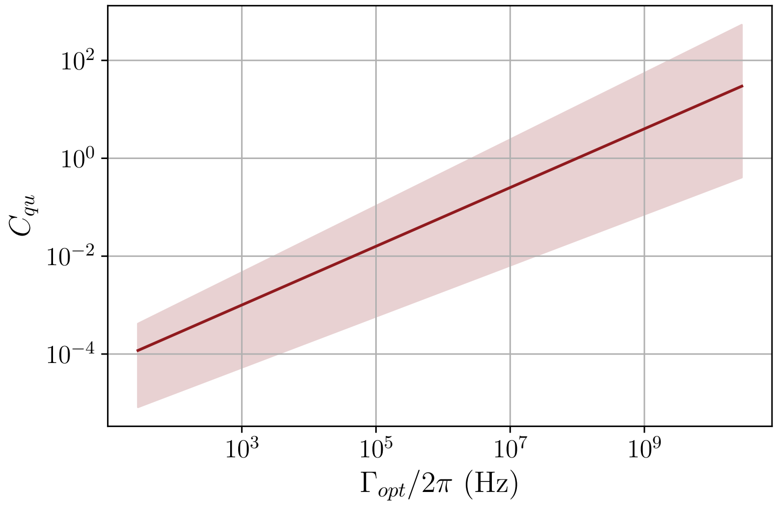

Figure 8.1: Representation of Eq. 8.1 for an intracavity power sweep utilizing the parameters of the optomechanical system defined in Chapter 6. The shaded portion signifies the 95% confidence interval.

During the investigation of the optomechanical cavity detailed in Chapter 6, we measured an optomechanical coupling strength of $g_0/2\pi = (1.19 \pm 0.03)$ Hz. Looking forward, we should consider shifting the laser wavelength to various free-spectral ranges (once the laser repair allows for it) to evaluate different coupling points, similar to the methodology in Fig. 5.16. The goal is to attain high optomechanical coupling Γ_{opt} and low optical absorption heating, which will be possible by operating the system at the highest coupling point in Fig. 5.16, where the optical power at the membrane's position is half of its maximum.

However, as we were unable to address different coupling points in this study, we cannot confirm whether we were operating at a position with low coupling strength, but high optical power on the membrane. Nonetheless, this uncertainty does not impact the power-law scaling derived from this thesis, it would only modify the pre-factors.

Future membrane designs could further enhance the coupling strength by maximizing g_0. The optimal approach might be a low-mass design, where the tether width remains sizable to ensure high heat transfer, a concept established in Chapter 3. Another option is to reduce the optical cavity length L, since $g_0 \propto 1/L$. However, this would consequently expand the beam waist and result in additional clipping losses discussed in 5.5. At present, we do have some tolerance there, which largely depends on how the beam waist shifts with respect to the defect's center during cooldown.

In terms of equipment, we plan to utilize the photomultiplier R13456 by Hamamatsu for our lock beam detection in future endeavors. This device features a noise-equivalent-power of 0.7 fW/$\sqrt{Hz}$ and a bandwidth exceeding 10 MHz. This represents lower noise compared to conventional low-noise silicon avalanche photodiodes. With this tool, we could further decrease our lock beam power below 2 nW input power during locking. The lock beam will consequently not introduce substantial additional heating in relation to the science laser.

Moreover, we aim to incorporate Faraday rotators in detection as it has been done in Brubaker *et al.*, 2022. Until now, we have allowed the back-reflected beam to be reflected in a beam splitter for free space detection, as depicted in Fig. 6.4. However, this method results in a loss of -3 dB of back-reflected signal. Faraday rotators utilize the Faraday effect, with a strong permanent magnet rotating the polarization by 45 degrees upon back-reflection. This will enable us to substitute the beam splitters with polarizing beam-splitters and detect nearly the full signal. We have already acquired FOR-5/57-AR835 5mm aperture TGG Faraday optical rotators from Leysop that operate within our laser wavelength range and are ready for implementation.

Additionally, in case we discover later that our measurement is not quantum noise limited, we could consider operating the lock beam and science beam at two distinct free-spectral ranges. The free-spectral range of the cavity lies in a microwave frequency range, at $2\pi \times 6.3$ GHz. Hence, we could use an IQ mixer and a filter cavity instead of the two acousto-optic modulators (AOMs) currently in use, to generate the science and lock beam. Fig. 8.2 describes the mechanism whereby the IQ mixer creates the lock beam and its sidebands at another FSR.

Lastly, improvements can also be made to the electromechanical system. The gap detuning, as demonstrated in Chapter 4, appears very promising. We need to investigate whether we can validate this increase in g_0 in an electromechanics experiment inside the dilution refrigerator. If successful and the initial measuremnts of Fig. 4.12 were true, this would ideally enable us to reach electromechanical coupling rates of $\Gamma_{\mathrm{e}}/2\pi = 4$ kHz, for the same amount of phase noise as the $\Gamma_{\mathrm{e}}/2\pi = 80$ Hz measurement in Seis *et al.*, 2022.

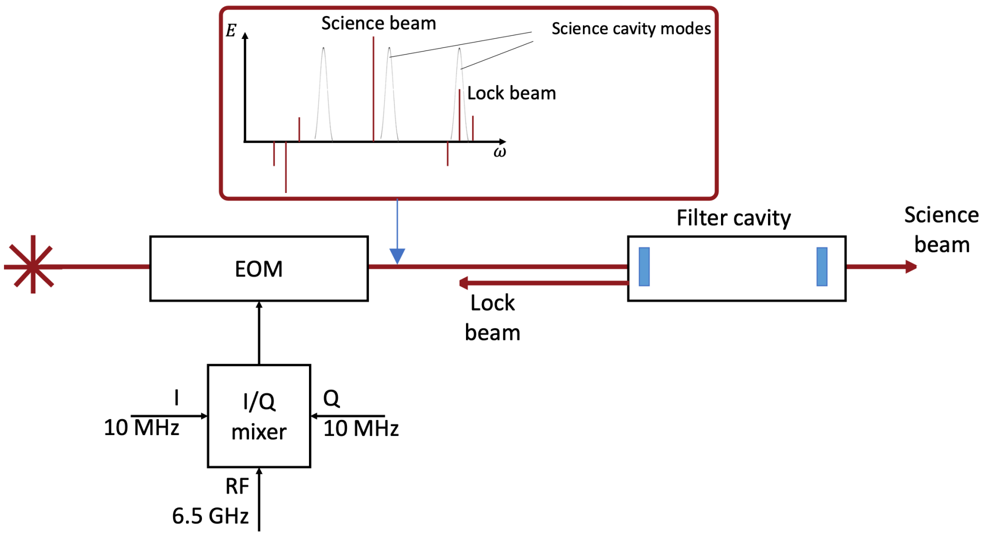

Figure 8.2: Diagram illustrating the process of locking the science beam using a lock beam operating at another FSR, 6.3 - 6.5 GHz detuned. The IQ modulator, together with the electro-optic phase modulator (EOM), generates the lock beam and its sidebands several GHz detuned. After the EOM, a filter cavity can spatially separate the lock and science beams.

9 Bibliography

Andrews, R. W., R. W. Peterson, T. P. Purdy, K. Cicak, R. W. Simmonds, C. A. Regal, and K. W. Lehnert (Mar. 2014). „Bidirectional and efficient conversion between microwave and optical light“. In: *Nature Physics* 10.4, pp. 321–326.

Arute, Frank, Kunal Arya, Ryan Babbush, *et al.* (Oct. 2019). „Quantum supremacy using a programmable superconducting processor“. In: *Nature* 574.7779, pp. 505–510.

Aspelmeyer, Markus, Tobias J. Kippenberg, and Florian Marquardt (Dec. 2014). „Cavity optomechanics“. In: *Reviews of Modern Physics* 86.4, pp. 1391–1452.

Barends, R., J. Kelly, A. Megrant, *et al.* (Apr. 2014). „Superconducting quantum circuits at the surface code threshold for fault tolerance“. In: *Nature* 508.7497, pp. 500–503.

Black, Eric D. (Jan. 2001). „An introduction to Pound–Drever–Hall laser frequency stabilization“. In: *American Journal of Physics* 69.1, pp. 79–87.

Blatt, Rainer and David Wineland (June 2008). „Entangled states of trapped atomic ions“. In: *Nature* 453.7198, pp. 1008–1015.

Bohr, N., H. A. Kramers, and J. C. Slater (Dec. 1924). „Ueber die Quantentheorie der Strahlung“. In: *Zeitschrift fuer Physik* 24.1, pp. 69–87.

Braginskii, V. B. and A. B. Manukin (1967). „Ponderomotive Effects of Electromagnetic Radiation“. In: *Soviet Physics JETP* 25.4, pp. 653–655.

Brubaker, B. M., J. M. Kindem, M. D. Urmey, S. Mittal, R. D. Delaney, P. S. Burns, M. R. Vissers, K. W. Lehnert, and C. A. Regal (June 2022). „Optomechanical Ground-State Cooling in a Continuous and Efficient Electro-Optic Transducer“. In: *Physical Review X* 12.2, p. 021062.

Catalini, Letizia, Massimiliano Rossi, Eric C. Langman, and Albert Schliesser (Apr. 2021). „Modeling and Observation of Nonlinear Damping in Dissipation-Diluted Nanomechanical Resonators“. In: *Physical Review Letters* 126.17, p. 174101.

Catalini, Letizia, Yeghishe Tsaturyan, and Albert Schliesser (July 2020). „Soft-Clamped Phononic Dimers for Mechanical Sensing and Transduction“. In: *Physical Review Applied* 14.1, p. 014041.

Clarke, John and Frank K. Wilhelm (June 2008). „Superconducting quantum bits“. In: *Nature* 453.7198, pp. 1031–1042.

Corruccini, Robert J. and John J. Gniewek (1961). *Thermal Expansion of Technical Solids at Low Temperatures - A Compilation From the Literature*. Ed. by U.S. Government Printing Office. U.S. Department of Commerce - National Bureau of Standards.

Covey, Jacob P., Harald Weinfurter, and Hannes Bernien (Apr. 2023). „Quantum networks with neutral atom processing nodes“. In: arXiv: `2304.02088 [quant-ph]`.

Delaney, R. D., M. D. Urmey, S. Mittal, B. M. Brubaker, J. M. Kindem, P. S. Burns, C. A. Regal, and K. W. Lehnert (June 2022). „Superconducting-qubit readout via low-backaction electro-optic transduction“. In: *Nature* 606.7914, pp. 489–493.

Devoret, Michel H. and John M. Martinis (Oct. 2004). „Implementing Qubits with Superconducting Integrated Circuits“. In: *Quantum Information Processing* 3.1-5, pp. 163–203.

DiVincenzo, David P. and IBM (Feb. 2000). „The Physical Implementation of Quantum Computation“. In: arXiv: `quant-ph/0002077 [quant-ph]`.

Doeleman, H. M., T. Schatteburg, R. Benevides, S. Vollenweider, D. Macri, and Y. Chu (Mar. 2023). „Brillouin optomechanics in the quantum ground state“. In: arXiv: `2303.04677 [quant-ph]`.

Dumont, Vincent, Simon Bernard, Christoph Reinhardt, Alex Kato, Maximilian Ruf, and Jack C. Sankey (Aug. 2019). „Flexure-tuned membrane-at-the-edge optomechanical system“. In: *Optics Express* 27.18, p. 25731.

Fan, Linran, Chang-Ling Zou, Risheng Cheng, Xiang Guo, Xu Han, Zheng Gong, Sihao Wang, and Hong X. Tang (Aug. 2018). „Superconducting cavity electro-optics: A platform for coherent photon conversion between superconducting and photonic circuits“. In: *Science Advances* 4.8.

Fedoseev, Vitaly, Matteo Fisicaro, Harmen van der Meer, Wolfgang Löffler, and Dirk Bouwmeester (Jan. 2022). „Realignment-free cryogenic macroscopic optical cavity coupled to an optical fiber“. In: *Review of Scientific Instruments* 93.1, p. 013103.

Gisler, Thomas, Mohamed Helal, Deividas Sabonis, Urs Grob, Martin Héritier, Christian L. Degen, Amir H. Ghadimi, and Alexander Eichler (Aug. 2022). „Soft-Clamped Silicon Nitride String Resonators at Millikelvin Temperatures“. In: *Physical Review Letters* 129.10, p. 104301.

Gorodetsky, M. L., A. Schliesser, G. Anetsberger, S. Deleglise, and T. J. Kippenberg (Oct. 2010). „Determination of the vacuum optomechanical coupling rate using frequency noise calibration“. In: *Optics Express* 18.22, p. 23236.

Harty, T. P., D. T. C. Allcock, C. J. Ballance, L. Guidoni, H. A. Janacek, N. M. Linke, D. N. Stacey, and D. M. Lucas (Nov. 2014). „High-Fidelity Preparation, Gates, Memory, and Readout of a Trapped-Ion Quantum Bit“. In: *Physical Review Letters* 113.22, p. 220501.

Hisatomi, R., A. Osada, Y. Tabuchi, T. Ishikawa, A. Noguchi, R. Yamazaki, K. Usami, and Y. Nakamura (May 2016). „Bidirectional conversion between microwave and light via ferromagnetic magnons“. In: *Physical Review B* 93.17, p. 174427.

Jiang, Wentao, Felix M. Mayor, Sultan Malik, Raphaël Van Laer, Timothy P. McKenna, Rishi N. Patel, Jeremy D. Witmer, and Amir H. Safavi-Naeini (Oct. 2022). „Optically heralded microwave photons“. In: arXiv: `2210.10739 [quant-ph]`.

Josephson, B.D. (July 1962). „Possible new effects in superconductive tunnelling“. In: *Physics Letters* 1.7, pp. 251–253.

Kim, Youngseok, Andrew Eddins, Sajant Anand, *et al.* (June 2023). „Evidence for the utility of quantum computing before fault tolerance“. In: *Nature* 618.7965, pp. 500–505.

Kjaergaard, Morten, Mollie E. Schwartz, Jochen Braumüller, Philip Krantz, Joel I.-J. Wang, Simon Gustavsson, and William D. Oliver (Mar. 2020). „Superconducting Qubits: Current State of Play“. In: *Annual Review of Condensed Matter Physics* 11.1, pp. 369–395.

Kómár, P., E. M. Kessler, M. Bishof, L. Jiang, A. S. Sørensen, J. Ye, and M. D. Lukin (June 2014). „A quantum network of clocks“. In: *Nature Physics* 10.8, pp. 582–587.

Lauk, Nikolai, Neil Sinclair, Shabir Barzanjeh, Jacob P Covey, Mark Saffman, Maria Spiropulu, and Christoph Simon (Mar. 2020). „Perspectives on quantum transduction“. In: *Quantum Science and Technology* 5.2, p. 020501.

Leivo, M. M. and J. P. Pekola (Mar. 1998). „Thermal characteristics of silicon nitride membranes at sub-Kelvin temperatures“. In: *Applied Physics Letters* 72.11, pp. 1305–1307.

Lvovsky, Alexander I., Barry C. Sanders, and Wolfgang Tittel (Dec. 2009). „Optical quantum memory“. In: *Nature Photonics* 3.12, pp. 706–714.

Magnard, P., S. Storz, P. Kurpiers, *et al.* (Dec. 2020). „Microwave Quantum Link between Superconducting Circuits Housed in Spatially Separated Cryogenic Systems“. In: *Physical Review Letters* 125.26, p. 260502.

Mainman, T. H. (Aug. 1960). „Stimulated Optical Radiation in Ruby“. In: *Nature* 187.4736, pp. 493–494.

Maldovan, Martin (Nov. 2013). „Sound and heat revolutions in phononics“. In: *Nature* 503.7475, pp. 209–217.

Marinković, Igor, Maxwell Drimmer, Bas Hensen, and Simon Gröblacher (Jan. 2021). „Hybrid Integration of Silicon Photonic Devices on Lithium Niobate for Optomechanical Wavelength Conversion“. In: *Nano Letters* 21.1, pp. 529–535.

Meesala, Srujan, Steven Wood, David Lake, Piero Chiappina, Changchun Zhong, Andrew D. Beyer, Matthew D. Shaw, Liang Jiang, and Oskar Painter (Mar. 2023). „Non-classical microwave-optical photon pair generation with a chip-scale transducer“. In: arXiv: `2303.17684 [quant-ph]`.

Metzger, Constanze, Max Ludwig, Clemens Neuenhahn, Alexander Ortlieb, Ivan Favero, Khaled Karrai, and Florian Marquardt (Sept. 2008). „Self-Induced Oscillations in an Optomechanical System Driven by Bolometric Backaction“. In: *Physical Review Letters* 101.13, p. 133903.

Midolo, Leonardo, Albert Schliesser, and Andrea Fiore (Jan. 2018). „Nano-opto-electro-mechanical systems“. In: *Nature Nanotechnology* 13.1, pp. 11–18.

Mirhosseini, Mohammad, Alp Sipahigil, Mahmoud Kalaee, and Oskar Painter (Dec. 2020). „Superconducting qubit to optical photon transduction“. In: *Nature* 588.7839, pp. 599–603.

Nakamura, Y., Yu. A. Pashkin, and J. S. Tsai (Apr. 1999). „Coherent control of macroscopic quantum states in a single-Cooper-pair box“. In: *Nature* 398.6730, pp. 786–788.

Nielsen, William Hvidtfelt Padkær, Yeghishe Tsaturyan, Christoffer Bo Møller, Eugene S. Polzik, and Albert Schliesser (Dec. 2016). „Multimode optomechanical system in the quantum regime“. In: *Proceedings of the National Academy of Sciences* 114.1, pp. 62–66.

Olivieri, E., J. Billard, M. De Jesus, A. Juillard, and A. Leder (June 2017). „Vibrations on pulse tube based Dry Dilution Refrigerators for low noise measurements“. In: *Nuclear Instruments and Methods in Physics Research Section A: Accelerators, Spectrometers, Detectors and Associated Equipment* 858, pp. 73–79.

Onnes, H.K. (1911). „Further experiments with liquid helium“. In: *Koninklijke Akademie van Wetenschappen te Amsterdam* 120b.15, p. 269.

Østfeldt, Christoffer (2022). „Quantum Optomechanics for Hybrid Spin–Membrane Entanglement“. PhD thesis. University of Copenhagen.

Page, Michael A., Maxim Goryachev, Haixing Miao, *et al.* (Feb. 2021). „Gravitational wave detectors with broadband high frequency sensitivity". In: *Communications Physics* 4.1.

Pampaloni, Francesco and Joerg Enderlein (2004). *Gaussian, Hermite-Gaussian, and Laguerre-Gaussian beams: A primer*.

Planck, Max (1901). „Ueber das Gesetz der Energieverteilung im Normalspectrum". In: *Annalen der Physik* 309.3, pp. 553–563.

Rabl, P., C. Genes, K. Hammerer, and M. Aspelmeyer (Dec. 2009). „Phase-noise induced limitations on cooling and coherent evolution in optomechanical systems". In: *Physical Review A* 80.6, p. 063819.

Rossi, Massimiliano (2020). „Quantum Measurement and Control of a Mechanical Resonator". PhD thesis. University of Copenhagen.

Rossi, Massimiliano, David Mason, Junxin Chen, Yeghishe Tsaturyan, and Albert Schliesser (Oct. 2018). „Measurement-based quantum control of mechanical motion". In: *Nature* 563.7729, pp. 53–58.

Saarinen, Sampo A., Nenad Kralj, Eric C. Langman, Yeghishe Tsaturyan, and Albert Schliesser (Mar. 2023). „Laser cooling a membrane-in-the-middle system close to the quantum ground state from room temperature". In: *Optica* 10.3, p. 364.

Sahu, R., L. Qiu, W. Hease, G. Arnold, Y. Minoguchi, P. Rabl, and J. M. Fink (May 2023). „Entangling microwaves with light". In: *Science* 380.6646, pp. 718–721.

Sahu, Rishabh, William Hease, Alfredo Rueda, Georg Arnold, Liu Qiu, and Johannes M. Fink (Mar. 2022). „Quantum-enabled operation of a microwave-optical interface". In: *Nature Communications* 13.1.

Seis, Yannick (2021). „Ultra-Coherent Electro-Mechanics in the Quantum Regime". PhD thesis. University of Copenhagen.

Seis, Yannick, Thibault Capelle, Eric Langman, Sampo Saarinen, Eric Planz, and Albert Schliesser (Mar. 2022). „Ground state cooling of an ultracoherent electromechanical system". In: *Nature Communications* 13.1.

Shor, Peter W. (Oct. 1997). „Polynomial-Time Algorithms for Prime Factorization and Discrete Logarithms on a Quantum Computer". In: *SIAM Journal on Computing* 26.5, pp. 1484–1509.

Tsaturyan, Y., A. Barg, E. S. Polzik, and A. Schliesser (June 2017). „Ultracoherent nanomechanical resonators via soft clamping and dissipation dilution". In: *Nature Nanotechnology* 12.8, pp. 776–783.

Tsaturyan, Yeghishe (2019). „Ultracoherent soft-clamped mechanical resonators for quantum cavity optomechanics“. PhD thesis. University of Copenhagen.

Uhlig, Kurt (Mar. 2023). „Dry dilution refrigerator with pulse tube shutoff option“. In: *Cryogenics* 130, p. 103649.

Vogt, Thibault, Christian Gross, Jingshan Han, Sambit B. Pal, Mark Lam, Martin Kiffner, and Wenhui Li (Feb. 2019). „Efficient microwave-to-optical conversion using Rydberg atoms“. In: *Physical Review A* 99.2, p. 023832.

Wang, Changqing, Ivan Gonin, Anna Grassellino, Sergey Kazakov, Alexander Romanenko, Vyacheslav P. Yakovlev, and Silvia Zorzetti (Dec. 2022). „High-efficiency microwave-optical quantum transduction based on a cavity electro-optic superconducting system with long coherence time“. In: *npj Quantum Information* 8.1.

Yuan, Mingyun, Martijn A. Cohen, and Gary A. Steele (Dec. 2015). „Silicon nitride membrane resonators at millikelvin temperatures with quality factors exceeding 108“. In: *Applied Physics Letters* 107.26.

Zeuthen, Emil, Albert Schliesser, Anders S Sørensen, and Jacob M Taylor (May 2020). „Figures of merit for quantum transducers“. In: *Quantum Science and Technology* 5.3, p. 034009.

Zhou, X., D. Cattiaux, R. R. Gazizulin, A. Luck, O. Maillet, T. Crozes, J.-F. Motte, O. Bourgeois, A. Fefferman, and E. Collin (Oct. 2019). „On-chip Thermometry for Microwave Optomechanics Implemented in a Nuclear Demagnetization Cryostat“. In: *Physical Review Applied* 12.4, p. 044066.

Zwickl, B. M., W. E. Shanks, A. M. Jayich, C. Yang, A. C. Bleszynski Jayich, J. D. Thompson, and J. G. E. Harris (Mar. 2008). „High quality mechanical and optical properties of commercial silicon nitride membranes“. In: *Applied Physics Letters* 92.10.